Development of a cryogenic silicon detector system and study of strange particle production in deep inelastic scattering

Dissertation

by

Rita De Masi

Physik-Department E18

Technische Universität München

July 2004

Fakultät für Physik der Technischen Universität
München
Physik Department E18

Development of a cryogenic silicon detector system
and
study of strange particle production
in deep inelastic scattering

Rita De Masi

Vollständiger Abdruck der von der Fakultät für Physik der Technischen Universität München zur Erlangung des akademischen Grades eines

Doktors der Naturwissenschaften (Dr. rer. nat.)

genehmigten Dissertation.

Vorsitzender: Univ.-Prof. Dr. A. J. Buras

Prüfer der Dissertation:

1. Univ.-Prof. Dr. St. Paul
2. Univ.-Prof. Dr. F. von Feilitzsch

Die Dissertation wurde am 25/10/04 bei der Technischen Universität München eingreicht und durch die Fakultät für Physik am 9/11/04 angenommen.

Contents

List of Figures

Introduction

The main goal of high energy physics is to find the ultimate components of matter and understand how they combine in order to form matter in the universe as seen today. Already the Greek philosopher Democritos (about 400 a.C.) hypothesised that matter is discontinuous and named its constituents *atoms*. From the end of the 19th century several experimental observations have confirmed the discontinuous structure of the matter. Since then many scientific theories and experimental models have been developed: now we know that atoms are composed of electrons, protons and neutrons. Protons and neutrons (collectively called *nucleons*) are not point-like, but they are in turn composed of pointlike fermions, with fractional electric charge, called *quarks*. Physicists discovered the existence of six type of quarks, called flavours, u, d, s, c, b and t. Nucleons are in first approximation composed of u and d quarks, but quarks combine to form also several other particles with short lifetime called *hadrons*.

Quarks are suject to electromagnetic, weak and strong forces. The *Quantum Electrodynamics* (QED) describes succesfully the interaction between electrically charged particles. The strong force is responsible for the formation of proton and neutrons and its residual effects account for the binding of nucleons in the atomic nucleus. In analogy with QED, the *Quantum Chromodynamics* (QCD) describes the strong interactions between quarks. The basic idea of QCD is that quarks carry a strong "colour" charge, analogue to the electric charge, which can take on three different values, labelled *red*, *blue* and *green*. Quarks are subject to the *colour force field* and they interact via the exchange of *field quanta* called *gluons*, which carry also colour. The gluons in QCD play an analogous role as the photons in QED. Presently no free quarks have been observed: this peculiarity is explained assuming the strong force to be significant at large distances and negligible at short distances. This behaviour is a result of the self-coupling of gluons, a key ingredient of QCD. This means that if quarks are close to each other ($\ll$1 fm) they behave like free particles but, as soon as their relative distance increases, the mutual attraction becomes stronger. The effect of this is that quarks remain confined in the hadron volume, which is colourless, and only this can be observed as free particle [Per82], [CM84].

All the hadrons which are observed until now are either formed of three quarks (baryons) or a quark−antiquark pair (mesons). However QCD does not exclude the existence of states with different quark content, provided that they are colourless, i.e. multiple of three colours or colour anti-colour pairs. Thus, in principle hybrid states which have explicitly excited gluonic components are possible, as well as states composed of two quark-antiquark pairs (*tetraquark*, $qq\overline{q}\overline{q}$), of three quarks and a quark-antiquark pair (*pentaquark*, $qqqq\overline{q}$) and so on. They are collectively called *exotics* [jaf04].

The actual theoretical understanding of exotic states in general and of pentaquarks in particular is nonetheless quite poor. Several models have been developed, in the framework of QCD, which predict the existence of pentaquarks and their characteristics (spin, parity, life time, etc.). At this point experimental results are needed to confirm the validity of the predictions. From the experimental side, evidence for two possible pentaquark states, Θ^+ and Ξ^{--}, have been given in the last year. These states are supposed to have minimum quark content $uudd\bar{s}$ and $ddss\bar{u}$ for Θ^+ and Ξ^{--}, respectively. The studies of Θ^+ pentaquark candidates were performed in photo- and hadro-production, while the Ξ^{--} was studied only in hadro-production. However the claimed pentaquark signals have a rather moderate significance [LEP03], [na403] and, moreover, several experiments gave contradicting results. This clearly asks for more experiments with higher statistics to clarify the matter. The study of the Ξ^{--} pentaquark candidate within the COMPASS experiment is the analysis part of this work.

COMPASS [COM96] is a fixed target experiment presently running at CERN-SuperProtoSyncrotron (SPS) using a 160 GeV muon beam. Its principal characteristics are high count rate and high precision. Both of these features are needed in order to study exotic states. One of the proposed goal of COMPASS is the study of exotics using a hadron beam; this task will be performed in the next years. However, the data acquired with muon beam offer the possibility of performing systematic studies of pentaquarks in photo-production.

The high precision of the COMPASS spectrometer is achieved with an accurate tracking of incoming and outcoming particles with respect to the target. A precise reconstruction of the beam particles before they interact in the target is obtained by using silicon microstrip detectors. Since COMPASS uses high intensity beams ($\sim 10^8$ particle/s) the silicon detectors absorbe high dose and, hence, suffer radiation damage. To maintain an optimal detection efficiency for long periods of data taking, detectors must be operated at cryogenic temperatures, exploiting the so-called *Lazarus effect* [RD39].

The work reported in this thesis can be divided in two parts. In the first part the design, installation and operation of a silicon detector system operated at cryo-

genic temperatures is presented. In the second part the data analysis is described with emphasis on the search for Ξ^{--} pentaquark candidate. The first chapter of this thesis describes the physics goals and the experimental setup of COMPASS. An introduction to the physics of silicon detectors is given in the second chapter, where the effect of radiation damage and the Lazarus effect are outlined. The third chapter is dedicated to the specific accomplishment of a silicon microstrip detector in COMPASS, with a special emphasis on the readout electronics. The realisation of a silicon detector system operating at cryogenic temperatures is reported in the fourth chapter; the work also included the design, development and testing of the cryogenic infrastructures. The fifth chapter, after an overview of the present status, both from a theoretical and experimental points of view, describes the analysis performed with the COMPASS data to search for the exotic pentaquark candidate Ξ^{--}. The results are discussed with respect to the general experimental scenario and finally conclusions are given.

Chapter 1

The COMPASS experiment

The **CO**mmon **M**uon and **P**roton **A**pparatus for **S**tructure and **S**pectroscopy (*COMPASS* (*NA58*)) is a fixed target experiment at the CERN[1] **S**uper-**P**roton-**S**yncrotron (*SPS*). The COMPASS experiment is the result of the merging of two different experiments, namely *HMC* and *CHEOPS* which had similar experimental needs, but had different physics objectives. HMC was designed to investigate the nucleon structure using a muon beam; CHEOPS had its main focus on hadron spectroscopy using hadron beam. COMPASS is thus able to address a wide range of physics goals achievable with both muon and hadron probes. The experimental apparatus was designed to be suitable for both configurations.

COMPASS began to take data in 2001 and, since then, it has been running with the muon beam. The first run with hadron beams will take place in September 2004 and will continue in 2006, after the SPS break planned for 2005.

The first part of this chapter focuses on the physics goals of the experiment: Sec. 1.1.1 describes the goals of the muon beam program; Sec. 1.1.2 describes the topics to be investigated with hadron beams. The second part illustrates and explains the COMPASS detector, including a description of the component which have to be modified in order to change from one configuration to the other.

1.1 The physics aims

1.1.1 Physics with the muon beam

The main goal of the COMPASS muon program is to understand the spin composition of the nucleon [COM96]. The spin of the nucleon is the total spin and

[1] European Centre for Nuclear Research

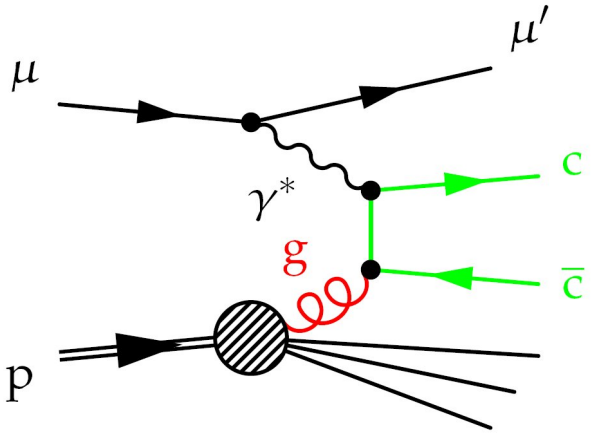

Figure 1.1: The Photon-Gluon Fusion process: the virtual photon in muon scattering interacts with the gluon via an intermediate quark. The intermediate quark provides the colour and electric charge conservation.

angular momentum of its constituents, that is:

$$\frac{1}{2} = \frac{1}{2}\Delta\Sigma + \Delta G + L_z^q + L_z^g \tag{1.1}$$

where the left-hand side of the equation is the spin $\frac{1}{2}$ of the nucleon, $\frac{1}{2}\Delta\Sigma$ is the quark spin contribution, ΔG is the gluon spin contribution, L_z^q and L_z^g are the orbital angular momentum of quarks and gluons, respectively. Various experiments ([EMC88], [SMC99], [HER98]) have measured $\Delta\Sigma = 0.27 \pm 0.13$. The other terms are presently still unknown.

With **S**emi **I**nclusive **D**eep **I**nelastic **S**cattering (*SIDIS*) measurements, COMPASS can provide information on the spin contributions of individual quark flavours (Δq) and on the gluon polarisation (ΔG), as well as on the total orbital angular momentum. Additional topic of interest is the measurement of the transverse spin contribution which is accessible with a transversely polarised target. All these measurements are discussed in the following.

ΔG/G

The measurement of the gluon polarisation ΔG is crucial to understand the puzzle of the nucleon spin. In COMPASS, ΔG can be accessed via **P**hoton-**G**luon **F**usion (*PGF*) process, which is shown in Fig. 1.1.

Three different channels can be studied, namely the *open charm* channel, the *high p_T pair* channel and the *high p_T single* channel.

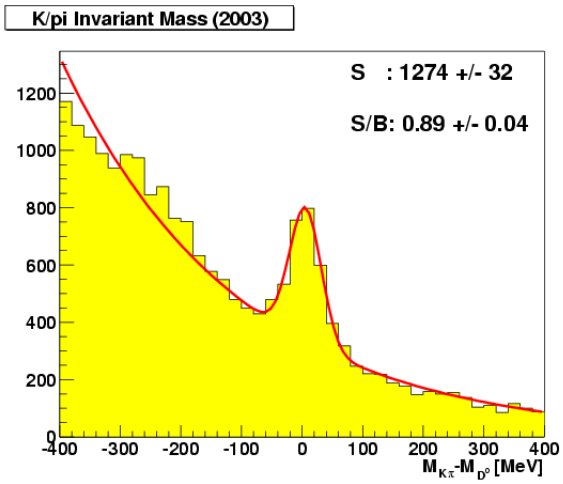

Figure 1.2: The $K^-\pi^+$ invariant mass spectrum where a clear peak for D^0 is visible.

- **Open charm** Due to its large mass, the presence of the c quark in the quark sea of a nucleon is of low probability. Moreover, the production of heavy quarks in leading order at COMPASS energies goes predominantly via PGF, leading to two charm tracks (c.f. Fig. 1.1). Therefore, the observation of charmed particles is a flag for the PGF process. The lightest charmed particles are D^0 mesons, which are cleanly identified in COMPASS in the decay chain $D^0 \rightarrow K^-\pi^+$. Fig. 1.2 shows the $K^-\pi^+$ invariant mass spectrum where a clear peak for D^0 is visible. A substantial reduction of the background is achieved by requiring that the D^0 come from D^{*+} decay, that is:

$$D^{*+} \rightarrow D^0\pi^+ \rightarrow K^-\pi^+\pi^+ \tag{1.2}$$

It is possible to correlate the number of charm events to the gluon polarisation (see [Mal96]) as:

$$A^{\text{exp}} = \frac{N_{c\bar{c}}^{\uparrow\downarrow} - N_{c\bar{c}}^{\uparrow\uparrow}}{N_{c\bar{c}}^{\uparrow\downarrow} + N_{c\bar{c}}^{\uparrow\uparrow}} \propto \frac{\Delta\sigma^{\gamma N\rightarrow c\bar{c}X}}{\sigma^{\gamma N\rightarrow c\bar{c}X}} = \frac{\Delta\sigma(\hat{s}) \otimes \Delta G(\eta,\hat{s})}{\sigma(\hat{s}) \otimes G(\eta,\hat{s})} \tag{1.3}$$

where A^{exp} is the spin-dependent asymmetry, $N_{c\bar{c}}$ is the number of charm events for target spin parallel or antiparallel to the spin of the beam muon, $\Delta\sigma^{\gamma N\rightarrow c\bar{c}X}$ and $\sigma^{\gamma N\rightarrow c\bar{c}X}$ are the helicity-dependent and helicity-averaged cross sections, respectively; these last two terms can be expressed as a convolution of the photon-gluon cross section $\Delta\sigma(\hat{s})$ and $\sigma(\hat{s})$ with the gluon distribution $\Delta G(\eta,\hat{s})$ and $G(\eta,\hat{s})$. $\hat{s}$ is the invariant mass squared of the photon-gluon system and η is the gluon momentum fraction.

- **High p_T pair** In principle the asymmetry A^{exp} can be measured for quarks of any flavour. A signature of PGF is the production of two jets emitted in opposite direction (in the centre of mass system) . This channel has higher statistics compared to the charm case, but also a higher background. By selecting only the hadrons with high transverse momentum ($p_T > 1$ GeV/c), a sensible reduction of the background is achieved. However the Compton scattering off a quark ($\gamma q \rightarrow gq$) has the same order in α_s like the PGF: the two processes cannot be distinguished experimentally, and Monte Carlo simulations are needed to estimate the contribution of the Compton scattering to the asymmetry. For the asymmetry:

  $$A_{LL}^{\gamma^* d \rightarrow hhX} = -0.065 \pm 0.036(stat) \pm 0.005(syst) \tag{1.4}$$

  was measured [OC04]. The Monte Carlo simulation to extract $\Delta G/G$ is still under development.

  The present status of the $\Delta G/G$ measurement in both the open charm and high p_T channels can be found in [OC04].

- **High p_T single particle** Recently the possibility of measuring ΔG via single particles created with high momentum was raised. This measurement is interesting, due to its low theoretical background and to the high statistics. On the contrary, the experimental background is difficult to estimate. More theoretical studied are needed to extract ΔG from the measured asymmetry. The feasibility of the measurement is at present under investigation [SHP].

Spin distribution functions

SIDIS measurements can access the spin distribution functions (Δq) of different flavours. Asymmetries with various leading hadrons in the final state are the means to measure the fractional contribution of the different quark flavours to the nucleon spin. The results of the measurement of the Λ^0 polarisation, which allow the extraction of the Δs spin distribution, can be found in [Lam04].

Transversity

A complete description of the nucleon structure at leading order is given by the three independent **P**arton **D**istribution **F**unctions (*PDF*) $q(x), \Delta q(x)$ and $\Delta_T q(x)$. The latter, called the *transverse spin distribution*, describes the quark distribution in a transversely polarised nucleon as probed by a longitudinally polarised beam and it is $\Delta_T q = q_{\uparrow}^{\rightarrow} - q_{\downarrow}^{\rightarrow}$.

In analogy with $g_1(x)$ one can define the structure function $h_1(x)$ as:

$$h_1(x) = \frac{1}{2}\sum_q e_q^2[\Delta_T q(x) + \Delta_T \bar{q}(x)]. \tag{1.5}$$

$h_1(x)$ cannot be measured in DIS processes due to its odd chirality nature, but it can be accessed by those process which show two helicity flips. One of those process is the polarised **S**emi-**I**nclusive **D**eep **I**nelastic **S**cattering (*p-SIDIS*) on a transversally polarised target, where $h_1(x)$ can be extracted by the azimuthal dependence of the leading hadron (*Collins angle*). The struck quark flavour can be identified by measuring the involved hadron.

The present status of the COMPASS transversity analysis can be found in [h1].

Generalised Parton Distributions (*GPD*)

In recent times the GPD [GPD02] are a promising tool for the understanding of nucleon structure as they provide a complete description of the nucleon by unifying the concepts of parton distributions and hadronic form factors. Exclusive measurements such as **H**ard **E**xclusive **M**eson **P**roduction (*HEMP*) and **D**eeply **V**irtual **C**ompton **S**cattering (*DVCS*) can experimentally access the GPDs.

An important remark about DVCS measurements is that they can access the orbital momenta, giving, as previously described, a crucial contribution in the understanding of the nucleon spin.

The HEMP and DVCS measurements are not present in the original COMPASS proposal of 1996. Nonetheless, feasibility studies [DVC] have shown that the COMPASS apparatus is highly suited to perform them, with additionally a large domain in (x_{Bj}, Q^2). Preliminary measurements have been already carried out, and a complete program will take place during the second phase of COMPASS after 2005.

Transverse Λ^0 polarisation

Another topic which was not included in the COMPASS proposal is the transverse Λ^0 polarisation. It was observed [Les75] that Λ^0s produced in non polarised processes have a preferred spin orientation, i.e. a polarisation. The preferred axis is normal to the production plane of the Λ^0. This phenomenon indicates the role of particle spin in the production mechanism. COMPASS has measured the transverse Λ^0 polarisation in photo-production; the results of this measurement can be found in [Wie03].

1.1.2 Physics with the hadron beam

The physics program to be covered by using hadron beams comprises three main aims: the study of doubly charmed baryons; the spectroscopy of exotic states and glueballs; the measurement of meson polarisabilities via Primakoff scattering. A complete description of the hadron physics program can be found in the proposal of the COMPASS experiment [COM96].

Doubly charmed baryons

Presently, little is know about doubly charmed baryons. They are most likely composed of a heavy cc-diquark surrounded by a light quark with masses in the region 3.6-3.8 GeV as first observed by the SELEX experiment [Moi02]. Doubly charmed baryons are expected to have a very low cross section. COMPASS uses high intensity beams in order to achieve high statistics;for this reason it is expected to give a significant contribution to the spectroscopy of doubly charmed baryons, as well as to the characterisation of their decay mechanism.

Exotic states and glueballs

An important property of the **Q**uantum **C**hromo**D**ynamic (*QCD*) theory is that the exchange bosons of the colour force, the gluons, have themselves a colour charge. As a consequence, the gluons can interact between each other and there is no theoretical impediment for them to form bound states. One expects to find then *glueballs*, pure gluonic states, and *hybrids*, states with both quark and valence gluons. These states are expected to have a short lifetime. The characteristics that distinguish them from other hadronic resonances is that they can have quantum numbers which are forbidden to any $q\bar{q}$ or qqq state. For this reason they are called *exotics*.

Also, another set of hadronic states can have exotic numbers, namely the so called *Tetraquarks* and *Pentaquarks*. These states are composed of more than three valence quarks or antiquarks, however have baryonic number B=0 or 1, like the usual hadronic states. Since the study of pentaquarks is one of the topic of this thesis, a more detailed description of the theoretical background will be given in the subsequents chapters.

Primakoff scattering

The pion polarisabilities are important observables for the understanding of hadron structure in the low energy range of QCD. The best way to access them is via $\gamma\pi$ Compton scattering. The difficulty of having a pion target can be overcome with Primakoff scattering. Instead of a photon beam on a pion target, the following interaction is used:

$$\pi + Z \rightarrow \pi\prime + \gamma + Z\prime \tag{1.6}$$

The incident pion scatters on a virtual photon of the Coulomb field of a nucleus with atomic number Z. A real photon is produced and can be detected, together with the scattered pion, in the final state. The Primakoff scattering can be seen as a Compton scattering in inverse kinematics.

These measurements can access the electric and magnetic polarisabilities of the pion and, for the first time, of the kaon. A complete review on the Primakoff measurements in COMPASS can be found in [pol02] and [Kuh01].

1.2 The COMPASS detector

In order to pursue its various physics goals, the COMPASS experiment has to achieve high statistics with high precision. The realisation of these two requirements is challenging for the detectors and the **D**ata **Ac**Q**u**isition system (*DAQ*). As an example, because of the high intensity beam ($\sim 10^8$ particles/s) both a fast readout electronics and radiation hard detectors are required.

Fig. 1.3 shows the setup for the muon run as in the proposal.

The beam hits a solid state target. The spectrometer is composed of different detectors placed along the beam, which enables the reconstruction of the tracks and the momenta of the interaction products and particle identification.

The spectrometer is $\approx$ 60 m long and divided into two stages positioned behind each other. The first stage is designed to detect particles emitted at low momenta (5-50 GeV) and at large angles and it is therefore called *Large Angle Spectrometer*. Detectors with high interaction length (calorimeters and muon wall) have a hole in the middle to allow the high momentum particles to pass undisturbed. These particles are detected in the *Small Angle Spectrometer* that detects particles with momentum from 30 to 100 GeV.

In the subsequent sections the different components comprising the spectrometer are described.

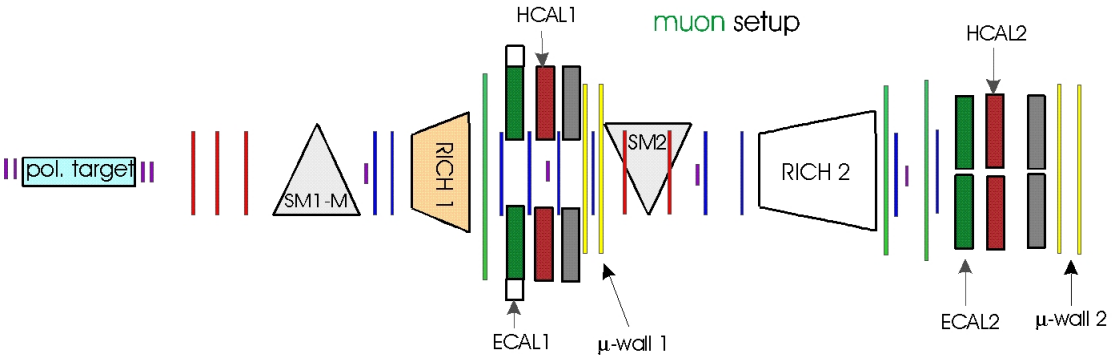

Figure 1.3: The COMPASS setup for the muon run. The beam goes from left to right. The position of the target and of the detectors is shown. The vertical lines represent tracking detectors.

1.2.1 The polarised beams

COMPASS is installed in the experimental hall *EHN2* of the CERN North Area. The experiment is served by the **M2** beam line which can provide both muon and hadron beams. The line can provide also an electron beam which can be used for test purposes.

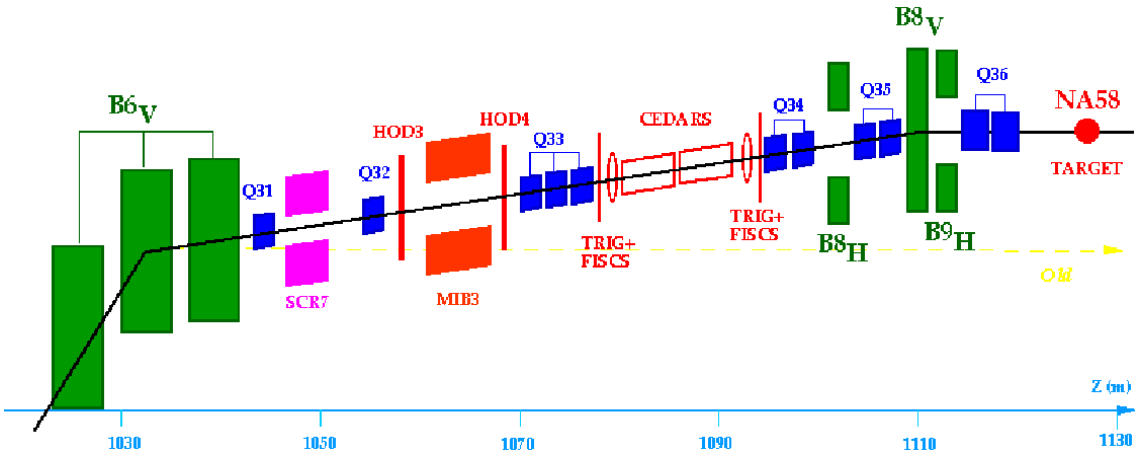

Figure 1.4: The **M2** beam line

The extraction line is shown in Fig. 1.4. A 400 GeV/c primary proton beam is extracted from the SPS and is directed towards the primary target **T6**. The proton intensity on the target varies between 10^{12} and 10^{13} protons per SPS cycle. From the **T6** target a secondary beam is derived. In the case of the muon beam, the

tertiary muons arise from pion and kaon decays. A Beryllium absorber stops the hadrons in the beam. In the case a hadron beam is wished, the absorber are moved and the secondary particles are directly transported to the COMPASS target; in this case Cherenkov detector (CEDAR) are installe in the beam line to perform particle identification. The beam is focused via a set of dipole and quadrupole magnets. The polarisation of the muon is obtained by selecting a certain energy range via the bending magnets. Due to the spill structure of the proton beam to the SPS, the flux of muons is not continuous but concentrated in 4.8 s (extraction at the SPS) followed by 12 ns when no beam is delivered, for a total of 16.8 s cycle. The characteristics of the beam for both muon and hadron programs are shown in Tab. 1.1.

	muon program	hadron program
particles	μ^+	π, k, p
energy (GeV/c)	60-160	100-300
intensity (particles/spill)	$2 \cdot 10^8$	10^8
beam size on the target (RMS in cm)	~ 0.8	$0.3 - 0.5$

Table 1.1: Characteristics of the beam for the muon and the hadron programs.

For a complete description of the M2 beam line and especially the COMPASS dedicated modifications, see [M2].

1.2.2 The spectrometer

Due to time and manpower constraints, for the time being, COMPASS is running with only a partially equipped spectrometer. Fig. 1.5 shows the setup as at 2003. The main difference is the absence of the RICH II (**R**ing **I**maging **CH**erenkov) detector and the electronic calorimeter in the second stage of the spectrometer. In the following the different parts of the COMPASS spectrometer will be discussed. The information concerning the detectors were obtained from [Wie03], [Fau04], [Kuh02], [Leb02], [Ilg03], [Ehl02], [Tak03] and [COM].

The targets

COMPASS uses both muon and hadron beams that can address different physical problems. In order to pass from one program to the other, the spectrometer setup must be slightly modified. The most important difference lies in the target.

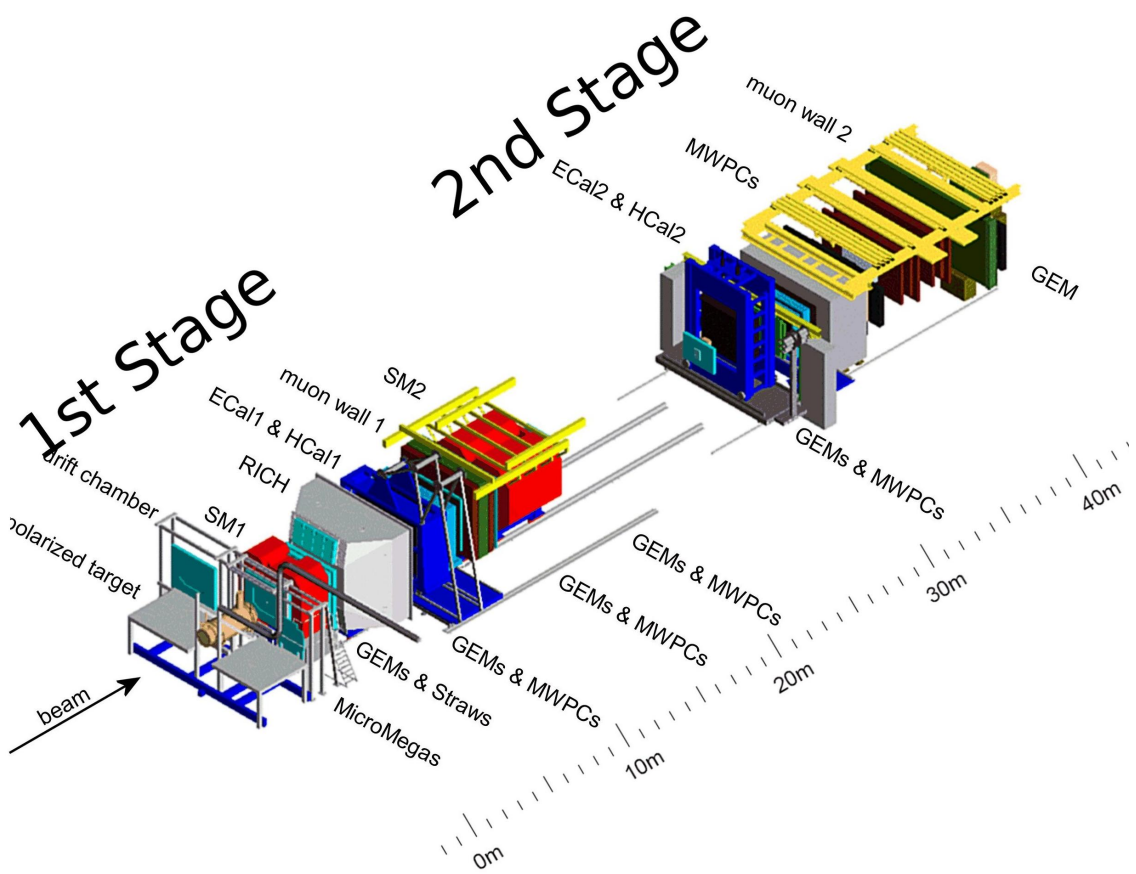

Figure 1.5: The COMPASS spectrometer in 2003: the beam passes from left to right. The two different stages are marked togheter with the position of the detectors.

- The target for the muon program is made of two cylindrical rods of ^6LiD of 1.5 cm radius and 60 cm lenght separated by 10 cm. The two cells are polarised via **D**ynamic **N**uclear **P**olarisation (*DNP*) at a temperature of 0.5 K and in a magnetic field of 2.5 T. According to the physical problem to be investigated, the cells can be longitudinally or transversely polarised with respect to the beam direction. The two cells have opposite directions of polarisation with respect to each other, to avoid systematic errors in the offline reconstruction; for the same reason the polarisation of the cells is inverted every 8 hours. Because of technical problems, the COMPASS solenoid magnet has not been completed in time. This fact forced the SMC target magnet, which has a lower acceptance with respect to the COMPASS magnet ($\pm$70 mrad instead of $\pm$160 mrad), to be reactivated. A polarisation of 55% was achieved in the 2003 data run.

- A different target will be used in the hadron program: the Primakoff and charm programs require a thin (2-3 mm) solid high-Z target. A precision vertex reconstruction is obtained with 3 or more silicon stations installed downstream. For the Primakoff program an additional *veto box* (a barrel of scintillators placed around the target) allows unwanted events, where hadronic fragments are produced, to be vetoed. For the diffractive and central production programs a liquid hydrogen target is used. A recoil detector made of layers of scintillators will be installed around the target. The detector is needed to identify the recoil proton.

The magnets

COMPASS uses conventional dipole magnets to reconstruct the particle momenta. Tracking detectors placed up and downstream of the magnets, permit the reconstruction of the deflected tracks. By knowing the properties of the magnetic field it is possible to extract the momentum of the particles. The first magnet **SM1** has a central gap of $110 \times 153 \times 172$ cm^3; for the hadron program the height of the gap will be reduced from 172 a 82 cm. SM1 has a integrated field on 1 Tm at 2500 A. The second magnet **SM2** has a gap of $400 \times 200 \times 100$ cm^3 and a maximum integrated field of 5.2 Tm. During the 2003 run it was operated at 4.4 Tm at 4000 A.

The tracking

COMPASS uses different tracking detectors along the entire spectrometer. They can be divided into three classes depending on their size: **VSAT** (**V**ery **S**mall

Area **T**racker); **SAT** (**S**mall **A**rea **T**racker) and **LAT** (**L**arge **A**rea **T**racker). A brief review of the trackers is given, while a summary of detectors size and spatial resolution is given in Tab. 1.2.

- **VSAT**: For the region upstream of the target and for the area in proximity of the scattered beam, where the particle density is high, detectors with high spatial resolution and small size are used. There are two different types of *Scintillating Fibres Stations* (**SCIFI-J** and **SCIFI-G**), that additionally have excellent time resolution ($\approx$ 400 ps) and are used to assign the correct time to the event. The *Silicon* detectors (**SI**) are used in the muon setup only upstream of the target for beam reconstruction. Instead, for the hadron setup, more detectors are foreseen downstream of the interaction point to improve the vertex reconstruction. Since the silicon detectors form one of the main topics of this thesis, their characteristics and usage in COMPASS are more extensively discussed in the chapters 2 and 3.

- **SAT**: The **SAT**s have a larger active area than the **VSAT**. The **SAT**s are *Micromegas* (**MM**) [MM] and *GEM* [Sau97] detectors: they are both gaseous detectors with innovative systems for the charge amplification stage (a metallic micromesh and a perforated copper-clad polymer foil, respectively). The central part of the detectors, where the beam passes through, is usually disactivated to avoid discharges in the gas due to the high intensity.

- **LAT**: The most outer area with respect to the beam direction, where the intensity is low and high resolution is not required, is covered by the **LAT**. Conventional *Drift Chambers* (**DC** and **W45**), *Multi Wire Proportional Chambers* (**MWPC**) and *Straw* chambers are used.

Detector	Active area (mm^2)	Spatial resolution (μm)
SCIFI-J	52.25×52.25	120
SCIFI-G	123×123	410
SI	50×70	7
MM	380×380	70
GEM	300×300	46
DC	1400×1250	240
W45	2400×5000	2000
MWPC	1500×1200	500
STRAW	3250×2770	250

Table 1.2: Spatial resolution for the various tracking detectors.

Usually three detectors, one per type, are mounted close to each other, centred along the beam direction. This nested configuration is particularly efficient: a large area is covered to maximise the tracking efficiency; different spatial resolutions in regions with different intensity minimises the occupancy, reducing the data rate for each event.

The particle identification (PID)

In order to distinguish between pions, protons and kaons, COMPASS uses **RICH** detectors. A RICH detector measures the velocity of particles via their Cherenkov emission angle at their passage though the material radiator. For the partial setup, only the RICH-1 detector was installed. Its purpose is to separate π, p and K with momenta up to 60 GeV/c. The photons are detected via MWPCs with CsI photocatodes.

The energies of all particles, except the muons and neutrinos, are measured by the calorimeters, where they are absorbed and deposit all their energy. Due to the high density of the material in the calorimeter, the particle creates a shower that allows to reconstruct the position of the incident particle. Calorimeters are also the only detectors in COMPASS which are sensitive to neutral particles. Each stage is equipped with electronic and hadronic calorimeters, installed downstream of the RICH. The electronic calorimeters ECAL1 and ECAL2 are made out of lead glass blocks from the former experiment GAMS. In 2003 ECAL-2 was installed, and ECAL-1 will be installed later next year. The hadronic calorimeters HCAL1 and HCAL2 have a similar structure, consisting of sandwich of scintillators and iron plates. The information from HCAL1 and HCAL2 are also used in the formation of the trigger.

The high penetration capability of high energy muons is used to identify them in the muon wall detectors **MW1** and **MW2**. A particle is identified as a muon if detected in both layers of tracking detectors (Iarocci and drift tubes, respectively) upstream and downstream a block of iron ($\approx$ 1 m thick).

The Trigger

The trigger initiates the data acquisition. A trigger is identified via the geometrical properties of the scattering muon track and of the energy deposited by the produced hadrons in HCAL1 and HCAL2. The muon track is reconstructed with dedicated scintillator hodoscopes placed all along the experiment. A different trigger calibration allows quasi real photon events ($Q^2 < 1$ GeV^2) and inclusive deep inelastic scattering events ($Q^2 > 1$ GeV^2) to be distinguished. For the

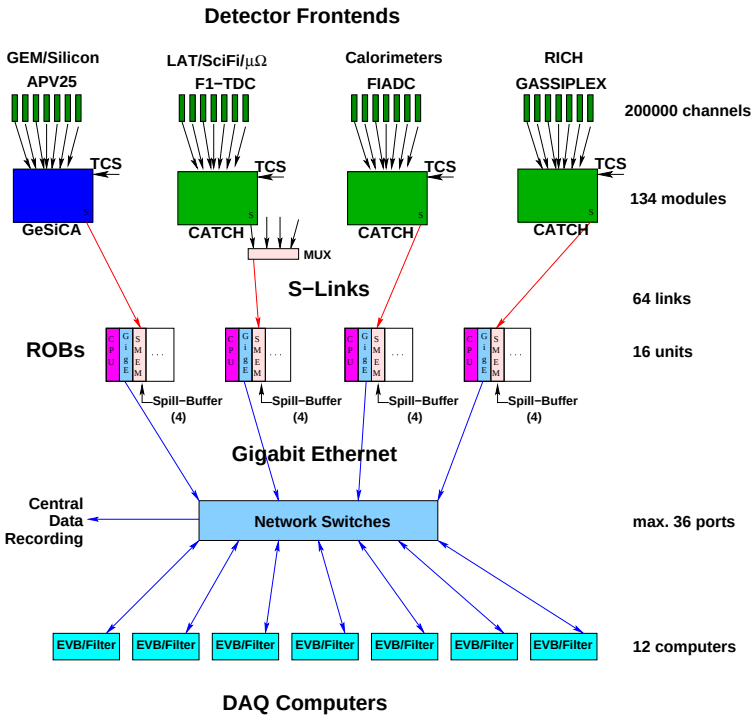

Figure 1.6: The DAQ architecture: the data from the detectors are first collected from the detector frontends, then transmitted to the DAQ computers, where they are combined in one event block and transferred to the central data recording.

hadron program, additional information from the electronic calorimeters will be used in the trigger.

The Detector AcQuisition system (DAQ)

The COMPASS detector contains approximately 190000 detectors channels. The trigger rate goes from 4 kHz to the maximum design frequency of 100 kHz. The event size is on average 50 kByte, therefore the data rate goes from 200 to 4000 MByte/s. In order to cope with such high data rate, the peculiar structure of the SPS spill is used. During the 4.8 s of extraction, the data are read out and buffered; the data are transferred in the following 12 s. This method uses the whole SPS cycle for the data acquisition, obtaining a smaller peak data flow. Fig. 1.6 shows the DAQ architecture.

The signals from the different detectors are read out from the detector frontends at each trigger. The readout modules (*CATCH* and *GeSiCA*) collect the data from several frontends and transfer them via optical connections to the DAQ computers, called **R**ead **O**ut **B**uffer (*ROB*). The ROBs host PCI cards called *spillbuffers*

where the data are buffered. From the spillbuffers the data are transferred via Gigabit Ethernet to the *Event Builder* computers, where the informations from the various detectors are combined in one event block and transferred to the CERN's central data recording system. A complete view of the COMPASS DAQ can be found in [Sch03].

The DAQ computers also perform the *online filtering*. It consists of a rejection of triggered events which do not have a certain topology. The information from the detectors upstream of the target are analysed: if a definite number of planes show a signal with coherent time evolution, the event is accepted. In this way interesting topologies can be tagged and events with a large pile-up of tracks from off time events or secondary interactions can be suppressed, reducing the number of events to record to tape. During the 2003 run, the online filter was used only to tag, while in 2004 it is actively used to filter the events. A complete description of the online filter and its performances can be found in [Nag05].

The Data Control System (DCS)

During operation, the DCS monitors and controls the COMPASS setup parameters such as the high and low voltage systems, gas supplies, slowly varying parameters like pressure, temperature, etc. The DCS uses a commercial SCADA[2], called PVSS.

1.2.3 Processing of COMPASS data

As illustrated in the previous section, the data from the detectors are collected via the DAQ. The informations corresponding to the same primary interaction in the target are then collected in one unique event block and transferred to the central data recording were they are stored on tape on a storage facility called *CASTOR* (**C**ern **A**dvanced **S**torage **M**anager) [CAS].

At this level, an "event" is a collection of raw informations from the detectors and has a typical size of $\sim$ 40 Kbytes. Before a physics analysis can be performed on the data, they have to be processed in order to reconstruct the topology of the event (tracks, vertices, momenta, particle identification) from the detectors' informations. This task is performed by the **CO**mpass **R**econstruction and **A**na**L**ysis (*CORAL*) program. After the reconstruction and processing, the size of one event becomes about 4 Kbytes, that means a reduction to 10% respect to the original event size. The standard output of CORAL is a **D**ata **S**ummary **T**ape (*DST*) file

[2]Supervisory Controls and Data Acquisition system

that contains the fully reconstructed events. The physics analysis is done with the package **PH**ysics **A**nalysis **S**oftware **T**ools (*PHAST*).

CORAL

CORAL is a C++ based software package that reconstructs the event topology from the detectors' raw data. This process can be divided in four steps: decoding, clusterisation, tracking, vertexing.

- **Decoding:** A unique hardware identifier is assigned to each detector's channel in COMPASS. This identifier is related to the frontend modules used for the readout of the channel. The correspondence between identifier of the channel and the name of the detectors to whom the channel belong is stored in the *mapping files*. As first step of the data processing, CORAL extracts the hit channels from the raw data and locates them with the help of the mapping files.
- **Clusterisation:** When a particle crosses a detector, it eventually creates signals on many neighbouring channels. CORAL combines these signals, eventually amplitude-weighted, in a "cluster", whose centre represents the impact point of the particle, and finds its spacial coordinates in the COMPASS reference system.
- **Tracking:** At this point the hits have to be combined to reconstruct the tracks. This is done in two steps: at first the experiment is divided in five zones in which the tracks are assumed to be straight (no magnetic fields, little multiple scattering) and straight lines are reconstructed; then the track segments from two neighbouring zones are fit together taking in account the bending due to magnetic fields or the deviation due to the multiple scattering.
- **Vertexing:** As last step, CORAL analyses the tracks to find if they can originate from a common vertex. This would suggest that the particles, which the tracks are associated with, were produced in the same interaction. Tracks are assumed to originate from one vertex if this is consistent with their geometry and kinematics. The vertex position is the average of the points of closest approach of the tracks.

PHAST

PHAST [PHA] is a software package based on C++ and ROOT developed for the COMPASS physics analysis. PHAST can read the raw data as well as the DST

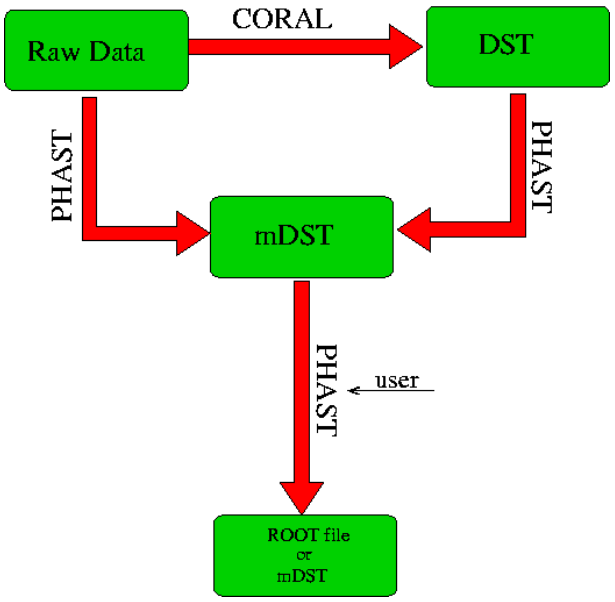

Figure 1.7: A schematic view of the data processing flow. For a detailed description see text.

files. It has a specific output format, the **m**ini **D**ata **S**ummary **T**ape (*mDST*). A mDST contains two different types of informations: the setup informations, like magnetic field maps, material maps, detector geometrical informations, stored in the *PaSetup* object; the event informations, like reconstructed particles and vertices, stored in the *PaEvent* object. The typical size of a mDST event is 1.2 KBytes, which means a further reduction respect to the DST event size. PHAST additionally rejects the events with none reconstructed vertex. Overall, the data volume is reduced to $\sim$ 1% in mDST compared to the raw data.

PHAST contains also a section with specific functions that can be modified by the user in order to read the mDST data and accomplish his/her own physical goals. The user can access the reconstructed events in the mDST files, select events with the desired characteristics and reconstruct physical observable like invariant masses, kinematic variables, etc. . The output can be either a ROOT file, to be further analysed with the standard ROOT frame, or a mDST file, that can be reprocessed with PHAST if more informations about the events are required. Fig. 1.7 the different steps of the data processing.

PHAST was used in this work for the analysis of strange particles described in Chap. 5.

Monte Carlo simulations

A better understanding of the detector performances is achieved with Monte Carlo simulation. The detector simulation is done in **COM**pass **GEANT** (*COMGEANT*). It is an interface to the GEANT3.21 program which is a currently frozen version of the CERN simulation package GEANT. It was developed for the WA89 experiment and has been upgraded to be used also for COMPASS.

The events are generated by programs called *event generators* (PHYTIA, LEPTO, etc.). COMGEANT calculates the output of the spectrometer to a certain event. The COMGEANT output file can be processed with CORAL and analysed with PHAST like a normal data file. The advantage of simulated data is that they contain also the original informations of the events, like which particles were generated, their momenta, position, etc.. Monte Carlo data are used to reconstruct interesting quantities, like efficiency, resolution, etc.. For example, the ratio of the number of Ξ particles reconstructed in the analysis and the number of Ξ in the event generator's file is the efficiency of the system (detector+analysis) for the Ξ. This method will be used in Chap. 5 for the calculation of the Ξ^{0*} and Ξ^{-} efficiency.

Chapter 2

The basic principles of silicon detectors and the Lazarus effect

Silicon detectors belong to the most precise tracking detectors for charged particles in high energy physics experiments. They have an excellent space resolution (few micrometers) and neighbour tracks separation, their signal collection time is short ($\sim$ 10 ns) and for a thickness of 300 μm it has only 0.3% radiation length, that is an extremely small value for tracking detectors. They have already contributed significantly to the study of the τ lepton [PER75], of charm and beauty quarks and, last but not least, to the discovery of the top quark [Erl95].

The radiation causes an appreciable deterioration of the performance of silicon detectors. In the planning phase of COMPASS a significant degradation of the signal to noise ratio after one year of data taking was estimated, which is not tolerable for the envisaged operation lifetime.

The radiation tolerance of silicon devices and of their read-out electronics is therefore of big interest and led to intense effort for the development of radiation hard techniques. One of those, discovered at CERN by the *RD39* collaboration, concerns the recovery of irradiated silicon detectors when operated at low temperature (around 130 K).This effect was called *Lazarus effect* and it is exploited in the COMPASS experiment.

In this chapter the basic operational principles of silicon detectors will be illustrated. Additionally, a review of the mechanism of radiation damage and of the Lazarus effect will be given.

2.1 Silicon microstrip detectors

2.1.1 Basic features

Energy loss

When a charged particle crosses a semiconductor medium it looses part of its energy, mainly via electromagnetic interactions with the atomic electrons. If the energy gained in the interaction is sufficient, the electron will move from the valence band to the conduction band leaving behind a hole, or missing electron. The atom in the lattice is ionised and an electron-hole pair is created. The energy E_g needed to create an electron-hole pair in silicon is 3.6 eV at 300 K and 3.8 eV at 77 K, where a third of it is used by the electron to overtake the energy gap and the rest is absorbed by lattice excitations. This threshold value is really low if compared for example with the ionisation energy in a gas ($\mathcal{O}$(10 eV)), making the silicon a highly suitable material for particle detection. It is important to notice that even though the thermal energy at room temperature ($kT = 8.617 \times 10^{-5}\ eV/K \cdot 300\ K \sim 26$ meV, where k is the Boltzmann constant) is only $\sim$ 7% of E_g, it is high enough to create many electron-hole pairs. A detailed description of the process can be found in [Bic72] .

The Bethe-Bloch formula provides the average energy loss of the crossing particle per unit length $\mathrm{d}E/\mathrm{d}x$ as a function of energy or momentum:

$$-\frac{\mathrm{d}E}{\mathrm{d}x} = 2\pi N_A r_e^2 m_e c^2 \rho \frac{Z}{A}\frac{z^2}{\beta^2}\left[\ln\left(\frac{2m_e\gamma^2\beta^2c^2W_{max}}{I^2}\right) - 2\beta^2 - \delta\right] . \qquad (2.1)$$

where r_e and m_e are the classical electron radius and mass, N_A is Avogadro's number, I is the mean excitation potential, Z, A and ρ are the atomic number, the mass number and the density of the absorbing material respectively, z is the charge of the incident particle in units of e, βc its velocity and W_{max} the maximum energy transfer in a single collision. δ is the so-called density effect correction (see for example [Leo94]). This formula has a minimum for particles with $\beta \sim 0.96$ which are then called *Minimum Ionising Particles* (MIP). From this point on the $\mathrm{d}E/\mathrm{d}x$ change slowly with increasing the energy, then the particles are still considered MIPs. In Fig. 2.1 the Bethe-Bloch formula for protons, pions and muons in different materials is depicted.

The mean energy deposited according to the equation 2.1 coincides with the most probable deposited energy only for thick detectors. For thin detectors ($d \lesssim 10$ cm for incident pion of $\sim$ 120 GeV) the probability of interactions with high energy transfer is strongly reduced and the average energy loss is higher than the most

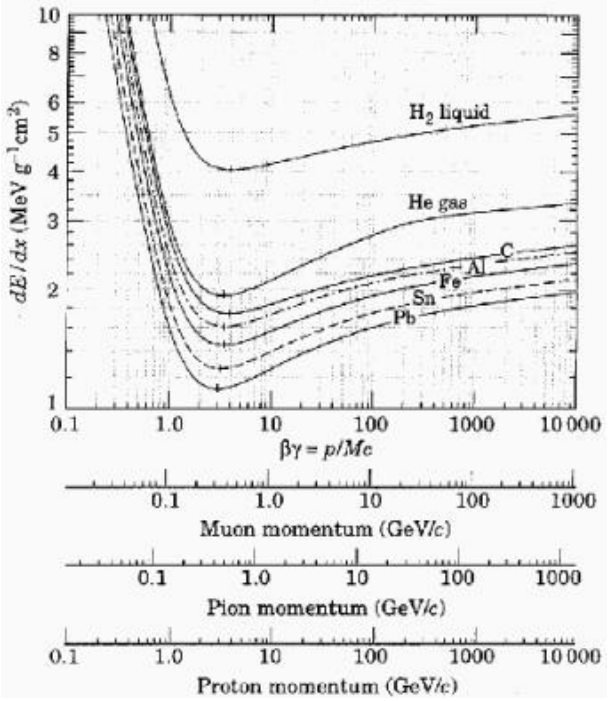

Figure 2.1: The energy loss in different materials as function of the momentum of the incident particle, described by the Bethe-Bloch formula

probable one. In this case the probability distribution of the energy loss is well described by a Landau curve, which is asymmetric with a long tail towards the high values, being however rare events with high energy loss. From this distribution one finds that the most probable energy loss of a MIP in a silicon detector of 300 μm thickness is $\sim$ 86 keV, producing $\sim$ 24000 electron-hole pairs.

p-n junction

Once the crossing particle has created a certain number of electron-hole pairs, they have to be extracted in order to determine the passage of a particle. A solution is to bring to contact two bulks of *p*- and *n*-doped silicon (diode-principle). When thermal equilibrium is established, a certain number of free charge carriers from the *p*- and *n*- region recombine. The junction region is then depleted of charge carriers and a potential difference is built up (*built-in* voltage). It is possible to increase the depth of the space charge region applying an external reverse bias voltage. The size of the depletion region is given by:

$$W = \sqrt{2\epsilon(V + V_{\text{bi}})/N_{\text{eff}}\, e} = \sqrt{2\rho\mu\epsilon(V + V_{\text{bi}})} \tag{2.2}$$

where W is the thickness of the depleted region, V the external bias voltage, V_{bi} is the *built-in* voltage, N_{eff} the effective doping concentration, e the electronic charge, ϵ the dielectric constant, ρ the resistivity and μ the charge carrier mobility [PDG00a].

An asymmetric dopant concentration allows the depletion region to be more extended on one side of the junction. A typical configuration is a small (few μm) highly doped p-region, so called p^+, on a n-doped bulk (some hundreds of μm). Usually n-doped material is used as bulk, for the mobility of its free charge carriers (electrons) is higher than in the p material, allowing a bigger depletion region with the same bias potential (Eq. 2.2).

The conductive p and n regions together with the depleted volume form a capacitor with the capacitance:

$$C = \epsilon A / W \tag{2.3}$$

where A is the area of the diode.

Leakage current

Even when the p-n diode is operated in reverse bias, a small leakage current is present, due to the thermal creation of electron-hole pairs. In order to identify the passage of a particle through the detector, the signal generated has to be higher than the leakage current, being the latter the noise of the detector. The leakage current I_{leak} depends linearly on the width W of the depletion region:

$$I_{\mathrm{leak}} \propto W \propto \sqrt{V} \tag{2.4}$$

Equation 2.4 shows that when the detector is fully depleted the leakage current saturates.

Change of silicon properties with the temperature

Reducing the operation temperature of a silicon detector reduces the thermal energy of the atoms in the lattice. This affects mainly two quantities which are significant for using the silicon as a particle detector [Rug99]:

- *leakage current* I_{leak} due to its origin, it has a strong dependence on the temperature: a decrease of the temperature is reflected in a reduction of the

number of electron-hole pairs created by thermal excitation. As consequence the noise of the detector decreases with the temperature.

- *mobility of the free charge carriers* it increases with decreasing temperature. This fact has two important consequences: as first the resistivity of the semiconductor increases, permitting to fully deplete the detector with a smaller bias voltage with respect to room temperature (Eq. 2.2); then the saturation value for the free charge carriers velocity is reached at a lower voltage. The observable effect is that the signal becomes faster and the change is more significant for the holes.

This means that also a non damaged silicon detector can benefit from being operated at low temperature.

2.1.2 Particle detection

Principle of operation

A silicon detector works like a *p-n* diode operated under reverse bias. When a particle crosses the depleted volume, it ionises the atoms of the lattice, creating electron-hole pairs. These are separated by the electric field applied and drift through the electrodes, where a signal is observed. There is no charge multiplication inside the silicon volume.

A silicon detector widely used in high energy physics is the microstrip detector. It is constituted of a *n*-type high resistivity substrate ($\rho_n > 1$ KΩcm), on which highly doped p^+ strips are implanted, forming a junction matrix. A typical distance between the strips is ~ 50 μm. On the backside there is an homogeneous implantation of highly doped n^+ silicon. The electrons created by the crossing particle are collected on the strips close to the impact point on the detector, providing a one dimensional information with a typical resolution of some μm. The detector is then coupled to the read-out electronics either directly (*DC coupling*) or with a silicon oxide layer in between (*AC* or *capacitive coupling*).

It is possible to achieve a double sided read-out segmenting the n^+ side as well as the p^+ one. In this case the holes will be collected on the n^+ strips arranged orthogonally to the p^+ ones. The double side read-out provides an information on the two-dimensional position of the impact point, minimising the amount of material the particle has to cross.

Spatial resolution

As already mentioned the silicon detectors can have a really good space resolution. The reasons are the small size of the charge clouds (a Gaussian distribution with $\sigma \sim 10$ μm), and the processing technology which permits to segment the readout strips down to ~ 10 μm pattern [Pei92].

If the charge cloud is completely collected on one strip, the centre of the strip gives the position measurement, while the resolution is given by $\sigma_x = \delta_x/\sqrt{12}$, where δ_x is the strip pitch and σ_x is the second moment of a constant distribution of width δ_x. If instead the charge cloud is distributed on more than one strip, the centre of the cloud can be estimated with much higher precision, fitting, for example, the charge distribution on the strip with a Gaussian function.

Time resolution

The mobility of charge carriers in the silicon is 1350 and 480 cm^2/Vs for electrons and holes, respectively. This means that the collecting time of the signal is of the order of few ns, for a typical thickness of 300 μm. It is possible to decrease the collecting time increasing the bias voltage over the full depletion value (*overdepletion*). The limit of this operation is the diode breakdown.

The signal shape of the detector is a convolution of the collecting time of the detector and of the characteristic time of the read-out electronics, being usually the latter the dominant contribution. In the next chapters a method for improving the time resolution of the COMPASS silicon detector will be described. For the moment let's just mention that values down to 4ns could be achieved.

Charge Collection Efficiency

The *charge collection efficiency (CCE)* is the ratio between the charge created in the silicon bulk by a crossing particle and the charge collected. This ratio depends on the depth of the depletion region, since in the not depleted region the charges created by a crossing particle can recombine with the free charge carriers. For a fully depleted detector the CCE is $\sim 100\%$. It is worthwhile to mention here that the exposure of detector to radiation reduces its CCE, according to a mechanism which will be described in the following section.

Noise

A correct estimation of the noise of a detector must consider the intrinsic noise of the detector itself and the noise introduced by the read-out electronics. The first term is constituted by the leakage current, as explained in Sec. 2.1.1. The second term is related to the capacitance of the detector as it is seen by the preamplifier. This quantity can be expressed as *Equivalent Noise Charge* (ENC) to permit an easier comparison with the signal, that it is usually expressed in term of number of electrons. The ENC from the readout electronics can be written as:

$$ENC = a + bC \tag{2.5}$$

where C is the load capacitance and a and b are parameters of the preamplifier.

2.2 Radiation damage

Radiation damage in silicon detectors can be divided into surface and bulk damage. In the following only the bulk damage will be discussed, being the most relevant contribution for minimum ionising particle detectors.

2.2.1 Defects in silicon

Damage mechanism

The bulk damage produced in silicon detector by high energy particles is caused primarily by elastic collision of the latter with lattice atoms. If the energy transferred to the silicon atom is high enough to displace it out of the lattice (*primary knock on atom*, PKA) a Frenkel pair is created, that is an interstitial atom and a left over vacancy. The energy needed to create a Frenkel pair is $\sim$ 25 eV. The energy of the recoil atom can of course be much higher (for example, a muon of 160 GeV can transfer up to $\tilde{2}$ GeV to a PKA) and the PKA can either ionise other atoms or remove them from their position in the lattice, creating a cascade of dislocated atoms. The non-ionising processes are predominant when the atom looses its last 5-10 keV. Then, at the end of each heavily recoiled atom path a cluster of defects is created, as displayed in Fig. 2.2.

The displacement of several silicon atoms from their position in the lattice is not the end of the damage process. Interstitial atoms and vacancies are very mobile in the silicon lattice. Therefore about 90% of the vacancies produced annihilate

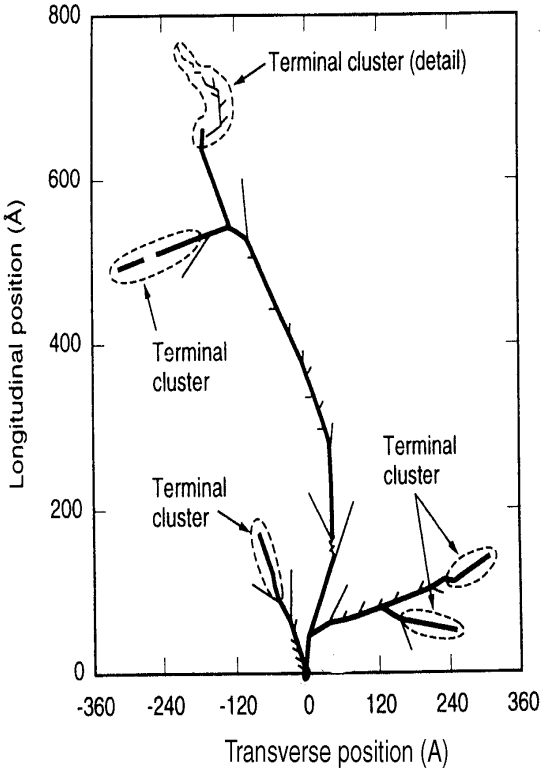

Figure 2.2: Monte Carlo simulation of the track of a PKA with formation of clusters of defects.

with interstitial silicons and no damage remains (see Sec. 2.2.3). The time scale of this process is $\mathcal{O}$(10 minutes). The remaining 10% migrate through the lattice and combine either with each other or with the impurity in the silicon creating a wide variety of defects. These are called *point defects* and they are, together with the cluster defects, the origin of the bulk damage. Their electrical properties results in the macroscopic deterioration of the detector properties. For a more detailed classification of defects see [Mol99].

The NIEL scaling hypothesis

In order to compare the defects created in the silicon by different particles, the *Non Ionising Energy Loss* (NIEL) hypothesis can be assumed. Its basic assumption is that the amount of defects induced in the bulk is proportional to the amount of energy released by the particle via non ionising collisions with the lattice atoms. Usually the fluence of neutron of 1 MeV is chosen as unity. To scale a certain fluence Φ_{meas} to its $\Phi_{\text{eq}}^{1\,\text{MeV}}$ one can use the relation:

$$\Phi_{\text{eq}}^{1\,\text{MeV}} = k\Phi_{\text{meas}} \tag{2.6}$$

k is called *hardness factor* and it is defined as

$$k = \frac{1}{D_{\text{n}}(1\text{ MeV})} \cdot \frac{\int_{\text{E}_{\text{min}}}^{\text{E}_{\text{max}}} \text{d}E_{\text{p}}\phi(E_{\text{p}})D(E_{\text{p}})}{\int_{\text{E}_{\text{min}}}^{\text{E}_{\text{max}}} \text{d}E_{\text{p}}\phi(E_{\text{p}})} \tag{2.7}$$

where $\phi(E_{\text{p}})$ is the energy spectrum of the particle p, E_{p} is its kinetic energy and $D(E_{\text{p}})$ is the *displacement damage cross section* whom behaviour as function of E is shown in Fig. 2.3. For neutrons of 1 MeV, the displacement damage cross section is 1 and D_{n}(1 MeV)= 95 MeV·mb.

2.2.2 Effects of the radiation on the properties of the detector

The final bulk damage of a silicon detector is produced by thermally stable point defects and clusters. Due to these defects, new energetic levels for electrons and holes are created inside the forbidden gap between the valence and the conduction energy band. Concerning the properties of the detector, the defects associated to the deep levels are the most pernicious ones, since they have energies in the middle of the forbidden gap.

Macroscopic effects of the defects on the properties of the detector are the change of the leakage current and of the effective doping concentration with the fluence.

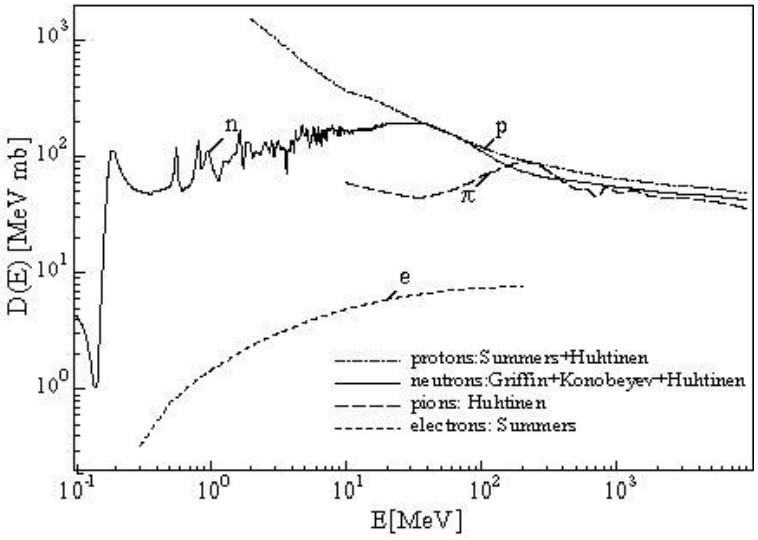

Figure 2.3: Displacement damage cross section for different particles as function of energy

- **leakage current** As mentioned in Sec. 2.1.1, the leakage current is the origin of the noise of the detector. If intermediate energy levels are created in the forbidden gap, more electron-hole pairs are generated due to thermal energy. It was experimentally observed that the leakage current in an inversely biased detector increases with the fluence as

$$\Delta I = I(\phi) - I(\phi = 0) = \alpha V \phi \tag{2.8}$$

  where α is the damage factor which is $\sim 6 \cdot 10^{-17}$ A cm^{-1} for neutrons of 1 MeV and V is the sensitive volume of the detector.

- **effective doping concentration** The effective doping concentration N_{eff} in a non irradiated semiconductor is defined as

$$N_{\text{eff}} = |N_{\text{D}} - N_{\text{A}}| \tag{2.9}$$

  where N_{D} is the donor concentration and N_{A} the acceptor concentration in the space charge region. The defects created by the irradiation with levels in the forbidden energy gap can capture and emit electron and holes, acting as dopants. They can be classified as *donors* or *acceptors* if neutral or negative, respectively when occupied with an electron. The defects, then, change the doping concentration. Since the number of defects is a function of the fluence ϕ, in irradiated detectors N_{eff} changes with ϕ. For a better

understanding of the phenomenon it is useful to consider the case of a detector with $n-$type bulk. A $n-$type silicon bulk is doped with donors; the space charge region is positive and the free charge carriers are electrons. When irradiated, donors and acceptors defects are created. The levels are filled with the free electrons; donors become neutral and acceptors become negative, decreasing the total charge of the bulk. On top of this, the *donor removal* process, due to the passification of donor dopants when reacting with defects, reduce further the total charge. The N_{eff} decreases and, after the detector has been enough exposed, the $n-$bulk material will change to $p-$type. After the type inversion, N_{eff} and the depletion voltage (Eq. 2.2) increase until the diode breaks down. Since $W \propto 1/\sqrt{N_{\text{eff}}}$ and $\rho \propto 1/N_{\text{eff}}$ (Eq. 2.2), the depth of the space charge region W and the resistivity ρ decrease with increasing the fluence.

The variation of N_{eff} with the ϕ can be expressed as

$$N_{\text{eff}} = |N_{\text{D}}\, e^{-c\phi} - N_{\text{A}} - \beta\phi| \tag{2.10}$$

where c and β parametrise the change of donors and acceptors concentration, respectively. For a $n-$type material with standard doping concentration, the type inversion takes place for fluences $\sim 10^{14}\text{cm}^{-2}$.

From the detection point of view, an increase of the leakage current corresponds to an increase of the noise, which reduces the performances of the detector. Furthermore, increasing the effective doping concentration means an higher bias voltage has to be applied to the detector in order to reach the full depletion. For very high damaged detector, the voltage needed for a complete depletion can be higher than the breakdown voltage of the *p-n* junction. As described in section 2.1.2, if a detector is not fully depleted its charge collection efficiency (*CCE*) is smaller than 100%.

To summarise, the radiation damages the lattice structure of the silicon, creating intermediate energy levels between the valence and conductive bands. These levels modify the macroscopic properties of the silicon, degrading its performances as particle detector. When the amount of radiation the detector undergoes is too high, the degradation is such to make the detector no longer usable.

2.2.3 Annealing

As mentioned in the previous section, the effective doping concentration N_{eff} in a silicon detector changes with the fluence. After the irradiation the N_{eff} still

changes, due to the reorganisation of the defects. The defects migrate through the silicon lattice until they recombine with their counterpart of form new defects by assosiation with other defects or impurities. This phenomenon is called *auto-annealing*. Right after the irradiation, N_{eff} decreases (*beneficial annealing*) and after few days N_{eff} starts to increase again (*inverse annealing*). The inverse annealing can last for years until N_{eff} reaches a saturation value. Keeping the detector at higher or lower temperature with respect to the room temperature can speed up or slow down the inverse annealing, but it does not change the saturation value.

For a detailed review about silicon detectors see [Pei92] and [Mol99].

2.3 Lazarus effect

As discussed in the previous chapter, the radiation damage poses an harsh limit on the life time of silicon detectors. Different ways of improving the overcoming the problem are under study. Between them, it is worthwhile to mention the implementation of multiple guard rings structures on the silicon wafer, which ensures better performances at high bias voltages [Abt96]; and, as defect engineering, an improved radiation hardness of the silicon bulk when enriched with oxygen at high concentration [ROSE].

An alternative approach to the problem was envisaged by the *RD*39 collaboration [RD39w]. Instead of avoiding the formation of radiation induced defects, these latter were electrically passified by reducing the thermal energy. The effect was a revival of highly damaged silicon detectors when operated at cryogenic temperatures. This phenomenon was named *Lazarus effect* after the biblical tale.

The Lazarus effect was already exploited in the *NA50* experiment [NA5] at CERN Proton-Synchrotron and will be used in the *TOTEM* experiment [TOTEM] at the Large Hadron Collider at CERN.

2.3.1 Experimental evidences

The first experimental evidence of the Lazarus effect was observed in 1998 [Laz98]. In Fig. 2.4 the corresponding plot is shown: the CCE recovery is clearly observed in the temperature scan. For the detector irradiated by $\phi = 1 \cdot 10^{14}$ and operated at the reverse bias voltage $V = 100$ V, the signal amplitude reaches its maximum at $T_{\text{m}} = 130$ K, with a CCE which passes from $\sim 20\%$ at 180 K to $\sim 90\%$ at 130 K . The recovery is also evinced at higher fluences and different bias

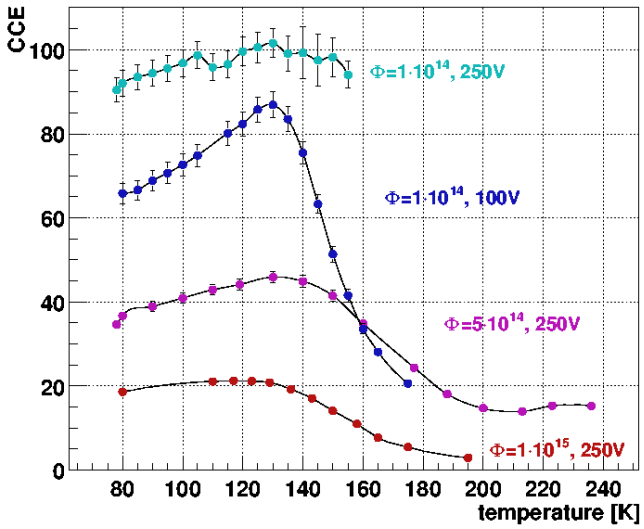

Figure 2.4: The variation of the charge collection efficiency (in percentage) as function of temperature for detectors irradiated with different fluences

voltages. The value of T_m does not depend on the fluence, whereas the maximum of the CCE decreases with increasing fluences.

After this first evidence, further studies were performed for a full characterisation of the phenomenon. It was found that the recovery of the CCE is not influenced by the temperature at which the detector was stored after the irradiation. Additionally, no significant differences were found when the silicon detectors are irradiated while operated at cryogenic temperatures [Cas01].

Including the benefits of a low temperature operation described in Sec. 2.1.1, one can conclude that a longer life time for silicon detectors operated in high radiation environment can be achieved decreasing the operation temperature down to 130K. In this way complications concerning wafer growth and design are avoided, but the challenge become the infrastructures needed for cryogenic operation.

2.3.2 The Lazarus effect model

There are two possible reasons for the degradation of the CCE in irradiated detectors:

- charge loss due to the trapping of carriers by deep levels created during the irradiation, as mentioned in Sec. 2.2.2.

- partial depletion of the detector.

Contribution of charge loss (CCE_t)

The intermediate energy levels created by the radiation act as trapping centres for the electrons and holes created by an ionising particle. The electrons and holes can be detrapped: let τ_{trap} be the time constant of the trapping-detrapping process. If τ_{trap} is smaller than the collection time of the charge t_{coll}, the charge can be collected in spite of the traps and the final signal is not affected. If $\tau_{trap} \gtrsim t_{coll}$ the total charge created by the ionising particle is collected in a longer time or is partially lost, and as a consequence the CCE is deteriorated. The relative charge collection efficiency factor related to the carrier trapping, CCE_t, is defined as

$$CCE_t = 1 - K[1 - exp(-t_{coll}/\tau_{trap})] \tag{2.11}$$

where $K = 1/3$ for MIPs [Laz]. The time dependence of Eq. 2.11 arises only from the dependence of τ_{trap} from the temperature, whereas t_{coll} is constant due to the saturation of the drift velocity (Sec. 2.1.1)

Contribution of the depletion depth (CCE_g)

For MIP detection, the CCE term originating from a geometrical factor (CCE_g) is

$$CCE_g = \frac{W^2}{d^2} \tag{2.12}$$

where W is the space charge region depth and d the detector thickness. W depends on the effective doping concentration N_{eff} (Eq. 2.2), then studying the dependency of N_{eff} from the temperature is possible to extrapolate the behaviour of CCE_g.

CCE Vs. Temperature

The total CCE can be written as

$$CCE = CCE_t \cdot CCE_g \tag{2.13}$$

It can be demonstrated that CCE_g is more sensitive to the temperature than CCE_t.

The experimental results on the CCE recovery can be then explained as following: the effective doping concentration N_{eff} decreases when decreasing the temperature; the ratio W/d then increases and hence the total CCE increases. When the detector is fully depleted $W/d = 1$ and the CCE_{g} stays constant when decreasing further the temperature. For $T < T_{\text{L}}$, where T_{L} is the temperature where the CCE has a maximum, the CCE_{t} becomes then the leading term: in this temperature interval the trapping constant τ_{t} decreases and correspondingly the CCE decreases.

A more complete explanation of the Lazarus effect is given in [Laz].

Chapter 3

The implementation of silicon detector in COMPASS

In this chapter the different components comprising the detector are explained. At first the silicon detector design, then the elements of the read-out chain are depicted. The last part of the chapter describes the cryostat, the liquid nitrogen distributor and an overall view of the complete apparatus.

3.1 The silicon detector in COMPASS

Until the 2003 run, silicon detectors were used only as beam tracking devices in the region upstream of the target. This was due both to the fact that in the muon program the space between the target magnet and the first spectrometer magnet was small thus leaving little space for tracking devices, and that such a high space resolution as provided by silicon detectors was not as mandatory for this physics program as for the hadron program.

During the 2003 run, three silicon stations and two scintillating fibre stations were installed upstream of the target, in order to provide excellent space and time resolution for the reconstructed beam tracks. The Fig. 3.1 shows the arrangement of different stations upstream of the target.

As mentioned in chapter 1, COMPASS has a high beam intensity and high trigger rate ($\sim 10^8$ particles/s; up to 100 kHz), which imposes the usage of fast readout electronics. This is especially true in the case of silicon detectors, since each detector is exposed to the full intensity beam.

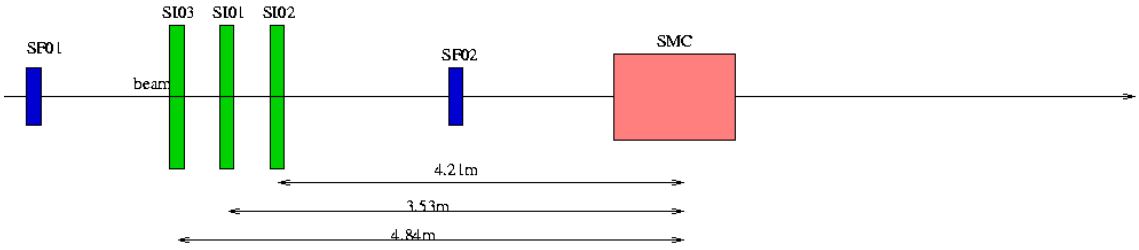

Figure 3.1: Detector arrangement upstream of the target: SF are scintillating fibre stations, SMC is the target magnet, SI are the silicon stations. SI01 and SI02 are mounted on a common support, while SI03 is on a separate bench.

3.2 The detector design

The silicon detectors used in COMPASS were originally designed for the HERA-B experiment. They were designed by the Halbleiter-Labor (HLL) of Max-Planck-Institut für Physik (München). The wafers used in COMPASS were part of a batch produced by SINTEF (Oslo, Norway) [Ber97]. From the geometrical point of view, they were identical to the original HLL design, but presented some slight technological differences with respect to it. For information about the HERA-B detector performances see [Abt99].

3.2.1 Processing characteristics

The detectors are processed on a 280 μm thick, n-type substrate, 2-3 kΩ cm resistivity wafers. The active area is 5×7 cm^2. The read-out pitch is 54.6 μm and 51.7 μm for the n- and p- sides respectively. On both sides, intermediate strips are present in order to improve the spatial resolution by charge division readout. The detector cross section is shown in Fig. 3.2.

The p-side is divided into 1024 strips, inclined at 2.5° with respect to the wafer edge; the n-side presents 1280 strips, perpendicular to the p-side strips. The reason of this peculiar arrangement will be clarified in the next section.

The readout strips on the p-side are naturally insulated from each other by the n-type silicon bulk, while the n-side (ohmic-side) requires more complicated designs for electrical isolation between the strips. In the case of the HERA-B silicon detectors, the $p-stops$ technology was used. It consists of highly p^+ doped compensation implantation silicon arranged between the n^+ readout strips.

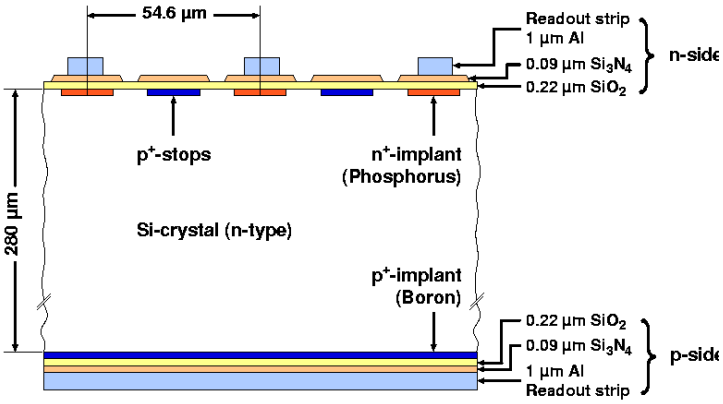

Figure 3.2: Cross section of the silicon detector. Details in Sec. 3.2.1

3.2.2 Geometry

Since multiple scattering contributions dominate the spatial resolution in microstrip silicon detectors, a reduction of the amount of material used is convenient. As a consequence double-sided silicon detectors are preferable, that provide information regarding two spatial coordinates with the same amount of material required for a single-sided readout.

Placing two double-sided detectors close together, allows the measurement of 4 independent projections providing the strips are not parallel, so that ambiguities in multi-hit events can be disentangled and ghost hits (noise above the signal threshold) can be rejected. As mentioned in the previous chapter, there is a 2.5° stereo angle between the strips and the detector edge. Putting two detectors back-to-back (a so-called station) will result 5° angle between strips on corresponding sides of the detectors, as shown in Fig. 3.3.

This design enables the largest possible overlap of the two detectors and, at the same time, the use of the same wafer design for both detectors in one station.

In the COMPASS coordinates system, one detector will give the x and y projections (inclined of 0° and 90°) and the inclined coordinates (with an angle of $-5°$ and 85°, respectively) are called the u and v projections.

3.2.3 Radiation hardness

Due to the high fluences (the detector had to stand in the HERA-B environment up to $3 \cdot 10^{14}/\text{cm}^2$ per year), a dedicated radiation-hard design for the detector

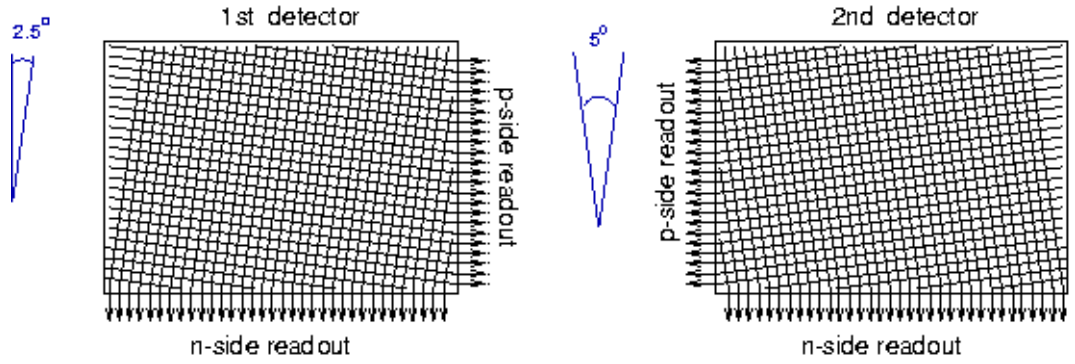

Figure 3.3: Readout strips on the two double-sided detectors mounted in one tracking station

was developed. In the following the different components of the design are illustrated, namely:

- multi guard-ring structure
- capacitive coupling of the readout strips
- polysilicon resistors for strip biasing

Multi guard-ring structure

For a full depletion of a silicon bulk after radiation damage, higher bias voltages than nominal ($\sim$ 90 V) are expected (up to 300-500 V). In order to be able to operate detectors up to such conditions, the sensitive area of the detector is surrounded by a 16 punch-through guard-ring structure on both sides. This structure shields the sensitive area from surface and edge leakage currents and, in addition, provides a controlled and gradual drop of potential from the detector's rim towards the potential of the undepleted substrate.

In Fig. 3.4 a corner of the *n*-side layout is shown.

The detector was tested for stable operation at bias voltage well above 500 V [Abt96].

Capacitive coupling

Due to the large leakage current induced by radiation damage, the readout electronics had to be capacitively coupled to the detector. For this capacitive cou-

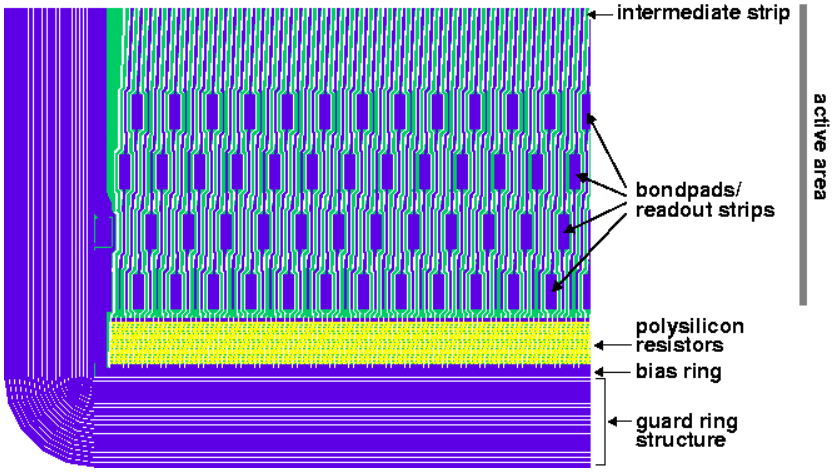

Figure 3.4: Layout of the n-side of the silicon detector (corner)

pling, the aluminium readout lines are separated from the implanted strips by a 220 nm thick layer of silicon dioxide (SiO_2) and 90 nm of silicon nitride (Si_3N_4), as shown in Fig. 3.2.

Polysilicon resistors for strip biasing

Usually the bias voltage for depleting the detector is provided by punch-through contacts to the readout strips. For a highly irradiated detector, this technique is not sufficient as traps, which are created in the punch-through channel, lead to an increase of the noise. Therefore, polysilicon resistors of ~ 1 MΩ were implemented [Ber97].

3.3 The electronics

The signal induced in the silicon by a crossing particle (Chap. 2) has to be collected, amplified and digitised, before being transferred to the COMPASS data acquisition system. A specialised readout chain (Fig. 3.12) has been developed for Silicon detectors, employing features like data reduction algorithms and fast readout. Optical data transmission is used, since the two sides of one detector are read out with the same readout chain, although they are on different potentials due to the bias voltage applied to the detector. Details on the COMPASS readout system and a thorough description of the data reduction algorithms in the ADC are given in [Gru01].

3.3.1 The APV25

As read-out chip the APV25 was chosen. It is an analogue pipeline ASIC [1] intended for the read-out of silicon microstrip detectors in the tracker of the CMS experiment at CERN.

Due to different assembly times, two versions of the chip, named *S0* and *S1*), were used in the COMPASS silicon detectors. Since there are only small differences between the two versions, in the following only the description of one will be given, namely the *S1* version, as it was the version used when the detectors were operated at cryogenic temperatures.

The APV25 is a 128 channel analogue pipeline with 192 columns of analogue storage. Silicon strip signals are amplified into a shaped pulses of characteristic time $\tau_{CR-RC} = 50$ ns and magnitude 100 mV/25,000 electrons. These are sampled at a rate of 40 MHz (that is each 25 ns) and stored in the ring buffer. Useful data are marked after a programmable latency, and held in the pipeline buffer until they can be read out. A 32 deep FIFO holds the addresses of pipeline columns holding marked data. When data is read from the pipeline it is processed using a FIR [2] filter before being read out through an analogue multiplexer. The output signal is a differential current. In Fig. 3.5 the schematic view of the APV25 is depicted.

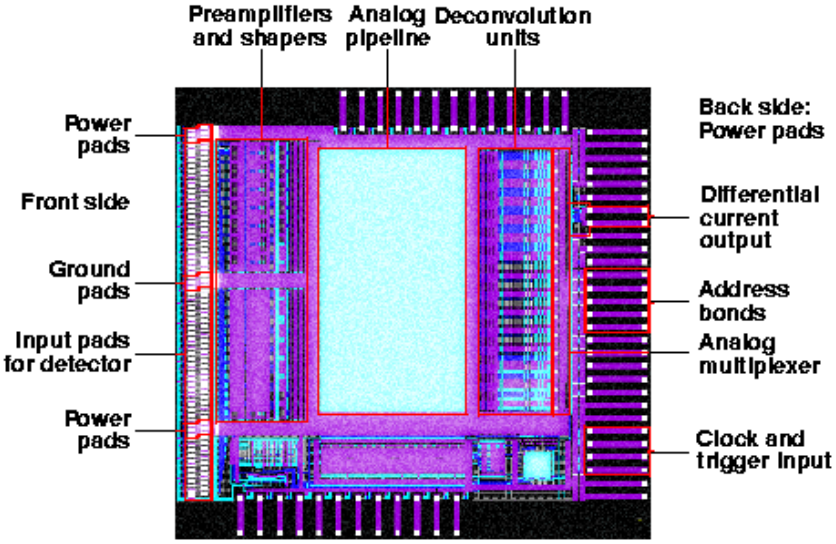

Figure 3.5: Layout of the APV25 read out chip

The output from the APV25 chip is in the range of ± 4 mA. When there is no data to read out, the output is at the logic 0 level, with synchronisation pulses

[1] **A**pplication **S**pecific **I**ntegrated **C**ircuit
[2] **F**inite **I**mpulse **R**esponse

every 70 clock-cycles. When an event is triggered, a data set is then output and is composed of four parts. The first three are digital: a header (three bits at logic 1 level); an address (eight bits) defining the column address used to store the signal; and an error bit. The fourth part is the analogue data set, that is the output of the 128 chip channels read out at the memory location indicated by the address. The analogue dc value (baseline) is programmable to be between the two levels of the digital signal, and the signal gain on top of the baseline is 1 mA/mip.

The Fig. 3.6 shows a typical output frame.

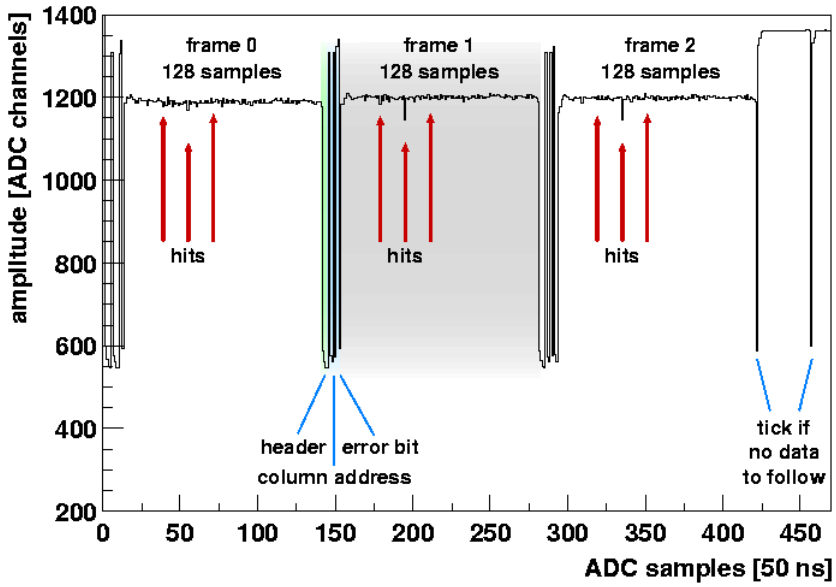

Figure 3.6: Output frame of the APV25 operating in multi-mode

The chip has three modes of operation:

- The *D*econvolution mode is used in normal operation when data rates are sufficiently high such that the effects of pile-up are significant. In this mode, the FIR filter removes the effects of pile-up to confine the signals to one 25 ns interval
- The second mode, *P*eak, is used when pile-up is not significant and a larger signal to noise ratio is required. In this mode the FIR filter acts simply as an amplifier
- The third mode, *M*ulti, can be used when calibrating a pulse shape, and in this mode three multiple consecutive pipeline columns can be triggered and read out without FIR filtering.

For the COMPASS silicon readout, the *M*ulti mode was chosen, in order to improve the time resolution. For a more detailed description of the method used to extract the time resolution with the COMPASS silicon detector see [Wie03].

3.3.2 The L-board

The supporting structure of the detector is composed of two 6-layer PCBs [3]. The wafer is glued between them with a mono-component silicon based non-conductive glue, in order to have access to the readout pads on both sides. The boards also provide pads for the bias voltage of the wafer. The bias voltage on each side of the detector, is fixed to the reference voltage on the corresponding L-boards. That means the two readout sides are on different ground potentials.

For reducing the pickup noise the readout chips are placed as close as possible to the wafer on the L-boards. The readout pads on the silicon are connected via wire bonding to the input pads on the chips. As the patterns for the pads are different on the detector and chips, a pitch adaptor (aluminium wires on a 300 μm thick glass support) is placed between them, to allow straight wire bonding.

Due to the different number of channels on the two sides of the detector, the L-board on the *n*-side hosts 10 APV25, while the one on the *p*-side hosts 8 (see Fig. 3.7).

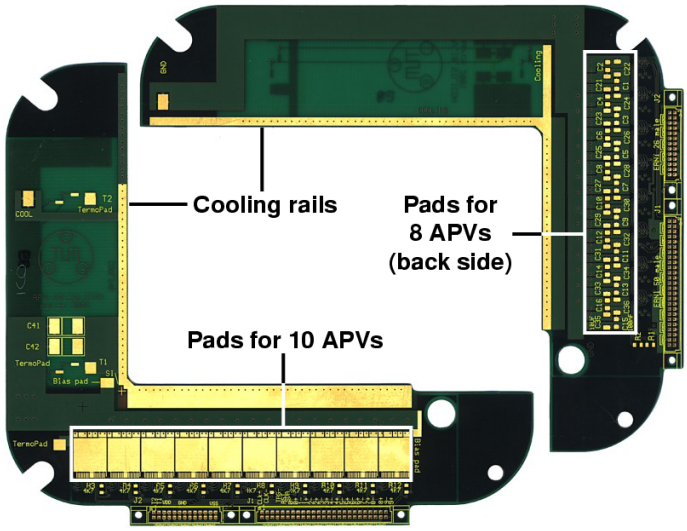

Figure 3.7: Layout of the two L-boards

As mentioned in the previous section, the output of the APV25 is a differential

[3] **P**rinted **C**ircuit **B**oard

current. On the L-boards, the data from each chip are read out through a 4.7 kΩ resistor, in order to convert the current output in a voltage output.

The APV25 chips are very sensitive to noise on the power and grounding lines, leading to oscillations of the baseline in the analogue output. In addition, due to the double-sided operation, there is a cross-talk between the readouts on the two projections via the silicon wafer. This coupling allows the transmission of the noise through the two sides of the readout. To achieve a stable operation at low noise, the power lines were equipped with capacitances directly underneath the chips and across the L-boards for stabilisation and frequency filtering. Right below the pads for the chips, flat cable connectors provide data transmission and power lines, a configuration bus and clock and trigger information. The L-boards also provide the cooling facilities needed for cryogenic operations: Copper-Nickel capillaries ($d_{outer} = 1.6$ mm; $d_{inner} = 1.3$ mm) are soldered on dedicated pads on the back side of the PCBs and are flushed with liquid nitrogen (LN_2), which is used as coolant. The pads are connected via metalized holes to the pads where the wafer is glued. To assure better cryogenic operations, the copper layers inside the PCBs are arranged in such way that the wafer is thermally decoupled from the readout chips as they are an heat source. Each PCB also hosts the readout for two *PT100* thermometers for temperature control on the detector.

3.3.3 The repeater card

A first signal preamplification is done in the *repeater cards*. One repeater board for each side is used. Apart from amplification, the boards provide power for the APV chips, distribution of clock and trigger lines, and an interface for temperature monitoring on the L-boards. In COMPASS, power supply for the repeater boards is provided by floating C.A.E.N. low voltage power modules, which allow monitoring of the currents that the APVs consume. Together with temperature monitoring, these currents proved to be an important tool for checking the chip's status and for remote debugging purposes.

3.3.4 The ADC card

For digitisation of the APV signals, an ADC card for Silicon readout was developed (sg_adc). One card processes information received from the repeater board from one silicon detector side. Digitisation is performed with 10 bit precision. The APV header information is merged with additional event information into a new header and data is sent out via optical fibres. The implemented *Hotlink* protocol permits transfer rates of up to 40 MByte/s on optical fibres.

Modes of operation. The sg_adc provides two modes of operation. In *latch-all mode*, the amplitudes of all channels and all three samples are transmitted to the readout chain. An amount of 9 kB data per event and detector is produced, limiting readout to a relatively low trigger rate of about 1 kHz. To increase performance, dedicated data reduction methods have been implemented for the sg_adc.

Zero suppression & common mode correction. In *sparse mode*, a Xilinx FPGA[4] chip on the card performs pedestal subtraction for each channel.[5] In addition, a correction for collective changes of all pedestals—the *common mode*—due to a baseline shift of individual APV chips is done. Only data from channels which exceed a given threshold are transmitted. Since a high fraction of channels contain low-amplitude noise, the data rate is reduced considerably by *zero suppression*. Thresholds and pedestals are loaded into the ADC via software using the I^2C protocol and are obtained from dedicated pedestal runs in latch-all mode. For the future, mechanisms to obtain pedestals during the execution of data runs are considered.

3.3.5 The GeSiCA

GeSiCA[6] is a 9U VME control module, which manages the communication between ADCs and the data acquisition system. It sequentially multiplexes data of up to four ADCs connected via Hotlink and sends them via a 160 MB/s optical Slink connection [Bij] to the COMPASS data acquisition. Moreover, GeSiCA receives the experiment-wide clock and trigger through a TCS[7] receiver and distributes them to the ADC (see [Gru01]). For configuration, the APVs' I^2C bus can be accessed and configuration registers of GeSiCA can be set via the VME bus and a VME front-end machine running Linux.

3.4 The cryostat

As mentioned in section 3.2, two silicon detectors are mounted back to back to form a station. As a first step, two detectors are mounted on a glass fibre star-shaped structure, called *shuricane*. The shuricane is then mounted in a holding structure called *cryostat*. The structure has to have the following requisites:

[4] **F**ield-**p**rogrammable **g**ate **a**rray

[5] In a noise spectrum, the baseline differs slightly from channel to channel. The zero values of the individual channels are called *pedestals*.

[6] **GE**M and **Si**licon **c**ontrol and **a**cquisition

[7] **T**rigger and **c**ontrol **s**ystem

- light tightness: silicon detectors can detect visible photons. In a normally lightened environment, the number of these photons is much higher than the number of detected beam muons. For avoiding to detect, then, visible photons the cryostat has to be light tight.

- vacuum tightness: cryogenic operation of the detectors imply their optimal thermal insulation which respect to the outer environment. In order to minimise the amount of liquid nitrogen used for cooling. The absence of water is also an issue, to avoid any formation of ice on the wafer, which would lead to an increase of material along the beam path. Both these requirements are fulfilled while operating the detectors in vacuum.

- low mass: to minimise the multiple scattering contribution to the spatial resolution, the radiation length of the detectors and their hosting structure has to be as small as possible in the beam through direction.

- Faraday cage: a metallic holding structure can help to reduce the noise induced by the electromagnetic radiation in the experimental environment, generated by other apparata.

Fig. 3.8 is a schematic view of the dedicated cryostat. Its main part is a stainless steel frame where the shuricane is positioned with a precision of ~ 100 μm. The cryostat hosts 3 KF flanges on the bottom, where a vacuum pump, a vacuum gauge and a spill valve for vacuum compensation are installed. The top and the two sides host 6 flanges, two flanges each, used for cryogenic and electric connections.

On the frame, perpendicular to the beam directions, two plates close the cryostat. In order to minimise the material in this direction, a 10×7 cm^2 window was opened on each plate. The window is covered with a 100 μm aluminized Mylar foil lying on a net of Keflar wires to avoid the implosion of the foil during the pumping. The aluminization guarantees both light tightness and electromagnetic shield. Details on the plate structure can be found in [Fuc04].

The cryostat is operated with an inner pressure $\sim 10^{-6}$ mbar. The electrical connections between the L-board and repeater cards are done via a long, curved PCB, which is glued in the flange with two-component epoxy glue, half remaninig in the cryostat and half outside. One of the top side flanges hosts a connector for the liquid nitrogen inlet: at the bottom of the connector the LN_2 flux is split and the cooling of the two detectors is done in parallel. The two LN_2 outlet are located on the sides. In order to avoid any electrical coupling, the capillaries are solded onto the detectors to the inlet and outlets via ceramic connectors. Fig. 3.9 shows a module installed in the cryostat.

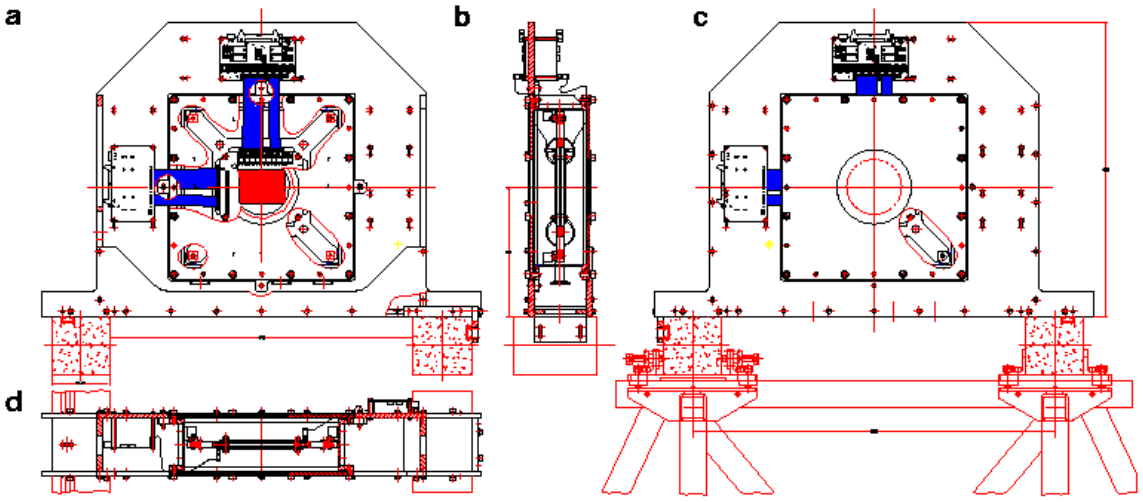

Figure 3.8: Schematic drawing of the cryostat: a)front view of open cryostat; b) side view; c) front view with window installed; d) top view.

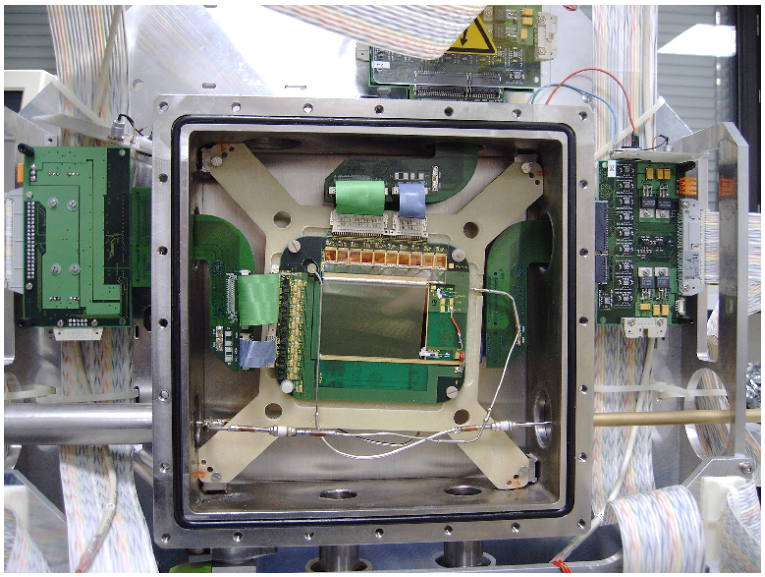

Figure 3.9: A silicon module in the cryostat

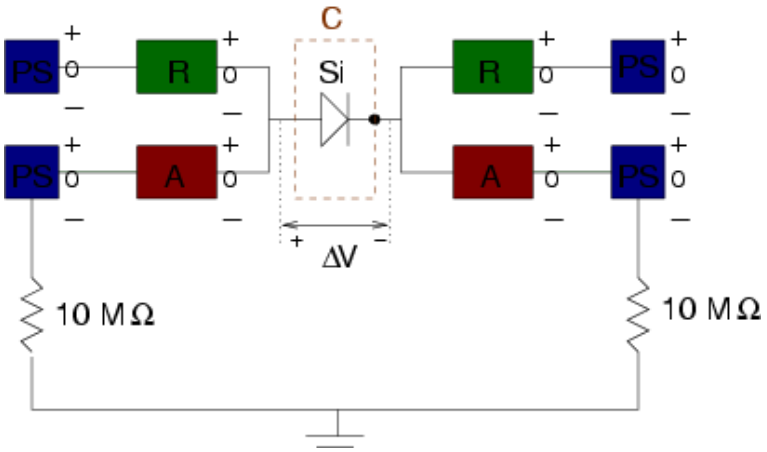

Figure 3.10: The grounding scheme for the silicon detector. **Si** is the detector, **C** is the cryostat, **R** the repeater cards, **A** the ADCs, **PS** the power supplies, Δ**V** the applied bias voltage between the two sides of the detector.

3.5 The grounding scheme

The bias voltage is applied between the *p*- and *n*-side of the silicon detector. Because of the capacitive coupling between readout strips and silicon implants (see Sec. 3.2.3), the readout electronics can be in principle on any potential. Anyhow, the L-board, the repeater card and the ADC reading out the same detector side were put at the same potential of the implant, in order to avoid problems in case of short cut of a strip capacitor. The grounding scheme is shown in Fig. 3.10. The silicon detector (**Si**) is represented as a diode and Δ**V** is the applied bias voltage. The power supplies of the repeater cards are intrinsically floating, while the ones for the ADCs are connected to the ground via a 10 MΩ resistor. Since the GeSiCA is optically connected to the ADCs, it is decoupled and it can read out ADCs which are at a different reference voltage. The *p*-side of the detector is also connected to the cryostat, in order to define a reference ground. Respect to it, the *n*-side is at high potential. Since the different components of the readout chain and their connecting cables cannot be grounded, they act like antennas and pick up electronic noise on the potential lines. To minimise the effect of this noise on the signal, a 10 nF capacitor and a 200 μF one were installed across the bias voltage to filter the high frequency noise.

Figure 3.11: View of the target region

3.6 An overall view

Fig. 3.11 is a picture of the silicon stations as installed during the 2003 run. The cryostats are mounted on an optical bench. The bench has a precision mechanical structure that permits it to be aligned with some reference direction to a precision of $\sim 100\ \mu$m.

The complete readout chain is depicted in Fig. 3.12.

A particle crossing the detector creates a signal which is collected on the readout chip. The signal is first amplified (repeater card), then transfered to the ADC

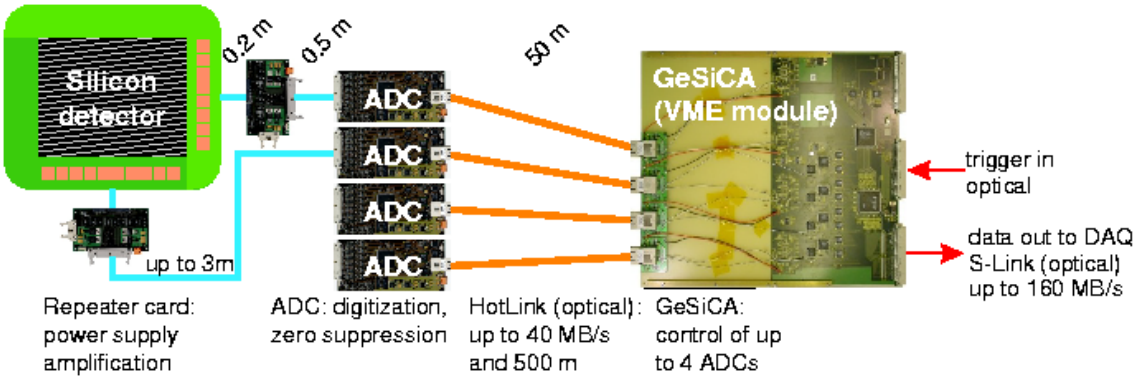

Figure 3.12: Silicon readout chain (not to scale)

where it is digitised. The ADC also performs zero suppression, reducing the amount of data which are transferred to the GeSiCA. The GeSiCA collects the data of four ADC (one complete station), merges and transfers them to the general COMPASS data acquisition system.

Chapter 4

Preparation and installation of the first cryogenic silicon station in COMPASS

As mentioned in chapter 2, the recovery of the charge collection efficiency (CCE) of damaged silicon detectors operated at cryogenic temperatures has a maximum for $\sim$ 130 K, the so called Lazarus temperature. In order to fulfil this temperature requirement, the supporting boards for the detectors were equipped with tiny capillaries (inner diameter 1.3 cm; outer diameter 1.6 cm) where a continuous two-phase flow of nitrogen was achieved, in an attempt to ensure an optimal thermal contact between them and the detector (see Chap. 3). The heat transfer proceeds from the detector to the capillary where liquid nitrogen is flushed. Since the boiling point of nitrogen is at 77 K (at atmospheric pressure), the capillaries will contain a mixture of liquid and gas (*2-phase* flux), the smaller the amount of gas the higher the cooling capability of the mixture.

A variation of nitrogen flux results in a change of the temperature of the detector.

In this chapter all the steps which brought the silicon station at cryogenic temperature into operation are listed. First the laboratory setup, then the tests of the different components, and finally the installation of the silicon station in the experimental area are described. The final section is dedicated to the description of a distribution box for liquid nitrogen that will be used during the runs in the next years.

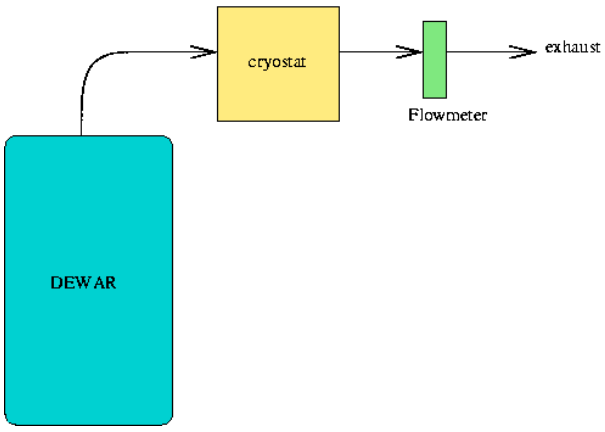

Figure 4.1: Schematic view of LN_2 flux for the laboratory setup

4.1 Laboratory setup

Within the scope of this thesis, a laboratory setup was realised from 2000 to 2002. Liquid nitrogen was supplied by a self-pressurised dewar. The dewar has a capacity of 120 l. An internal pressure building circuit permit a pre-set pressure to be maintained which can be set by the user. Nitrogen is transfered to the cryostat via a super-insulated transfer line. The transfer line has a double axial structure: the inner pipe, where liquid nitrogen is flushing, is surrounded by a second chamber. They are connected in a way such that a small amount of nitrogen is flushing back into the second chamber; the third chamber is evacuated to minimise the thermal exchange with the exterior. This peculiar arrangement was designed to minimise the loss in liquid helium transfer; in case of liquid nitrogen the transfer occurs with practically no losses. For a more detailed description of the dewar and the transfer line see [wes].

In the following measurements, manual flow meters were used to measure and control the liquid nitrogen flux downstream of the detector. The gas was guided to the flow meters with a PVC tube. In order to avoid any dis-function of the flow meters due to frost, they were placed $\sim$ 2 m away from the outlet of the cryostat, allowing for the gas to warm up before passing through the device.

In Fig. 4.1, a schematic view of the liquid nitrogen path is depicted.

4.2 Characterisation of the APV25 chip at cryogenic temperatures

In order to optimise the performances of the silicon detector readout, the chip has to be mounted at a minimum distance from the silicon microstrips. Therefore, in order to operate the silicon detector at cryogenic temperatures, it is mandatory that the readout electronics should work in the same range of temperatures. The first step was then to check the functionality of the readout chip at cryogenic temperatures.

In this section, results of tests performed on the APV25-S0 at cryogenic temperatures are presented: in particular, the features of different samples in the range of temperature between 77 K and room temperature; the chip features stability with temperature oscillations in the "Lazarus region" (130 ± 20 K) and the resistance of the chip to thermal cycles. The S0 version of the APV25 chip was used.

4.2.1 Cold measurement setup

In order to perform measurements, the APV25-S0 has been mounted on a dedicated 4-layer printed circuit board PCB as shown in Fig. 4.2.

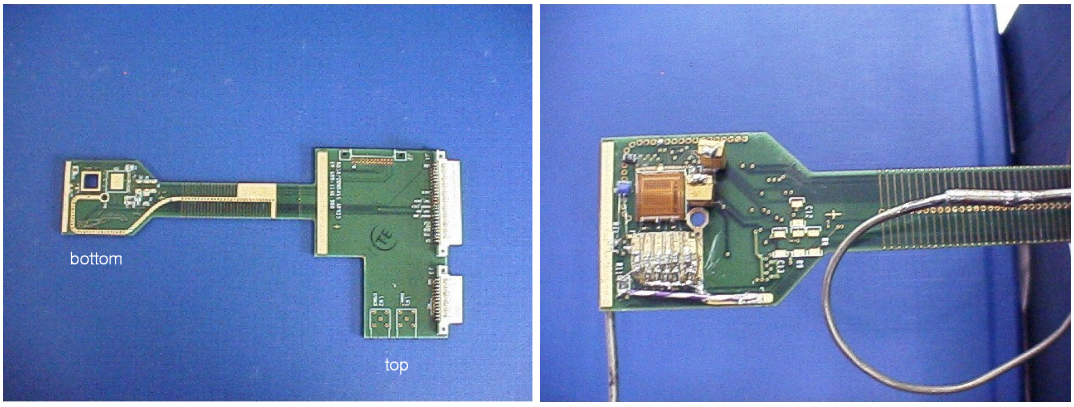

Figure 4.2: 4-layer PCB used for the cold measurements

The PCB can host, in its lower side, up to two silicon sensors, one per side, with their readout and the temperature monitoring system. The design has been made with the perspective of testing silicon tracking detectors and their electronic readout at cryogenic temperature. However, in the following measurements, only one side of the board was used to characterise the APV25-S0 chip. The board is partially inserted into a dedicated cryostat that works in vacuum conditions. The design of the PCB has been optimised in order to achieve two main requisites:

- homogeneous cooling in the region of the detector and electronic readout
- thermal decoupling between the bottom in the cryostat's vacuum and the top at atmosphere pressure.

In particular, the second requisite is needed to avoid that at the top of the PCB, where all the electrical connections are placed, water condenses. Further information on the cryogenic characteristic of such a design can be found in [gra01] or in [RD39w].

In order to cool down the PCB, a nickel-copper micro-pipe (inner diameter 1.3 mm, external diameter 1.6 mm) was used, tin soldered on the dedicated pad in which a flux of liquid nitrogen was directed. The temperature can be tuned thus controlling the flux rate of liquid nitrogen. The chip has been glued with 2-components conductive glue, to ensure the electrical connection to the bias pad on the bottom. To simulate a **M**inimum **I**onising **P**article (*MIP*) injection on one chip channel, a RC network connected to an external tunable power supply was used. This arrangement permits simulation from 0.5 up to several MIPs, in steps of 0.5. Moreover, five other channels of the APV25-S0 were connected to the ground via a series of different capacitances and 50 Ω resistors to measure the noise as function of capacity at different temperatures.

To measure the chip properties as a function of temperature, a vacuum tight cryostat has been used. The dedicated measurement setup is shown in Fig. 4.3. From the figure it is possible to distinguish two sets of flanges: four (on the top of the figure) to host instrumentation and five (on the bottom) to host PCBs. The PCB used for these measurements is plugged into the second flange from left. A PVC transparent tube emerges from the PCB, this is the liquid nitrogen outlet connected to a flow meter that measures and tunes the flux rate. On the other flanges from the left there is a ventilation gauge, a pressure gauge, a liquid nitrogen inlet line and the vacuum turbo pump gauge. The working pressure inside the cryostat has been measured as 1×10^{-6} mbar. The maximum liquid nitrogen flux allowed by the flow meter was 250 N_2 gas/hour. The temperature was monitored via Platinum thermometers *PT100* connected to a Keithley multimeter. The whole system allows temperature control within 1 K.

4.2.2 APV25-S0 characterisation

Fig. 4.4 shows the output of the APV25 where a 1-MIP equivalent signal is injected into one input channel. A full characterisation of the chip can be found in [Ray01]. The amplitude of the connected channel is correlated with the number

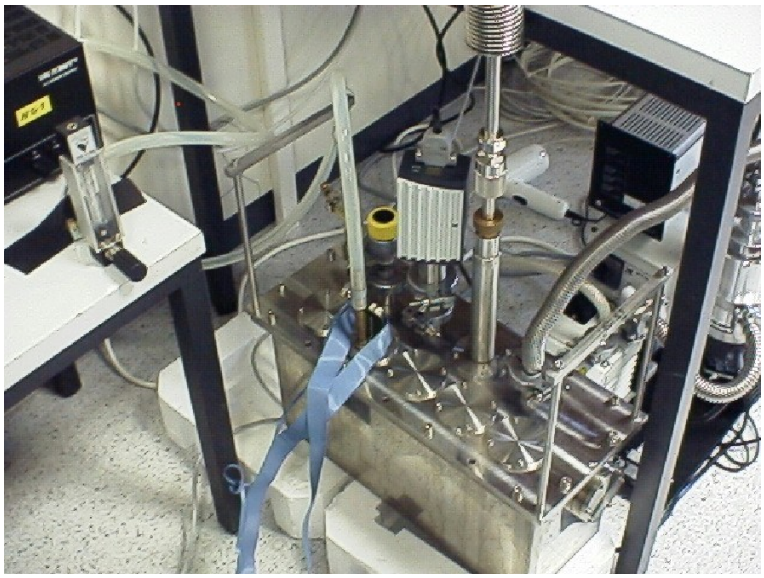

Figure 4.3: Experimental set-up: a) beam-through flange, b) inlet for liquid nitrogen, c) nitrogen outlet, d)flange to host the chip board.

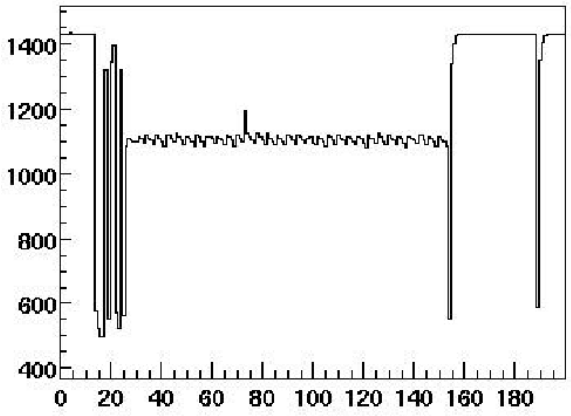

Figure 4.4: APV25-S0 output data frame at 130 K

of injected electrons. Measurements were performed to determine the analogue pulse shape and linearity, noise as function of input capacitance, temperature behaviour and uniformity of pipeline. It is worth pointing out that all measurements at low temperature have been performed without changing the parameters' setting of the APV25-S0 with the respect to room temperature, in order to verify the effects of the temperature on the CMOS circuit.

Analogue pulse shape and linearity

Fig. 4.5 shows the amplifier pulse shape measured at room temperature and 130 K, in peak (broad curve) and deconvolution (narrow curve) modes (Sec. 3.3.1). Applying a progressive delay ΔT between the time of the charge injection and of the readout (depicted on the x-axis) the shape of the APV25 output signal was reconstructed.

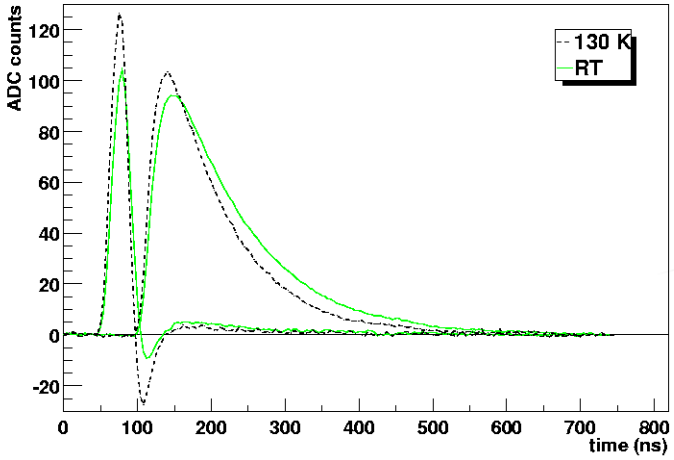

Figure 4.5: APV25-S0 pulse shape dependence on signal amplitude in *peak* and *deconvolution* mode at 130 K (dashed black curves) and at room temperature (continous green curves) for 1 **M**inimum **I**onising **P**article (*MIP*) equivalent signal

The curves at 130 K show a smaller rise and falling time, while the position of the peak is basically the same. Moreover, in case of deconvolution mode, one can note an undershooting. Finally a slightly higher peak value is present in both working modes when the chip is operated at 130 K. In fact at low temperature, the behaviour of a CMOS circuit is expected to decrease its characteristic time τ, which in other words means that the circuit becomes faster. This consistently explains all the three main features at low temperature. A basic evaluation shows that the rising time t at 130 K is about 15% smaller than at room temperature.

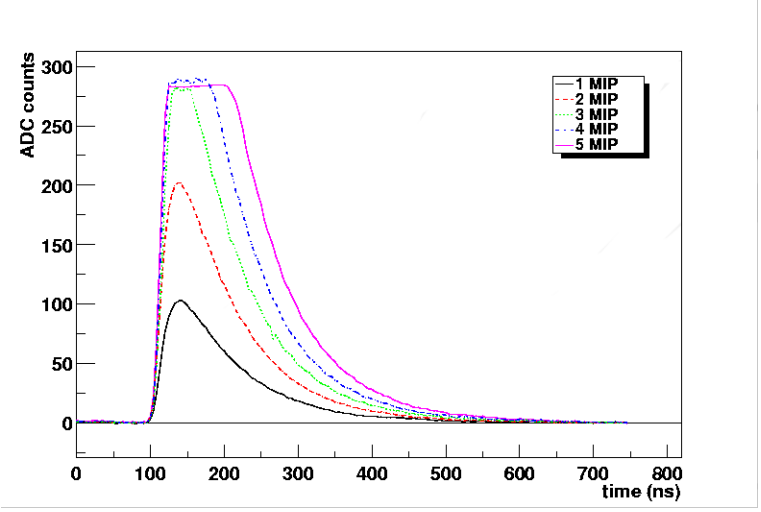

Figure 4.6: APV25-S0 pulse shape dependence on signal amplitude in *peak* mode at 130 K for different MIP signals

Fig. 4.6 illustrates the pulse shape dependence with the signal amplitude in peak mode at 130 K. The input signal varies between 1 and 5 MIPs in 1 MIP steps. The saturation of the maximum of the pulse shape begins at higher values of MIP than at room temperature. This is due to the fact that when lowering the temperature the position of the APV25-S0's baseline shifts to lower values with respect to the dynamic range of the chip.

Noise

Fig. 4.7 shows the APV25-S0 noise dependence as function of the input capacitance at room temperature and at 130 K. It is clearly seen that at low temperature, the noise becomes higher. This behaviour can be explained starting from the measurements described in the previous section. At low temperature the characteristic time τ of the chip decreases; since the noise of the chip's amplifier goes as $1/\tau$ [NBW], an increase of the noise is expected at low temperatures. However, the observed variation is small and does not inhibit the functionality of the chip.

Temperature behaviour.

In order to check the behaviour of the chip's characteristic versus temperature variation around the Lazarus temperature, the noise and the pulse shape at different MIP signals in the range 110-150 K in 10 K step were measured. Fig. 4.8

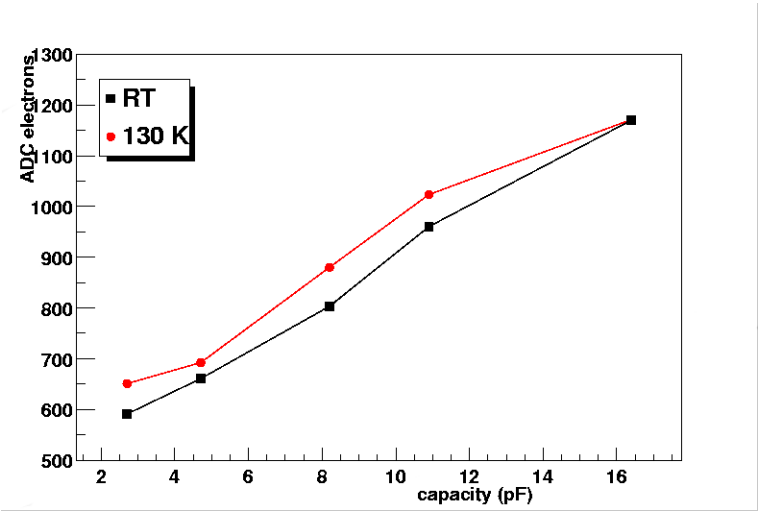

Figure 4.7: APV25-S0 noise dependence on input capacitance at room temperature and 130 K.

shows pulse shapes for 1 MIP signal at different temperatures. As shown in the plot, no significant changes in amplitude and time are observed.

In Fig. 4.9 the dependence of the maximum amplitude of 1 MIP signal from the temperature is shown. If one estimates the noise of thermal oscillations as the variation of ADC counts per K at the maximum amplitude, one finds 0.125 ADC channels/K.

In Tab. 4.1, the values of typical sources of noise are listed. The noise due to temperature variations is negligible compared with other sources of noise. This result is very promising in view of a usage of the APV25-S0 at cryogenic temperature.

Source	Noise (ADC channels)
Intrinsic ADC noise	0.5
Not bonded channel	~ 1
Bonded channel	~ 3.5
From temperature variation	$\sim 0.125/K$

Table 4.1: Different sources of noise in ADC channel units.

In Fig. 4.10 the gain corresponding at different temperatures is shown. The saturation for input signals bigger than 3 MIPs is due to the limitation imposed by the dynamical range.

The noise as function of the input capacitance at different temperatures is shown in Fig. 4.11. As expected, the noise increases when temperature decreases.

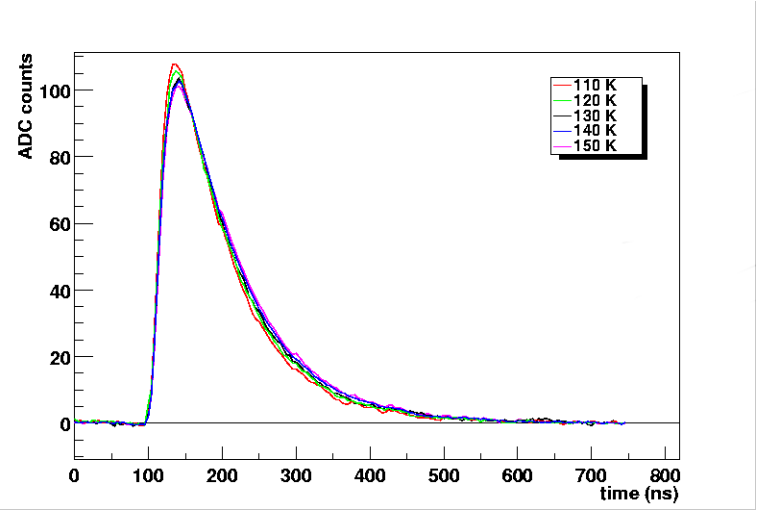

Figure 4.8: APV25-S0 pulse shape in peak mode for 1MIP equivalent input signal at different temperatures.

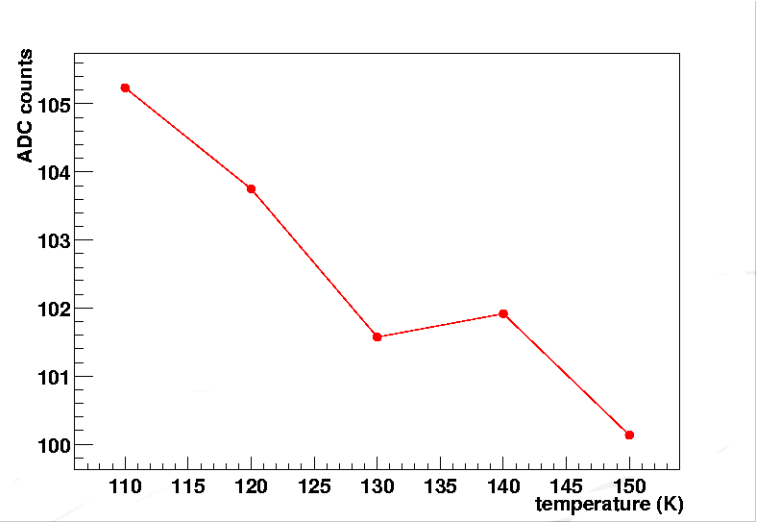

Figure 4.9: Dependence of signal amplitude from the temperature.

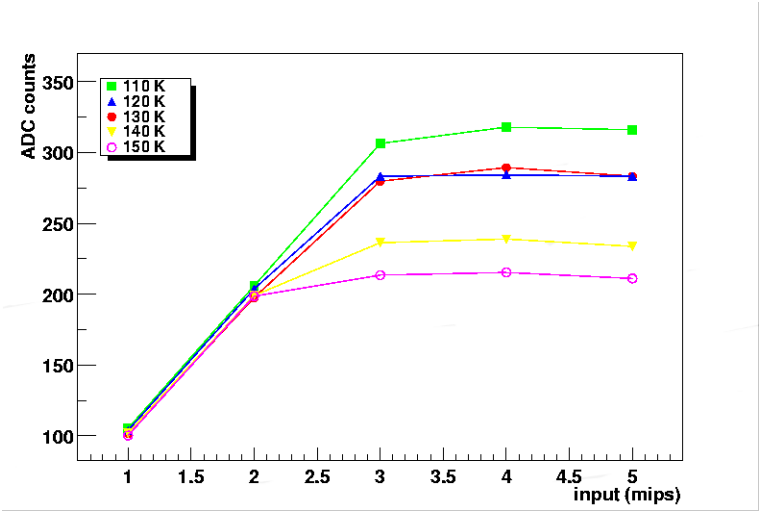

Figure 4.10: APV25-S0 gain at different temperatures

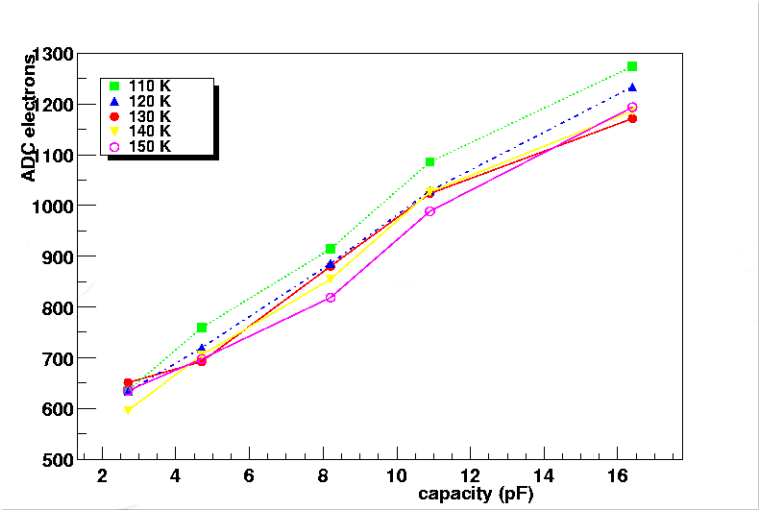

Figure 4.11: Noise vs. capacitance at different temperatures.

Pipeline tests

The APV25 pipeline cell capacitance has to be uniform to avoid variation for corresponding pedestal values. The uniformity of pipeline at 130 K was tested to verify that no peculiarities occur at cryogenic temperatures. Fig. 4.12 shows the value of pedestals versus pipeline location, while Fig. 4.13 shows the same results after converting the rms value to Equivalent Noise Charge. The figure clearly demonstrates that even at low temperature the noise associated to pipeline distribution is negligible.

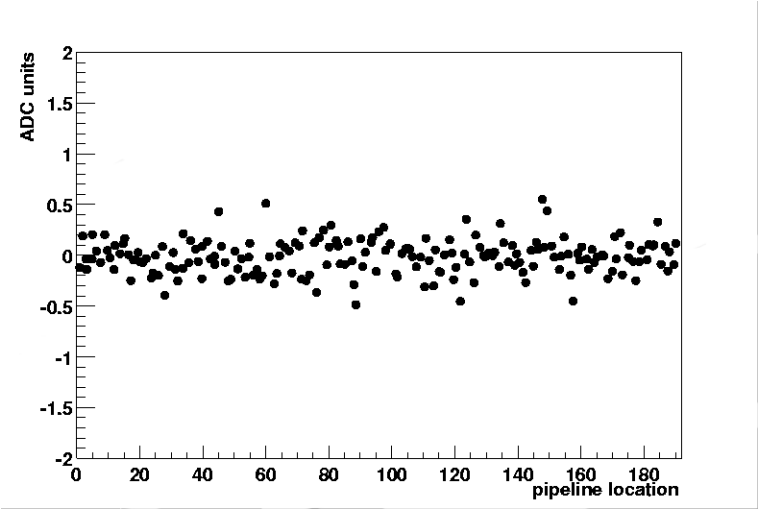

Figure 4.12: APV25-S0 pipeline pedestal for a typical channel at 130 K.

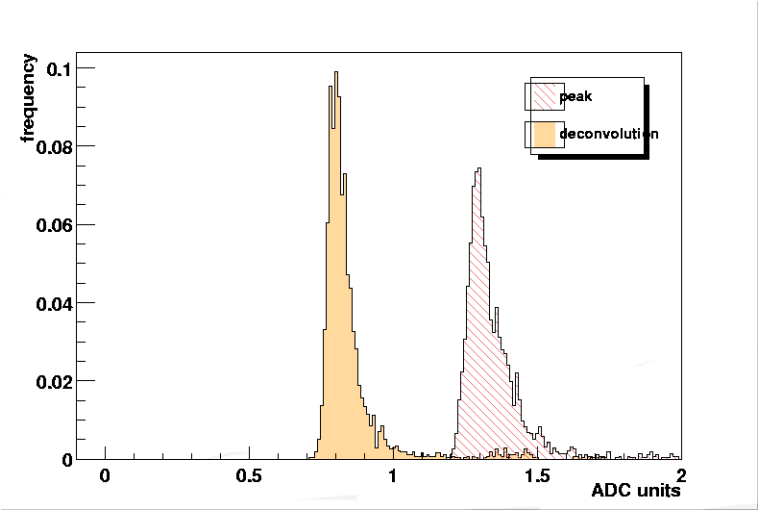

Figure 4.13: r.m.s. pipeline pedestals for all 128 channels.

The amplitude on the 192 capacitance pipeline for a 1MIP signal at 130 K as shown in Fig. 4.14. The width of the distribution is as small as was measured for room temperature, indicating a close matching of capacitance between cells [5].

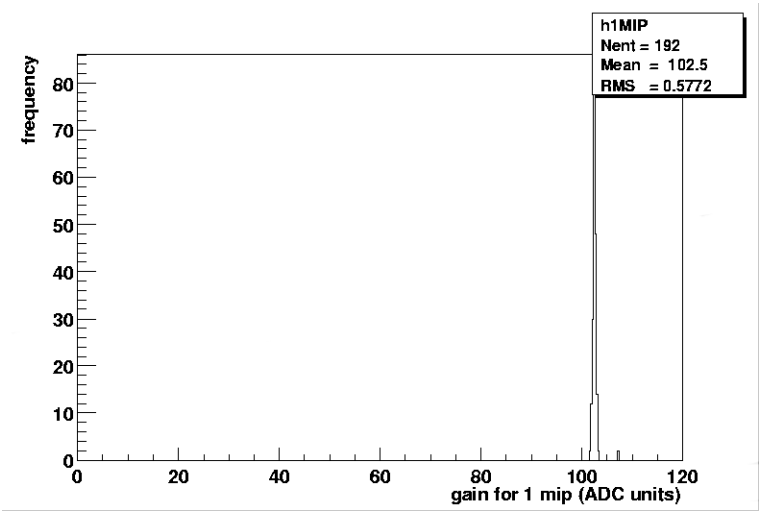

Figure 4.14: Pipeline gain uniformity at 130 K.

Tolerance at thermal cycles

In order to use the APV25-S0 in a real environment, it is mandatory to make sure that the behaviour of the chip stays stable even after several thermal cycles. In the course of the test previously described, some chips underwent approximately 50 thermal cycles. Additionally, systematic tests on one sample chip were performed. The minimum temperature attained by the chip has been of the order of 100 K; after performing the measurements of the chip characteristics, such as output data frame, pulse shape, noise, the chip has been quickly warmed up to room temperature. The measurements were then repeated 50 times. The results in Fig. 4.15 and Fig. 4.16 clearly show that no appreciable change occurred before and after the thermal cycles.

4.3 Test of the components

As for the readout chip, the usability of the assembling components at cryogenic temperatures was checked.

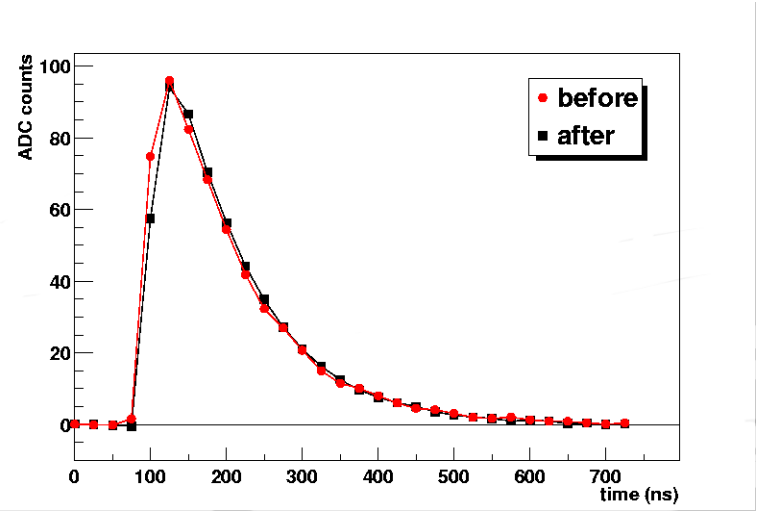

Figure 4.15: APV25-S0 pulse shape before and after thermal cycles.

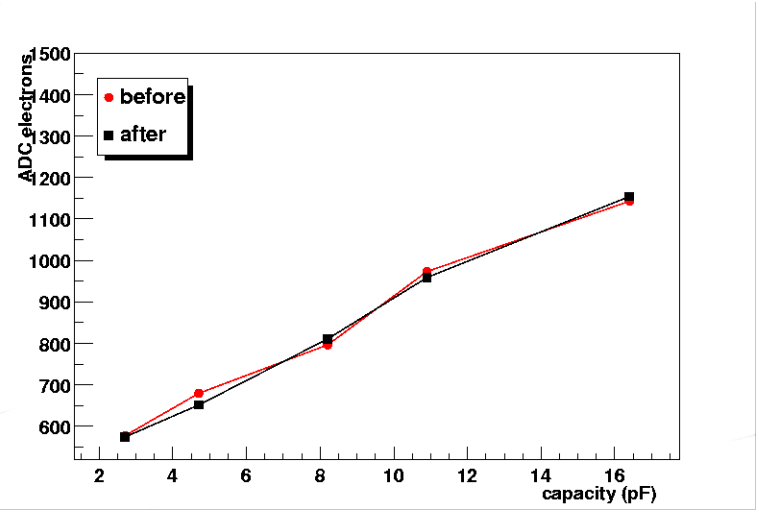

Figure 4.16: APV25-S0 noise before and after thermal cycles.

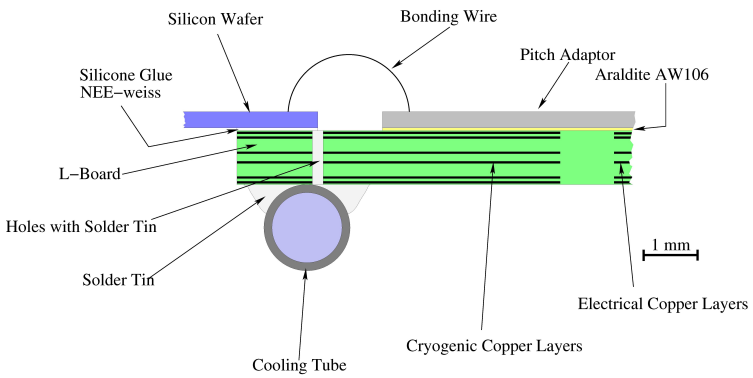

Figure 4.17: The Arrangement of the wafer on the L-board

4.3.1 Test of the glue

In Fig. 4.17, a cross section of the detector is depicted. The cooling proceeds through the sides of the wafer which are glued to the L-board with a silicon based glue. The glue had to be electrically non-conductive and at the same time possess a certain elasticity in order to absorb the mechanical stresses created on the whole detector by temperature variations. The most eligible glue, NEE001 weiss, used already for the HERA-B silicon detectors [Abt98], was tested at cryogenic temperatures, to check whether its characteristics where maintained in these working conditions. A 5×7 cm^2 piece of glass of 300 μm thickness was sandwiched between two L-boards, reproducing the assembly used for the COMPASS detectors. The glass was glued on two sides only with small spots of glue and on the two remaining sides with a continuous line. The sample was squeezed in liquid nitrogen for 3 hours. The sides with the spots of glue were unglued in some points, while the two remaining sides were still stuck with continuous lines of glue. The glass was then glued with a continuous line on all the four sides of the board. The sample was then squeezed in liquid nitrogen for 10 minutes, then extracted and kept at room temperature for 5 minutes. The cycle was repeated for five times after which no changes appeared in the setup.

The chips were glued with a bi-component epoxy-based conductive glue. This glue was also tested for liquid nitrogen temperature; it never showed any degradation after many thermal cycles.

4.3.2 Test of the connector

In Chapter 3 the layout of the L-boards was described, it was particularly highlighted that the two L-boards between which the wafer is glued have two different ground potentials. It was then preferable to use two different capillaries for the two sides of the detector, in order to have a complete electrical decoupling of the two L-boards. To avoid any mechanical complication, a unique flux cooling of one detector was used as well as an insulator connector between the capillaries on the two sides of the detector. The connector was designed with a 180° angle to be fitted in the dedicated hole in the L-boards (see Fig. 3.7).

Concerning the material, the first choice was to use Stesalit, a fibre glass material. On both sides of a small tube of Stesalit ($\sim$ 1.5 cm length, $\sim$ 1 cm external diameter, 1.7 mm inner diameter) two capillaries were fitted and glued with a two component epoxy glue. The piece was then inserted into the same cryostat used for the measurements described in section 4.2. The cryostat was evacuated at $\sim 10^{-6}$ mbar and liquid nitrogen flushed in the capillaries. With the vacuum gauge mounted on the cryostat it was possible to check eventual leaks due to cracks of the Stesalit or, more probably, of the glue. The piece could stand a flux of $\sim$ 600 l/h of gas, that is $\sim$ 1 l/h of liquid in the tube, but, after few thermal cycles, the vacuum inside the cryostat was lost.

The use of the Stesalit tube requires three different materials to be connected to the same point: the Stesalit itself, the copper-nickel capillary and the epoxy based glue. Since these materials have different expansion coefficients, the thermal stress at this point was high. The idea of modelling a connector with epoxy glue and gluing the capillaries to it with the same glue was successful. This connector has approximately the same dimension of the Stesalit one. The epoxy connector underwent the same tests of the Stesalit, showing its reliability after many thermal cycles and an easier handling respect to the Stesalit one.

In Fig. 4.18 the epoxy connector is shown.

4.4 Temperature distribution

As already mentioned, in order to exploit the Lazarus effect, the silicon detectors have to be operated at cryogenic temperatures, preferably 130 K, since for this value of temperature the recovery of the CCE is maximum. The silicon detectors used in COMPASS have an active area of $5 \times 7 \text{cm}^2$, and the challenge was to ensure uniform temperature on the wafer. A first set of measurements was performed in order to have a distribution of the temperature on the L-board, while

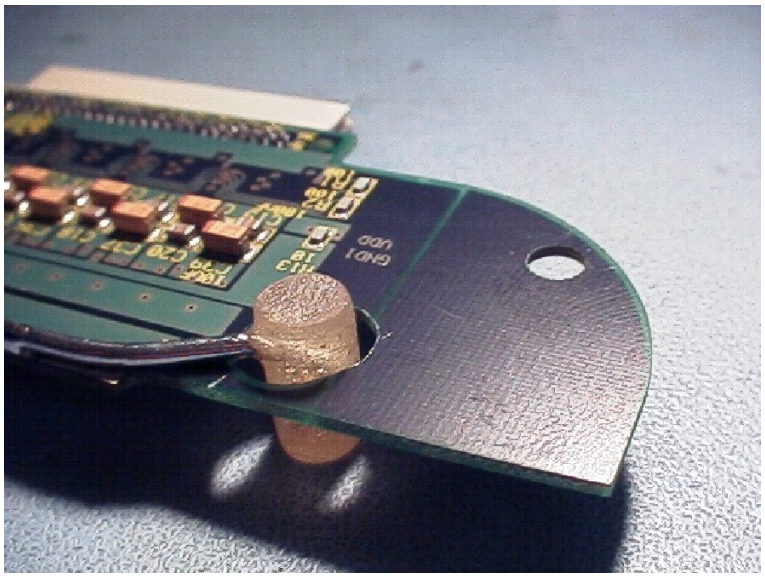

Figure 4.18: The epoxy connector

the temperature distribution on the silicon wafer is the results of simulations.

4.4.1 Temperature distribution on the L-board: measurements

The readout chips dissipate a non-negligible amount of power ($\sim$ 5 W) and constitute the main source of heat on the board. This is the reason why the cooling capillaries have to pass underneath the wafer on the side where the chips are present, in order to stop the heat flow to the detector. In order to measure the temperature distribution on the L-board, a PCB prototype was build. The distribution of the copper layers in its inner reproduces the distribution of the L-boards, but, instead of using two L-shaped PCBs, a single piece was designed. Instead of the chips, 1 kΩ SMD [1] resistors were used. Five resistors were placed at each chip position, to simulate the fact that the power is dissipated over the whole surface of the chip. The resistors were connected to an external tunable power supply, so that a variation of the voltage applied corresponded to a variation of the power dissipated. Copper-Nickel capillaries were tin-soldered on dedicated pads located on the four sides of the wafer position. All around the wafer position and across the chips, 23 Pt100 thermometers were placed. The thermometers were read out via a NI4351 National Instrument readout card, with a Labview graphical interface. A piece of glass 300 μm thick was glued on the wafer position, in order to have the same thermal load as the real detector. The goal was to

[1] **S**urface **M**ountable **D**evice

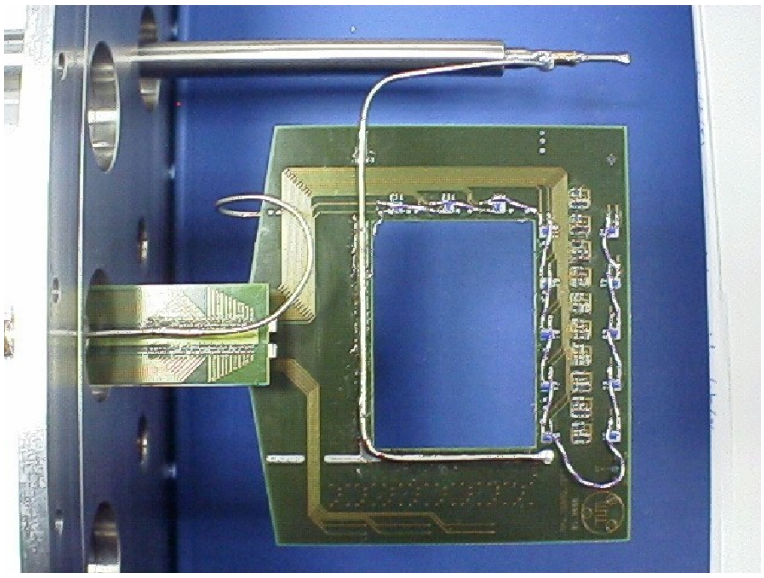

Figure 4.19: The PCB designed for thermal distribution tests

measure the temperature distribution along the wafer position. In Fig. 4.19 the dedicated board is depicted.

The board was then inserted into the cryostat described in section 4.2 and the cryostat was evacuated. The working pressure inside the cryostat was $\sim 10^{-6}$ mbar. By varying the voltage applied to the resistors and the nitrogen flux in the capillaries, a complete scan of temperature versus power dissipated and flux could be achieved.

In Fig. 4.20 the temperature behaviour registered by one thermometer as a function of the power dissipated for different liquid nitrogen fluxes is shown. The curve for 250 l/h shows that is possible to achieve a constant temperature of $\sim$ 130 K even if the power dissipated varies.

In Fig. 4.21, the temperature distribution on the two sides of the wafer position for 4W power and different LN_2 fluxes is shown. One could see that for a flux $\geq$ 150 l/h, an uniform temperature on both sides of the wafer could be achieved. Referring to Fig. 4.20, one can then assert that with a liquid nitrogen flux of $\sim$ 0.4 l/h ($\sim$ 250 l/h of gas measured) it is possible to achieve a uniform temperature of $\sim$ 130 K on both sides of the wafer position. The temperature stays approximately constant even for a variation of the power dissipated of $\pm$3 W around 5 W.

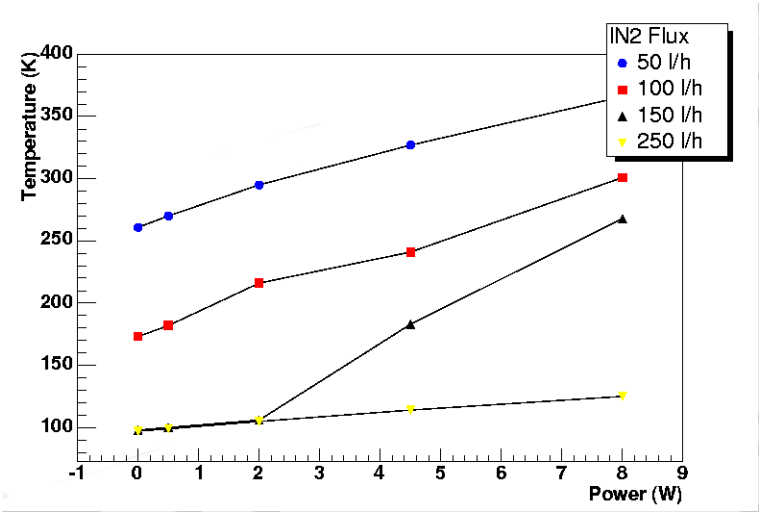

Figure 4.20: The temperature behaviour registered by one thermometer as function of the power dissipated for different LN_2 fluxes

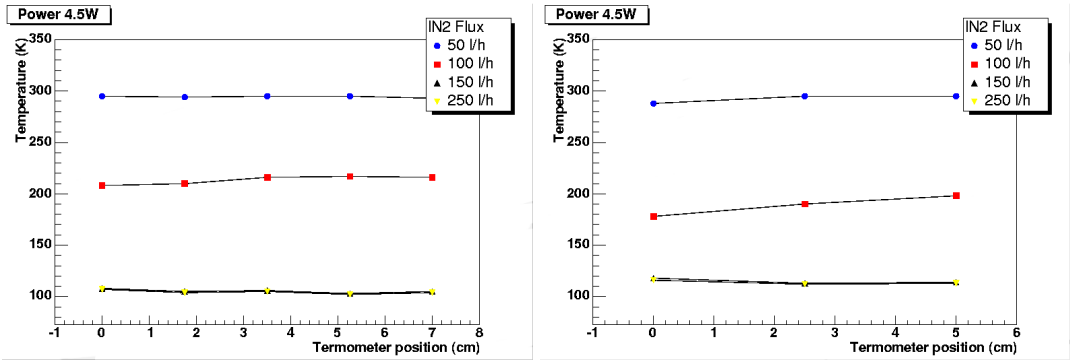

Figure 4.21: Temperature distribution on the two sides of the wafer position for 4W power and different LN_2 fluxes

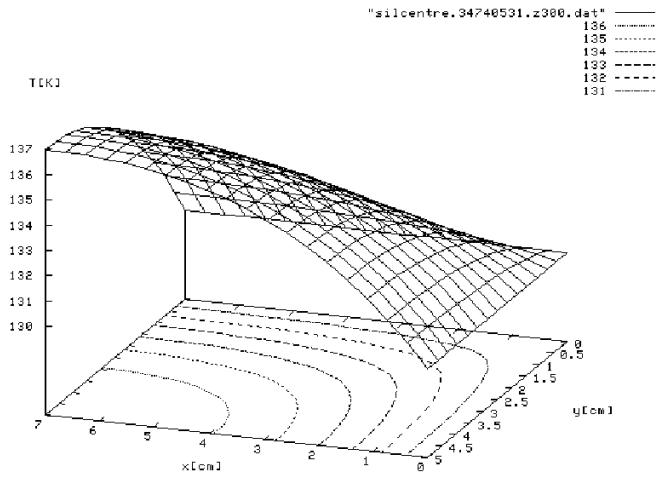

Figure 4.22: Temperature distribution on the silicon wafer (from simulation)

4.4.2 Temperature distribution on the wafer: simulation

Once the possibility to achieve an uniform temperature of $\sim$ 130 K on both sides of the wafer on the L-board was investigated, the next aim was to check the uniformity of the temperature on the wafer. This was performed done via simulations. The thermal conductivity of silicon crystals at 300 K (room temperature) is 156 W/Km (for iron 80 W/Km, for air 0.024 W/Km). With decreasing temperature, the thermal conductivity of silicon reaches values between 950 and 420 W/Km in the temperature range 100-150 K (see [GLA64]), implying that if one cools the system down to 130 K on both sides of the wafer, an uniform temperature of 130 K will be achieved over the entire surface.

To test this hypothesis, a C++ simulation package was developed, to calculate the temperature distribution of a silicon wafer with fixed temperature along two sides. The wafer was simulated as a black body, such that the power dissipated via irradiation follows the Stephan-Boltzmann law and it can be written as $R = \sigma \Delta T^4$ were σ is the Stephan-Boltzmann constant and ΔT is the temperature gradient between the wafer and the cryostat (the latter being at room temperature). This is the only power dissipated in the setup. The thermal conductivity as function of the temperature was also taken in account and in this way the time evolution of the temperature on the wafer could also be evaluated. In Fig. 4.22 the temperature distribution on the silicon wafer at thermal equilibrium is shown.

The plots shown in Fig. 4.22 were obtained supposing that the wafer irradiates from both surfaces while once the detector is installed in the cryostat, one surface

will see another wafer which is at the same temperature of 130 K and thus the power irradiated is reduced of a factor two. Moreover, the approximation that the silicon wafer is a black body overestimates the power dissipated. One can then state that the values obtained via simulations are upper limits on the temperature gradient on the wafer. Nevertheless, the value obtained of 7 K on the silicon surface was considered acceptable.

4.5 A cold station in COMPASS experiment

After ensuring the reliability of the individual components for cryogenic operation, the complete detector was assembled. The detector was installed in the cryostat and operated at cryogenic temperature. The measurement were performed in the Munich laboratory using measurement setup described in section 4.1. The main functionalities of the detector were tested using a Strontium source and a dedicated trigger setup, .

Once the detector was evaluated to be correctly functioning, a complete station equipped with cryogenic facilities was assembled and installed in the COMPASS experiment. In this section, the installation process will be described, followed by the characterisation of the silicon detectors.

4.5.1 Installation in the experiment

In order to ensure a stable cooling, a dedicated system for controlling and tuning was developed in Munich. Due to external constraints, the system could not be installed during the 2003 beam time and so the laboratory setup was used. A description of the system will be given in the next section. Electronic mass flow meters were used instead in the experiment of the manual ones. The flow meters were controlled and read out via a Labview program running on a PC. This allowed the flux to be controlled and monitored with a high precision and without access the experimental area. The nitrogen dewar was connected to the main nitrogen valve in the experimental area; unfortunately, it was not possible to refill it automatically, but this procedure was performed manually twice a week. The cryostat was evacuated till a pressure of $\sim 10^{-5}$ mbar. To avoid water condensation on the beam through windows, forced ventilation on the outer of the cryostat was organised.

The complete setup is shown in Fig. 4.23.

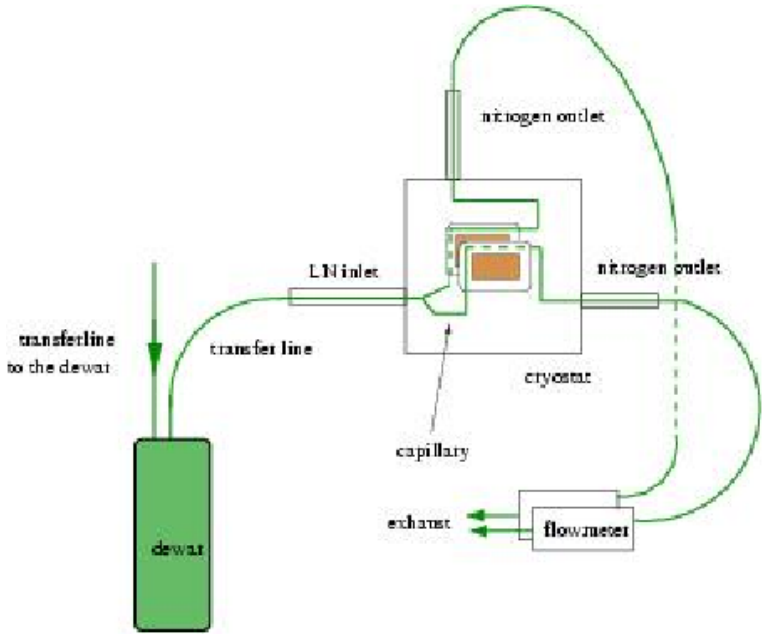

Figure 4.23: The cold setup in the experimental hall

4.5.2 The 2003 data taking

Exploiting a temporary failure of the SPS, the laboratory set-up was installed and tested in the area at the end of July. Unfortunately, this set-up did not guarantee a long term reliability. First the capacity of the dewar only provided sufficient liquid nitrogen for approximately three days, after that it had to be manually refilled and this operation required access to the experimental area. Additionally, it was observed that the capillary tubes were regularly obstructed with ice, preventing any further cooling. The ice most likely originated from microscopic water crystals intermingled with the liquid nitrogen. This blockage caused a slow decrease in the supply through the capillaries and a consequent increase in the temperature of the detector after approximately one day of stable conditions. Fig. 4.24 shows this behaviour. The rising slope in the second picture is explained by the formation of ice in the capillaries.

In order to avoid loss of beam time during the data taking, it was decided to operate the detector at room temperature until September, when a beam with a peculiar 25 ns structure (not useful for physics data taking) would be delivered by the SPS, allowing a complete test of the detector features at cryogenic temperatures within the COMPASS environment.

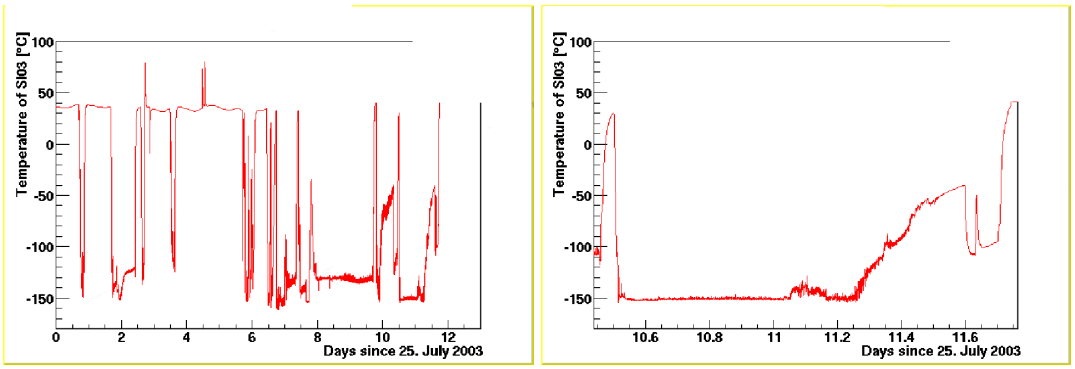

Figure 4.24: Temperature behaviour during 2003 beam time

4.5.3 Detector performances

The data taken during the 25 ns beam time were analysed in order to compare the detector performances at room and at cryogenic temperatures. As explained in Sec. 2.1.2, the size of the charge cloud is directly related to the spacial resolution. No change was found in these two parameters while the detector was operated at 130 K. A significant improvement was found instead in the time resolution: from a typical value of $\approx$ 2.3 ns at room temperature to $\approx$ 1.2 ns, an improvement by almost a factor two. The variation is most likely due to the change of the readout chip preamplifier parameters. The observations are consistent with the measurements described in Sec. 4.2. A complete description of the analysis performed can be found in [Fuc04].

4.6 The cooling control system

Operating more silicon stations at cryogenic temperature with a stand-alone cooling system, in an experimental environment where the access to the apparatus is not always possible and special safety conditions are required, presented several problems for which finding a solution has been a challenging task. A complete system was developed which allows independent cooling of several stations, with a self regulating temperature system. It consists of the mechanical infrastructures to handle liquid nitrogen and the temperature control electronics (hardware+software). As mentioned, this setup was not used during the 2003 run, but it will be installed in autumn 2004. In this section an extensive description of the components is given.

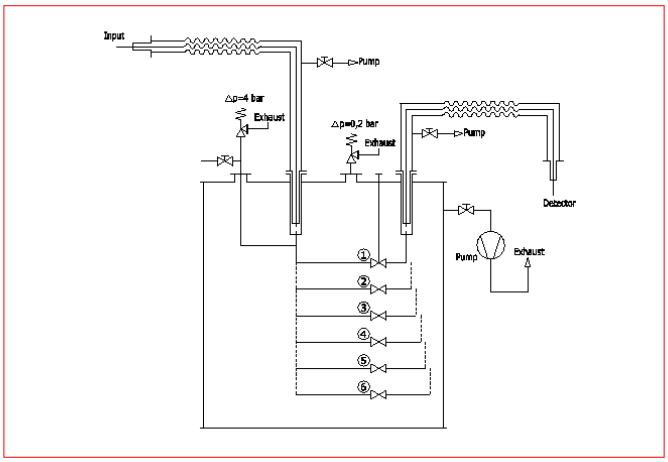

Figure 4.25: The flow scheme (the objects are not on scale)

4.6.1 The mechanical design

The design for a liquid nitrogen transfer line and distribution box to the silicon detector in the COMPASS experiment is described in this section. It is a fixed installation aimed to transfer liquid nitrogen between the main gauge, located on a side of the experimental area, and the silicon detectors. The main gauge is delivering LN_2 at 3.2 bar. The remotely controlled cryo valve installed on the gauge is connected via a bayonet to a 30 m long vacuum insulated flexible transfer line to the distribution box. The nitrogen flux is there divided in order to provide separate cooling to the different silicon stations. Liquid nitrogen is supplied to the detectors is done via 2 m vacuum insulated transfer lines with bayonet connections on each end. Each line has an estimated flux of 2 l/hour of LN_2. The nitrogen flows through the capillaries and cools down the detector as described in Sec. 3.3. The nitrogen exhaust is collected and evacuated outside of the experimental hall. The nitrogen flow from the main gauge to the detector is depicted in Fig. 4.25.

It is worthwhile to mention that a water filter will be installed at the main gauge, in order to avoid the formation of ice inside the capillaries that compromised the correct operation of cryogenic silicon detectors during 2003 beam time (see Sec. 4.5.2).

All the dimensions of the components have been optimised according to the German security code for under pressure devices AD-Merkblätter. In the following a more detailed view of the individual components is given.

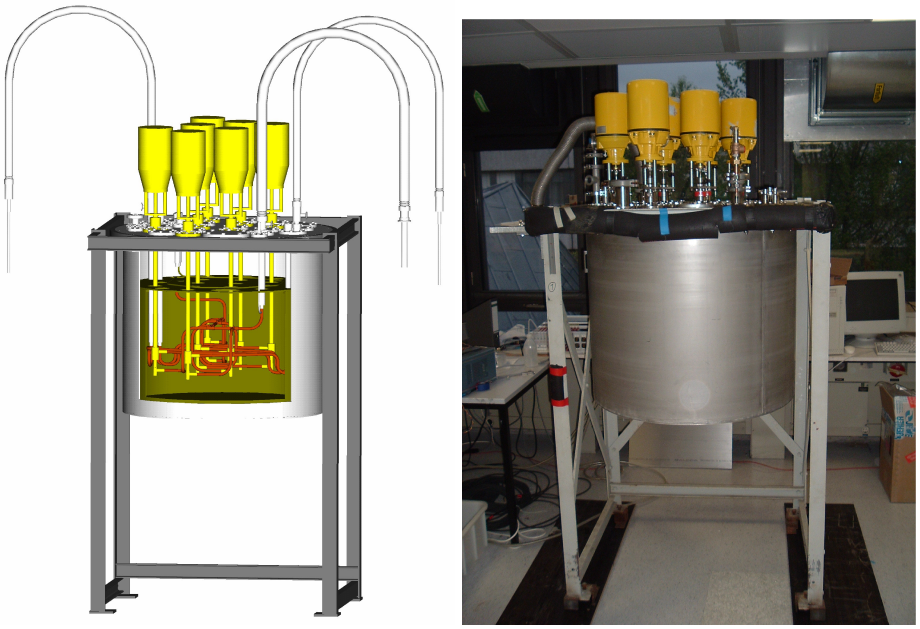

Figure 4.26: The distribution box

The distribution box

The distribution box is a vacuum cryostat which divides the main supply of liquid nitrogen and redirects it to the individual silicon stations. Its main components are the vessel, the shield and the distribution system. Fig. 4.26 shows a sketch of the distribution box.

- The *vessel* is a stainless steel cylinder closed at the bottom end, with a diameter of 2 m, 1.5 m height and 5 mm thick walls. It host the distribution system and it is closed on the top with a flange where all service connections are mounted. A service flange for pumping is installed on the side of the vessel. The vessel is evacuated down to $P \approx 10^{-2}$ mbar, to ensure a good thermal decoupling between the distribution system and the outer environment. The vessel is additionally equipped with an valve that opens in of an internal pressure 0.2 bar higher than atmospheric. This system is meant to prevent pressure building up inside the vessel in the case of nitrogen leak from the distribution system.

- A *copper shield* is installed between the vessel and the distribution system to improve the thermal decoupling of the latter. The shield is cooled to ≈ 100 K via a dedicated cooling line. The amount of energy transferred via radiation between two bodies with temperatures T_1 and T_2 is $\propto T_1^4 - T_2^4$. Without the shield, the energy transferred to the nitrogen in the distribution

system would be $\propto 300^4$ K $- 77^4$ K. The presence of the shield reduces this quantity to $\propto 100^4$ K $- 77^4$ K. In this way a lower gas/liquid ratio in the tubes can be achieved, increasing the cooling properties of the mixture.

- Fig. 4.26 shows the *distribution system*. The nitrogen comes from the main gauge through the transfer line, that is connected with a bayonet to the distribution box. The main tube is then divided in seven tubes with smaller diameters. Each of these tubes is connected to a cryogenic valve, in order to open and close the supply of LN_2 for each silicon station individually. One of the tubes is soldered along the walls of the copper shielding, while the other six are directed to the top flange where they are connected via bayonet to the transfer lines of the stations. To minimise the thermal loss due to radiation, the tubes are wrapped in several layers of super insulating materials: a Mylar foil coated with aluminium. The main tube is equipped with an overpressure valve ($P = 4$ bar), to avoid pressure increases that would be over the security values. The system was built in the Munich workshop, readapting an existing structure used in the *Tritron* experiment. The functionality of the system has been successfully tested in the laboratory.

The transfer lines

As already mentioned, the nitrogen supply is provided via a main gauge installed in the experimental hall. The distribution box is located ~ 30 m from the gauge, close to the silicon detector platform. The transfer of liquid nitrogen is done via a transfer line. The transfer line is flexible, since it must follow a complicated path from the gauge to the distribution box. The line is composed of two concentric flexible stainless steel tubes, between which is a vacuum. The nitrogen flows through the inner tube and the vacuum ensures good thermal insulation. Custom-made Teflon spacers are inserted every 20 cm throughout the whole tube length to avoid any contact between the two tubes which would reduce the thermal insulation. The inner tube is wrapped in several layers of super insulating materials. The transfer line was manufactured at the CERN cryolab. Other transfer lines are used from the distribution box to the detector. The main line structure is repeated on smaller scale.

The gas formation fraction in the transfer lines was estimated to be small for the required cooling flux of $\approx$ 2l/h each station. In this way the cooling of the detectors was optimised.

Electrical insulation

As mentioned in Sec. 3.3.2, the readout chips are very sensitive to the noise from power and grounding lines. In order to avoid the pick up noise from the cooling system (transfer lines and distribution box), it has to be electrically decoupled from the cryostat. For this purpose, a connecting structure of Teflon was designed, that was installed on the bayonet which connects the transfer line with the cryostat. Teflon is used since it is an excellent insulator and additionally highly suitable for cryogenic temperatures environment.

4.6.2 The control of the flux

The temperature of the silicon wafer depends upon the amount of nitrogen that flows in the capillaries. Therefore, a fast and reliable regulation of the nitrogen flux is of capital importance to achieve a stable temperature. For this reason, the developed temperature control is based on the control of the gaseous nitrogen flux at the outlet of the cryostats. This choice allows independent tuning of the two detectors in one station, minimising the number of inlets in the cryostat. In the following the individual components of the flux controller are described.

The Flow Controller

The *Bronkhorst* EL-FLOW mass flow controller was used to measure and tune the nitrogen gas. Via an analog input (0-5 V) it is possible to control gas flows from 0 up to 900 l/h. The measurement of the effective flux goes via analog output also in the range 0-5 V. For more detailed information see [Bro].

*E*mbedded *L*ocal *M*onitor *B*oard (ELMB)

The active flux control is performed via ELMB [ELMa]. The ELMB is a multi purpose front end I/O system with a CAN interface, developed for the ATLAS experiment at CERN and already used in COMPASS for several monitoring tasks [ELMb]. The ELMB reads the thermometer on the silicon wafer (see Sec. 3.3.2) and, depending on the temperature value, adjusts the flux at the flowmeter, according to an algorithm developed specifically for this purpose. Furthermore the ELMB reads several parameters of the system (e.g. pressure in the cryostat) and comunicates them to the COMPASS *D*etector *C*ontrol *S*ystem (DCS) that monitors and stores the measured values into a data base. For a more detailed description of the usage of the ELMB in the silicon cooling infrastructure, see [See04].

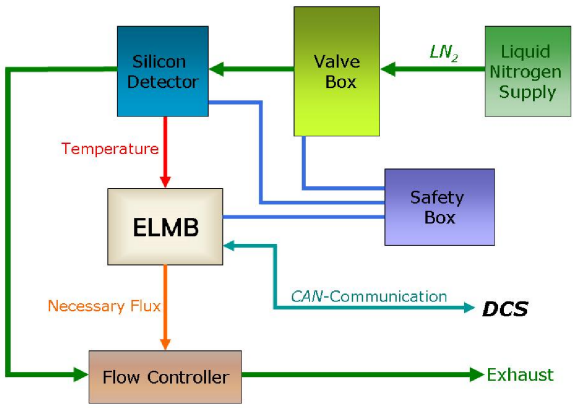

Figure 4.27: Schematical view of the cooling setup

The safety box

To prevent the damage of the system that may be caused by the failure of some components, a safety device was developed. The *Safety Box* consists of a series of logical circuits that monitors several values of the system (e.g. temperature, pressure, flux) and compares them with some predefined values. In case of anomalies, the safety box switches off the voltage of the readout electronics, the bias voltage of the detector and closes the cryogenic valve that provides the liquid nitrogen to the defective station. The safety box is designed to operate as stand alone component.

4.6.3 The principle of operation

Fig. 4.27 shows a schematic view of the cooling control system. The temperature of the silicon detector is read out via *PT100* by the ELMB. If the temperature is different then required, the ELMB sends a command to the flow controller, to vary the flux accordingly. The safety box switches off the station in the case of failure of a component of the system.

Chapter 5

The search for the Ξ^{--} pentaquark in COMPASS

The discovery of states composed of four quarks and an antiquark, collectively called pentaquarks, in 2003 opened a new era for hadron spectroscopy. The COMPASS experiment can make a valuable contribution to the investigation of pentaquarks, trough the high statistics and precision it offers.

In this chapter the search for an exotic pentaquark with charge -2 and strangeness +1, called Ξ^{--}, using data from the COMPASS experiment is described. In the first section an overview of the present understanding of pentaquark states is given, both from a theoretical and experimental point of view. In the second section the analysis method is described; the obtained results are presented and their interpretation in relation with other experiments is given.

5.1 Introduction

For many decades, high energy physics experiments have been devoted to the search of baryons and mesons that are not composed of three quarks or a quark−antiquark pair, respectively. Some of these states are assumed to have charge and quantum numbers in combinations which are forbidden for "normal" states, they are called exotics. The search for exotics has been rather unsuccesful, and in its 1988 review the Particle Data Group stated [PDG00b]:

> *The general prejudice against baryons not made of three quarks and the lack of any experimental activity in this area make it likely that it will be another 15 years before the issue is decided.*

The situation remained unchanged until 2003, when the evidence of a very narrow baryonic state was reported [LEP03]. The state, called Θ^+, has strangeness one, charge one and mass $\simeq$ 1540 MeV and decays in $\Theta^+ \rightarrow nK^+$. The Θ^+'s minimum quark content is $uudd\bar{s}$, i.e. a combination of four quarks and an antiquark; therefore the state has been called *pentaquark*. Despite of comprising more than three quarks, this state is still baryonic, since it has baryonic number $B = 1$. Almost a year later, another pentaquark was observed: the Ξ^{--} $(ddss\bar{u})$ at 1862 MeV. Since these first observations, several experiments have tried to confirm the existence of the pentaquarks leading to controversial results. Still today, there is no convincing experimental evidence that the pentaquarks exist.

From a theoretical point of view, the situation is not much clearer. States with more than three quarks are not forbidden in QCD, provided that they are colourless. However in the constituent quark model such a state would be expected to fall apart so rapidly that its width would be broad, contrary to the experimental results. Assuming QCD is still valid, several models have been developed proposing alternatives to the constituent quark model. Further experimental measurements are needed to discriminate between them, according on their predictions of observables quantities like mass, width and parity of pentaquarks.

In this section a review of two theoretical models and of the experimental results on pentaquark searches is given.

5.1.1 Theoretical models

Many different models which predict the existence of exotic baryons have been developed. They can be separated into those that are an extension of the constituent quark model (i.e. diquark model) and those which propose a completely different approach (i.e. chiral soliton model, see below). The recent experimental results on the Θ^+, concerning its light mass ($m \sim 1540$ MeV) and its narrow width ($\Gamma \lesssim 10$ MeV), have put harsh constraints on the theoretical predictions. In this section two models are outlined which are currently the most promising to understand exotic baryons.

Chiral soliton model

In the constituent quark model, a baryon is formed by three quarks which interact with each other via gluon exchange. The interactions between the constituent quarks and the ones in the Dirac sea are neglected. The quantum numbers (strangeness, beauty, etc.) of a baryon are simply the sum of the quantum numbers of its constituent quarks. In the chiral soliton model, or Skyrme model,

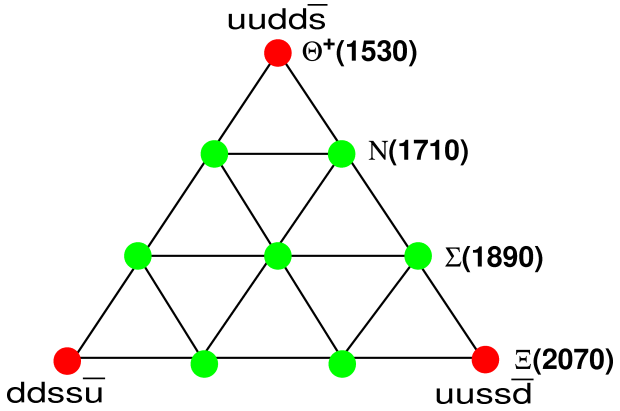

Figure 5.1: The baryonic antidecuplet $\overline{10}$. The particles in the corners have exotics quantum numbers.

a baryon is composed of three quarks which interact with each other and with the quarks in the Dirac sea. The strength of the interaction between quarks becomes weaker as the distance between the correspondent energy levels increases. In practice, the three "constituent" quarks interact only with the quarks in the most upper energy levels and not with all the quarks in the Dirac sea, which are infinite in number. This means that the calculation of physical quantities is a finite process. If one considers only the quarks in the light sector u, d and s, the classification of states in colour multiplets of the constituent quark model is still valid, but besides the well know **8** and **10** multiplets of baryons, an additional antidecuplet $\overline{10}$ appears in the chiral soliton model (Fig. 5.1). The particles which contain an antiquark, but not the corresponding quark (i.e. $ddss\overline{u}$) have exotic quantum numbers. In Fig. 5.1 the exotic baryons are the ones at the three corners of the triangle.

The most impressive prediction of the chiral soliton model has been the existence of an exotic baryon with charge +1, strangeness +1, mass $m \sim 1530$ MeV and width $\Gamma < 15$ MeV [Pol97], the Θ^+, that was experimentally claimed in 2003 by the LEPS experiment [LEP03].

Diquark model

The main idea of the diquark model is that two quarks form a strongly bounded compound qq if they form a colour antitriplet, flavour antisymmetric, spin singlet with even parity. Considering only the light quarks (u, d and s), it is possible to demonstrate [jaf04] that highly correlated scalar diquarks are the combinations ud, su and ds. If a state is dominated by one of these configurations, it should be lighter and more stable than states formed of other type of diquarks. This

model would also explain why no exotics mesons are observed (any combination of "good" diquark and antidiquark $qq\overline{q}\overline{q}$ will have the same quantum numbers of a standard meson). If one applies this model to pentaquarks one can find that all possible states formed by two diquarks and one antiquark $(qq)(qq)\overline{q}$ are organised in the following flavour multiplets:

- a nonet with spin $1/2$ and negative parity
- an octet with spin $1/2$ and positive parity
- a antidecuplet with spin $3/2$ and positive parity (like in the chiral soliton model)

Again, exotic pentaquarks are at the three corners of the antidecuplet (Fig. 5.1).

A complete review of the diquark model can be found in [jaf04].

5.1.2 Experimental results

The experimental observation of pentaquark states is probably the most important result in hadron spectroscopy in the last years, but it is not an easy task. Pentaquarks hare rare particles and their masses are predicted in a range where many other resonances are present ($m \sim 1500 - 2000$ GeV). If one considers the states at the corner of the antidecuplet (Fig. 5.1), they are manifestly exotics, which means their quantum numbers cannot belong to states composed of only three quarks. The identification of such exotic states is much easier, since no other resonances are expected in the corresponding invariant mass spectrum. This section contains a review of the published results for the observed pentaquarks. Many experiments are reanalysing the existing data in the quest for pentaquarks and new results are expected soon. Other dedicated experiments are being planned and will be carried out in the near future to improve our knowledge pentaquarks.

Measurements of Θ^+

The first experimental observation of a narrow baryon resonance with strangeness $S = +1$, called Θ^+, has been reported by the LEPS collaboration [LEP03]. Θ^+ contains one excess strange antiquark. According to the quark model it cannot be a three quark state but its minimum quark content has to be $uudd\bar{s}$ and it is manifestly exotic. The Θ^+ resonance corresponds to a sharp peak at 1.54 ± 0.001 GeV in the K^- missing mass spectrum of the $\gamma n \to K^+K^-n$

reaction. The width of the resonance has been estimated to be smaller than 25 MeV and the Gaussian significance of the peak is 4.6 σ. Several experimental groups have consistently confirmed this observation [DIA03], [CLA03], [SAP03], [HER03]. They observed a sharp peaks in the nK^+ or pK^0_S invariant mass spectra at the mass $\sim$ 1540 MeV and with a width limited by the experimental resolution. However, many other experiments have not observed any signal corresponding to a Θ^+ baryon in the same invariant mass spectra. Significant difference may come from the mechanism production, which can be substantially different in e^+e^- collisions rather than in photo-production, for example. Presently, more measurements with higher statistics are required. Moreover measurements of the parity and width of the Θ^+ will provide the only constraints to discriminate between different theoretical models (outlined in Sec. 5.1.1).

Measurements of $\Xi^{--}_{3/2}$ and $\Xi^{0}_{3/2}$

Presently, the only experimental observation of a state with charge $Q = -2$ and strangeness $S = -2$, called $\Xi^{--}_{3/2}$ (minimum quark content $uuss\bar{d}$), has been performed at the NA49 experiment at CERN [na403]. NA49 used a proton beam on a proton target at energy $\sqrt{s} = 17.2$ GeV with x_F in the range $[-0.25, 0.25]$. By analysing the decay chain:

$$\Xi^{--} \rightarrow \Xi^{-}\pi^{-} \rightarrow \Lambda^0\pi^{-}\pi^{-} \rightarrow p\pi^{-}\pi^{-}\pi^{-} \tag{5.1}$$

a narrow resonance in the $\Xi^-\pi^-$ invariant mass spectrum with a mass 1.862 ± 0.002 GeV has been observed. The width of the resonance is below the detector resolution $\Gamma < 0.018$ Gev. At the same mass position a signal in the $\Xi^-\pi^+$ invariant mass spectrum has also been observed. This is originated by the neutral and non exotic member of the $S = -2$ isospin quartet $\Xi^0_{3/2}$. Fig. 5.2 shows the $\Xi^-\pi^-$ and $\Xi^-\pi^+$ and their charge conjugate invariant mass spectra as measured by NA49.

The same decay channel has been analysed by other experiments (see, for example, [HER04] and [wa804]) with different beams, targets and energies. None has confirmed the observation of NA49. The search of the $\Xi^{--}_{3/2}$ and $\Xi^{0}_{3/2}$ within the COMPASS experiment is one of the main topics of science analysis presented in this thesis and will be extensively described in Sec. 5.2.

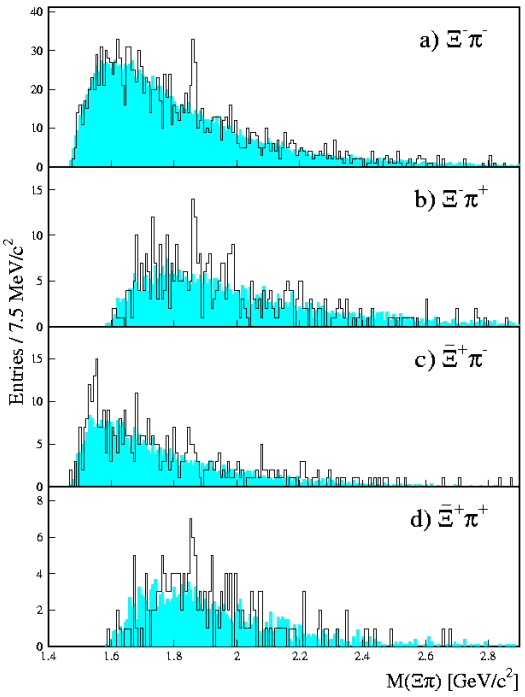

Figure 5.2: Invariant mass spectra for $\Xi^-\pi^-$, $\Xi^-\pi^+$, $\bar{\Xi}^+\pi^-$ and $\bar{\Xi}^+\pi^+$ as observed by the NA49 experiment.

Measurements of exotics not in the antidecuplet $\overline{10}(\Theta_c$ and $\Xi^-_{\frac{1}{2}})$

Considering more flavours than the u, d and s quarks, other heavier pentaquarks with charm or beauty can be formed. More recently a narrow signal in the pD^{*-} invariant mass spectrum has been observed by the H1 experiment at DESY [H104] with mass $m = 3099$ MeV and width $\Gamma < 12$ MeV. The signal is a candidate for the $\Theta_c(3099)$ pentaquark with minimum quark content $uudd\bar{c}$. The ZEUS experiment does not see any signal in the same channel.

The pentaquarks in the antidecuplet are predicted to have spin 3/2. An exotic state with spin 1/2 has been observed by NA49 in the channel $\Xi^-_{\frac{1}{2}} \rightarrow \Xi^{0*}\pi$. The candidate has a mass $m = 1855$ MeV [KA04]. The same decay chain has also been investigated in this thesis and it will be presented later.

5.2 The analysis of the COMPASS data

The spectroscopy of exotic states is one of the future goals of the COMPASS hadron program from 2006 (see Sec. 1.1.2). The data already obtained with the muon beam also offer the possibility to perform a search for pentaquarks. In particular, COMPASS is optimised for the *quasi−real photo-production*, that is when the energy transferred in the scattering process is small ($q^2 \leq 1$ MeV) and the scattering photon is almost *on-shell*. The Θ^+ pentaquarks have been observed in this production regime. Moreover the high resolution and the high statistics of the COMPASS spectrometer make it highly suitable for the analysis of rare particles, like the pentaquarks. Currently, study of the decay channel $\Theta^+ \rightarrow pK^0 \rightarrow p\pi^+\pi^-$ with the COMPASS data are being performed. In this work the channel $\Xi^{--} \rightarrow \Xi^-\pi^-$ has been analysed. As result, no positive evidence of a signal corresponding to such pentaquarks has been found; however, an upper limit for the production cross section has been determined.

5.2.1 Data Sample and luminosity

The following analysis has been performed on the COMPASS data from 2002 and 2003. PHAST version 7.006 has been used (see Sec. 1.2.3).

The luminosity L is the product of the beam flux I and the number of scattering centres in the target C. A built in function in PHAST provides the value of the integrated muon flux I. In total for the 2002 and 2003 data $I = 6.4 \cdot 10^{13}$. The number of scattering centres C per cm^2 is given by:

$$C = \frac{N_A}{V} l \sum A_i P_i \tag{5.2}$$

where N_A is the Avogadro's number, V is the target volume, l is the target length, A_i is the atomic mass of the i element of the target and P_i the number of its mols. The COMPASS target is mainly composed of ^6LiD, with some contamination from other materials. Tthe composition of the target material is given in Tab. 5.1, $C = 3.488 \cdot 10^{25} \text{cm}^{-2}$. The luminosity is then

$$L = I \cdot C = 6.4 \cdot 10^{13} \times 3.488 \cdot 10^{25}\ \text{cm}^{-2} = 2240 \cdot 10^{39}\ \text{cm}^{-2} = 2240\ \text{pb}^{-1} \tag{5.3}$$

Element	# of mols	Atomic number
H	0.1019	1
D	44.5370	2
^3He	3.6207	3
^4He	10.9118	4
^6Li	42.8429	6
^7Li	1.7950	7
C	0.0080	12
F	0.0160	19
Ni	0.0057	58.6
Cu	0.0136	63.6

Table 5.1: Composition of the target material.

5.2.2 Event topology

A signature of the S=-2 pentaquark Ξ^{--} is related to the following decay chain (Fig. 5.3):

$$\Xi^{--} \to \Xi^- \pi^- \to \Lambda^0 \pi^- \pi^- \to p \pi^+ \pi^- \pi^-. \tag{5.4}$$

Also the following decay chain, originating from the well known Ξ^{0*} state is considered:

$$\Xi^{0*} \to \Xi^- \pi^+ \to \Lambda^0 \pi^- \pi^+ \to p \pi^+ \pi^- \pi^+. \tag{5.5}$$

It is useful to remember that, in the $\Xi^-\pi^+$ invariant mass spectrum, NA49 has observed a signal corresponding to the neutral member of the isospin multiplet (see Sec. 5.1.2).

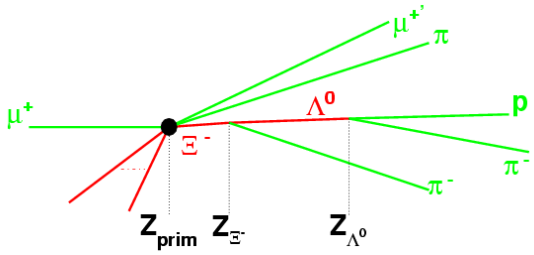

Figure 5.3: The decay chain considered in this analysis: Z_{prim}, Z_{Ξ^-}, Z_{Λ^0} are the longitudinal coordinates of the primary vertex, the Ξ^- and the Λ^0 decay vertex, respectively.

The reconstruction of such events start from the end of the decay chain:

- events with Λ^0 candidates are selected;
- in this subsample events with Ξ^- are identified;
- Ξ^- are combined with a pion track to reconstruct Ξ^{--} and Ξ^{0*};
- Ξ^{0*} are combined with a pion track to reconstruct $\Xi^{0*}\pi$ states.

During the 2002 and 2003 data runs, the RICH detector could not perform an accurate particle identification. A clear p/π separation could be obtained only in a limited region of the acceptance. This means a clear particle identification could be achieved at the cost of a significant reduction of the statistics. Therefore the data form the RICH detector are not used in this analysis. Only muons are clearly identified using the muon filters (Sec. 1.2.2). The invariant mass of a particle is reconstructed making assumptions on the masses of the daughter particles.

An instructive example is the case of the Λ^0 decaying in the $p\pi^-$ channel. For each pair of particles of opposite charge, the positive one is assumed to be a proton and the negative one a pion. If the two particles are really a proton and a pion coming from a Λ^0 decay, their invariant mass is Gaussianly distributed around the value of the Λ^0 mass with dispersion that is the convolution of the detector resolution and the width of the particle. If they are not coming from the Λ^0 decay, they will contribute to the background. Altogether, the $p\pi^-$ invariant mass spectrum, will look like a Gaussian peak corresponding to the Λ^0 superimposed on the background. Comparing the number of events under the Gaussian peak and

the background in the same region gives an idea of the quality of the reconstruction. As it will be shown in the following sections, a clear reconstruction of Λ^0, Ξ^- and Ξ^{0*} particles has been achieved even without using the RICH informations.

5.2.3 Preliminary selection of events

The first selection to be applied to the event sample concerns the primary interaction vertex, that is the interaction point of a muon from the beam and a nucleon in the target.

In CORAL (Sec. 1.2.3) a primary vertex is identified by containing an incoming muon track. A reconstructed event can have zero, one or even more primary vertices. To reconstruct the kinematics of the Ξ baryons production, the informations on the energy transferred in the primary interaction are needed. Therefore events with zero primary vertex have been discarded. In case of events with more than one primary vertex, the one with more associated tracks has been selected. The event sample after the cuts on the primary vertex is reduced to $\sim$ 90% of the original event sample.

The beam muons can interacts not only in the target, but also with any other material surrounding it (air, magnet, coolant). These events have been discarded requiring the position of the primary vertex to be inside the target volume. This cut further reduces the sample to $\sim$ 65%. Fig. 5.4 shows the position of the reconstructed primary vertex and the cuts applied. It is useful to remember that the target for the muon program is made of two cylindrical rods of ^6LiD of 1.5 cm radius separated by 10 cm. The peaks at ~ -150 and $\sim$ 60 cm in the z[1] distribution correspond to the windows of the target spectrometer.

Also if the scattered muon from the primary vertex is not reconstructed the measurement of the energy transferred in the scattering process is not possible. Therefore only events with at least one scattered muon are selected, corresponding to a further $\sim$ 20% reduction in the number of events.

To each reconstructed particle the following additional cuts are applied:

- the particle is neither identified as a muon nor as an antimuon;
- the last point of the particle's track is located at Z $>$ 360 cm (in order to measure its charge with SM1);
- the momentum of the particle is $\leq$ 140 GeV, to exclude unidentified muons.

[1] In the COMPASS reference system the z coordinates coincides in direction and versus with the beam. The x and y coordinates are in the transverse plane respect to the beam.

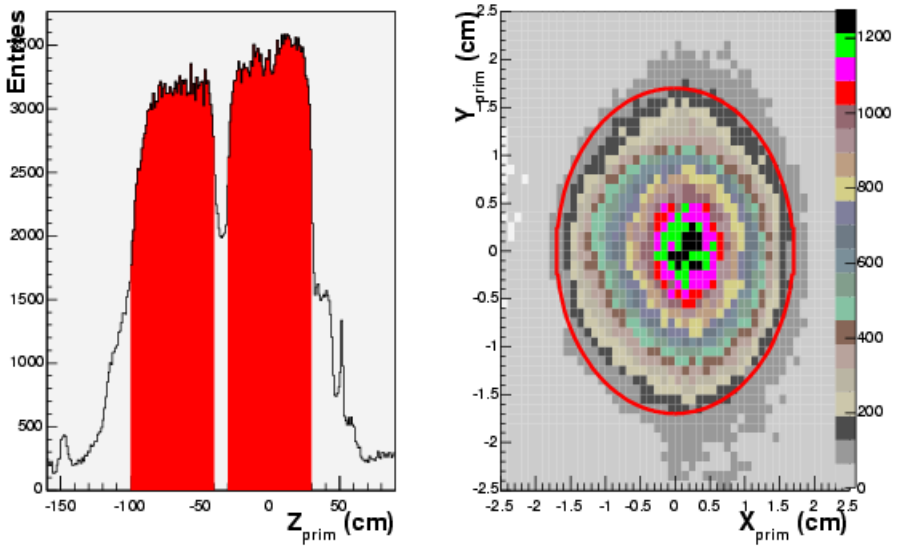

Figure 5.4: The primary vertex distribution. The z coordinate (left plot) is in the longitudinal direction respect to the beam and the x and y coordinates (right plot) are in the transverse direction. The red shaded area in the left plot and the red continuous line in the right plot show the applied cuts.

5.2.4 Λ^0 and $\overline{\Lambda^0}$ reconstruction

The next step in the analysis is the Λ^0 reconstruction. The Λ^0 decays in $p\pi^-$ with a 63.9% branching ratio. This decay channel is better suited to the reconstruction with respect to the other predominant channel ($n\pi^0$, 35.8% branching ratio) for the decay products are charged particles and can be directly tracked in the spectrometer (while neutral particles are not). If defining the V^0 as a vertex with only two outgoing particles with opposite charge, the decay vertex of the Λ^0 is a V^0 in the selected decay channel. The following cuts are applied to the V^0:

- V^0 is not classified as primary vertex, to discard Λ^0 produced in the primary interaction;
- $Z_{\Lambda^0} \geq Z_{\text{prim}}$, to search for the right event topology;
- the normalised χ^2 of the V^0 is smaller than 4.

On each outgoing track from the V^0 the following cuts are applied:

- last point of the track is located at Z $>$ 360 cm. This cut selects the particles which cross the first magnet SM1 and, therefore their charge can be clearly measured (see Sec. 1.2.2);
- the particle is neither identified as muon nor as antimuon;
- the momentum of the particle is $<$ 140 GeV, to reject muons from the beam not correctly identified in the muon filters (see Sec. 1.2.2).

Assuming the track corresponds to a certain particle, it is possible to reconstruct its Lorentz vector combining the 3−momentum of the track as given by CORAL and the mass. For the reconstruction of the Λ^0, the proton mass is assigned to the track of the positive particle and the pion mass to the negative one. In case of $\overline{\Lambda^0}$ the mass assignments are opposite. With v^μ the Lorentz vector of a particle

$$v^\mu_{\Lambda^0} = v^\mu_p + v^\mu_{\pi^-} \tag{5.6}$$

and one can reconstruct the mass, the track and the momentum of the Λ^0.

Λ^0 enrichment

The V^0s do not come only from Λ^0 decay. The conversion of a photon in a e^+e^- pair or the decay of other neutral particles in two particles of opposite charge also form a V^0. Since no direct particle identification (as it could be done in the RICH) is used in this analysis, the above-mentioned processes may be indistinguishable from a Λ^0 decay and contribute to the Λ^0 background. Furthermore it has been observed that the combinatorial background for the Λ^0 varies strongly depending on the position of the V^0 along the incoming muon beam direction, Z_{Λ^0}. The background studies are presented in this section.

e^+e^- background. One parameter to distinguish between the $p\pi^-$ from Λ^0 decay and e^+e^- from photon conversion is the angle α between the Λ^0 momentum vector in the lab system and the momentum vector of one of the daughter particles in the Λ^0 CMS. Fig. 5.5 shows the $\cos\alpha$ distribution (left plot).

The decay products of an upolarised Λ^0 are uniformly distributed in the solid angle. The e^+ and e^- from the conversion of a real photon have a small transverse momentum and hence are mostly emitted at small angles, then the peaks in the distribution for $\cos\alpha \simeq \pm 1$ comes more likely from them. One can estimate the effects of the cut on the $p\pi^-$ invariant mass (Fig. 5.5, right): the black histogram is the $p\pi^-$ invariant mass distribution without any cut on the $\cos\alpha$; the red histogram has the cut $|\cos\alpha| < 0.9$ (red area cosine plot, Fig. 5.5, left);

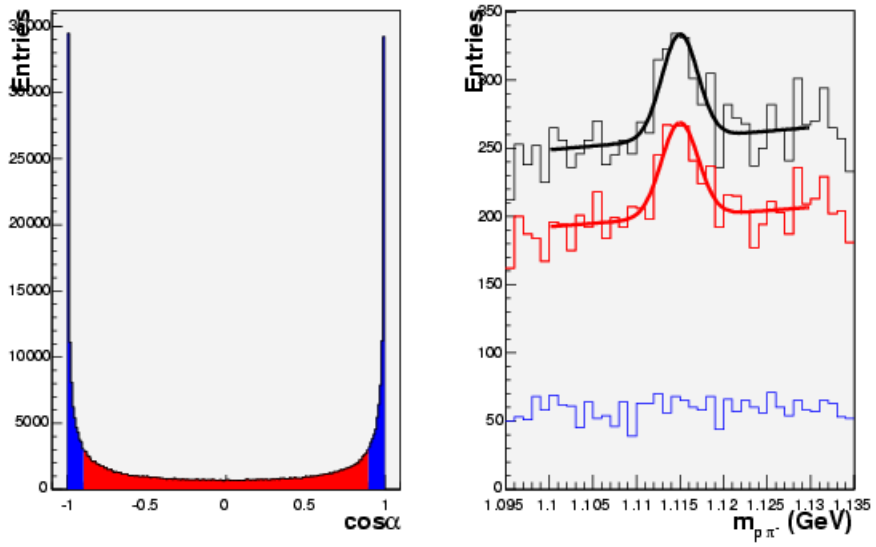

Figure 5.5: Right: $\cos\alpha$ distribution. Left: $p\pi^-$ invariant mass distribution. The continuous curves are the fit with a Gaussian function plus a polynomial. For explanation see text.

the blue histogram has the cut $|\cos\alpha| \geq 0.9$ (blue area in the left plot). The blue histogram does not show any peak corresponding to reconstructed Λ^0. Therefore the events with $|\cos\alpha| \geq 0.9$ can be discarded with only a very small loss in the Λ^0 signal.

K^0 background. The K^0 decays in $\pi^+\pi^-$ and it is a potential source of background for the Λ^0 reconstruction. Fig. 5.6 shows the $\pi^+\pi^-$ invariant mass distribution (left plot), with a K^0 peak at $\sim$ 0.5 GeV. The peak has been fit with a Gaussian function plus a polynomial for the background. The width of the Gaussian is $\sigma = 8$ MeV.

The effect of excluding the region of the K^0 peak can be seen in the $p\pi^-$ invariant mass of Fig. 5.6 (right plot): the black histogram is the distribution without any cut; the red histogram contains all events under the K^0 peak within 3σ (red area in the left plot); the blue histogram contains all events out of the K^0 peak within 3σ (blue area in the left plot). In the red histogram a small peak corresponding to reconstructed Λ^0 is still visible. The signal to background ratio of this last sample is small, moreover the events have not been discarded since a clear selection of Λ^0 from Ξ^- decay can be done, as will be explained in Sec. 5.2.5.

The longitudinal position of the Λ^0 decay vertex, Z_{Λ^0}. It has been observed that the background in the Λ^0 reconstruction strongly depends on the position of the

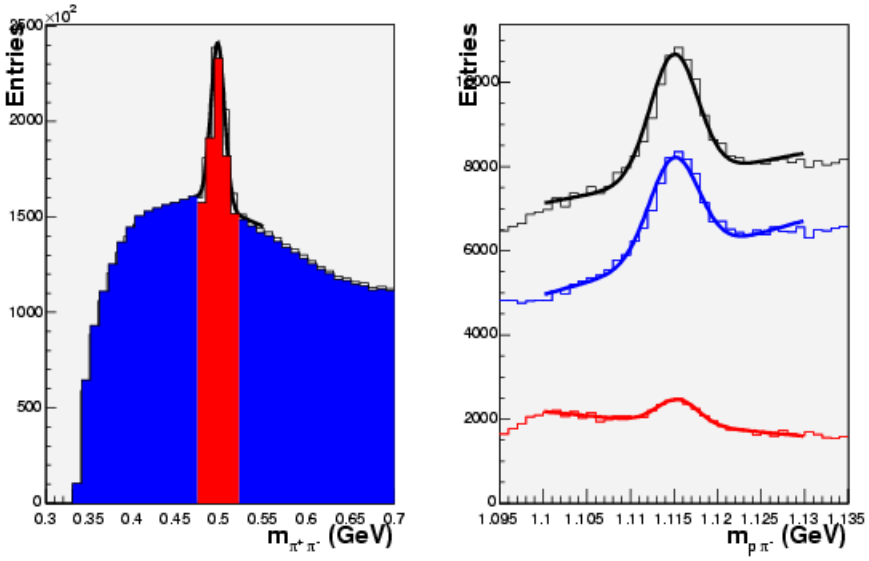

Figure 5.6: Right: $\pi^+\pi^-$ invariant mass distribution. A clear peak for K^0 is visible. Left: $p\pi^-$ invariant mass distribution. The continuous curves are the fit with a Gaussian function plus a polynomial. For explanation see text.

Z_{Λ^0}. Fig. 5.7 shows the $p\pi^-$ invariant mass spectra for three different intervals of Z_{Λ^0}. The left plot contains all Λ^0 decaying in the most downstream cell of the target or in the 10 cm between the cells. The central plot contains the Λ^0 decaying in the most downstream cell of the target. The left plot contains the Λ^0 decaying downstream of the target. A peak at the Λ^0 mass is visible in all three samples, but the first two samples are dominated by the background. Two two most likely reasons are:

- the combinatorial background is much higher in the target, due to the higher number of secondary interactions in the target material.
- the acceptance of the target magnet: if the Λ^0 decay products are emitted at large angle, they can be absorbed by the magnet and no Λ^0 reconstruction is possible; the acceptance decreases with increasing the distance between Z_{Λ^0} and the end cup of the magnet. A detailed study can be found in [Wie03]

The signal to background ratio for the three distributions in Fig. 5.7 has been calculated. The invariant mass distributions are fitted with a Gaussian function plus a background parabolic function. The signal and the background for Λ^0 and $\overline{\Lambda^0}$ are estimated from the fit parameters and are shown in Tab. 5.2. Because of the extremely small signal to background ratio, only Λ^0 decaying downstream of the target have been used for further analysis ($Z_{\Lambda^0} > 30$ cm).

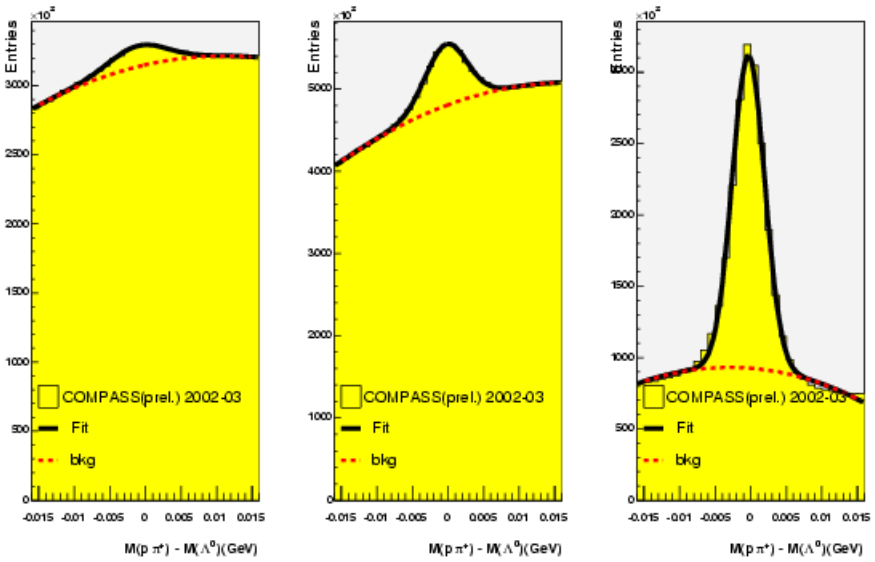

Figure 5.7: The $p\pi^-$ invariant mass spectra for three different intervals of Z_{Λ^0}: Λ^0 decaying in the first target cell (left plot), in the second target cell (central plot), outside of the target (right plot).

	Λ^0			$\overline{\Lambda^0}$		
	S	N	S/N	S	N	S/N
$-30 > Z_{\Lambda^0} > -100$	3×10^5	1.5×10^7	0.02	3.8×10^5	3.6×10^7	0.01
$30 > Z_{\Lambda^0} > -30$	1.1×10^6	1.6×10^7	0.07	0.5×10^6	3.1×10^7	0.02
$Z_{\Lambda^0} > 30$	2.5×10^6	1.2×10^6	2.09	1.3×10^6	2.3×10^6	0.5

Table 5.2: Signal (S), noise (N) and signal to noise ratio (S/N) for Λ^0 and $\overline{\Lambda^0}$. The first line corresponds to particle which decays in the first cell of the target, the second line to the second cell, the third line to particles which decays outside of the target.

Final results A clean Λ^0 and $\overline{\Lambda^0}$ sample is selected for further analysis. Fig. 5.8 shows the $p\pi^-$ and $\overline{p}\pi^+$ invariant mass spectra with respect to the nominal mass of the Λ^0. The continuous (black) curves result from a fit of a Gaussian and a parabolic background. The dotted (red) lines show the background. The total number of Λ^0 and $\overline{\Lambda^0}$ events for COMPASS, the central value and the width of the fit on their mass distribution are shown in Tab. 5.3.

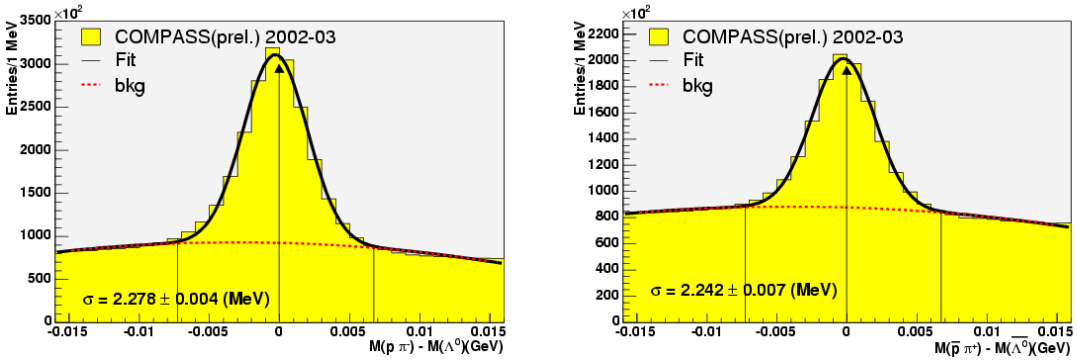

Figure 5.8: The $p\pi^-$ (left) and $\overline{p}\pi^+$ (right) invariant mass spectra respect to the $m^{\mathrm{PDG}}_{\Lambda^0}$. The lateral vertical lines show the mass cut applied in the $\Lambda^0\pi^-$ reconstruction.

	Λ^0	$\overline{\Lambda^0}$
Events	1245800 $\pm$ 2400	638000 $\pm$ 2200
mass (MeV)	1115.390 $\pm$0.003	1115.440 $\pm$0.005
width (MeV)	2.278 $\pm$ 0.004	2.242 $\pm$ 0.007

Table 5.3: Number of Λ^0 and $\overline{\Lambda^0}$ in COMPASS data from 2002 and 2003, the central value and the width of the fit on their mass distribution

5.2.5 Ξ^- and $\overline{\Xi^-}$ reconstruction

The next step is the Ξ^- reconstruction. The Ξ^- decays in $\Lambda^0\pi^-$ with a 99.89 $\pm$ 0.035% [PDG00a] branching ratio. Λ^0 candidates with mass $|m_{p\pi} - m_{\Lambda^0}| \leq 3 \cdot \sigma = 7$ MeV are selected for further analysis (see Sec. 5.2.4). For Λ^0 candidates within this mass window the nominal mass $m^{\mathrm{PDG}}_{\Lambda^0}$ [PDG00a] is assumed for further analysis. An additional negative particle with the following characteristics is requested:

- the particle has not been used for the reconstruction of the Λ^0;

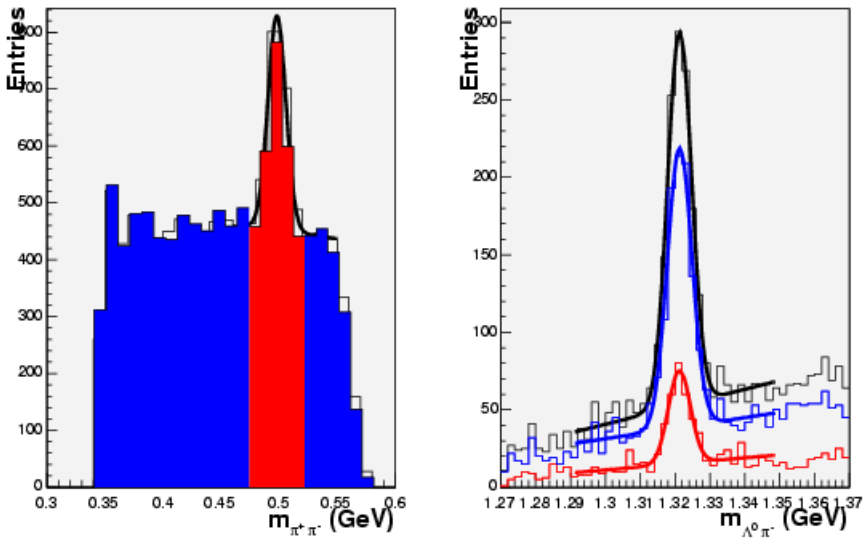

Figure 5.9: Right: $\pi^+\pi^-$ invariant mass distribution. A clear peak for K^0 is visible. Left: $\Lambda^0\pi^-$ invariant mass distribution. The continuous curves are the fit with a Gaussian plus a linear functions. For explanation see text.

- the track is not connected to the primary vertex;
- the closest distance of approach (CDA) between the particle's track and the Λ^0 track is $<$0.8 cm;
- $Z_{prim} \leq Z_{\Xi^-} \leq Z_{\Lambda^0}$

The pion mass is then attributed to this negative particle. In terms of Lorentz vectors:

$$v^{\mu}_{\Xi^-} = v^{\mu}_{\Lambda^0} + v^{\mu}_{\pi^-} \tag{5.7}$$

and reconstructs the mass, the track and the momentum of the Ξ^-. In the case of a $\overline{\Xi^-}$, a positive pion is coupled with a $\overline{\Lambda^0}$.

An interesting point concerns the effect of the K^0 background on the Ξ^- reconstruction (Sec. 5.2.4). As previously mentioned, despite being a source of background for the Λ^0 signal, no cut on the K^0 mass has been applied.

The left plot in Fig. 5.9 shows the $\pi^+\pi^-$ invariant mass distribution with a peak at $\sim$ 0.5 Gev. The effect on the $\Lambda^0\pi^-$ invariant mass of excluding the region of the K^0 peak can be seen in Fig. 5.9 (right plot): the black histogram is the distribution

without any cut; the red histogram contains all events under the K^0 peak within 3σ (red area in the left plot); the blue histogram contains all events out of the K^0 peak within 3σ (blue area in the left plot). In the red histogram a clear peak with negligible background corresponding to reconstructed Ξ^- is visible. Most likely, false Λ^0 are rejected in the analysis when the match with an additional particle is required. Not rejecting the K^0 background in the Λ^0 reconstruction is justified by the Ξ^- analysis.

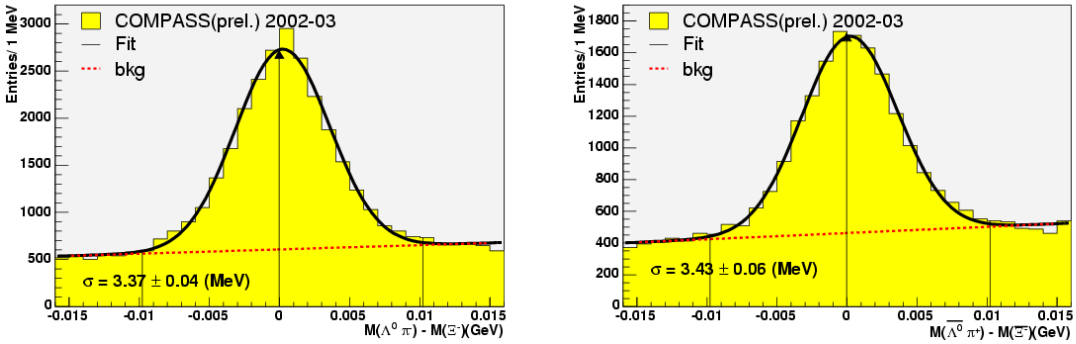

Figure 5.10: The $\Lambda^0\pi^-$ (left) and $\overline{\Lambda^0}\pi^+$ (right) invariant mass spectra relative to the $m^{\mathrm{PDG}}_{\Xi^-}$. The vertical lines show the mass cut applied in the $\Xi^-\pi$ reconstruction.

Fig. 5.10 shows the $\Lambda^0\pi^-$ invariant mass spectra with respect to the Ξ^- nominal mass. The black (continuous) curves result from a fit of a Gaussian and a linear background. The red (dotted) lines show the background.

In view of the reconstruction of the exotic Ξ^{--} state observed by the NA49 experiment (see Sec. 5.1.2), it is interesting to compare the total number of Ξ^- and $\overline{\Xi^-}$ events for NA49 and COMPASS as shown in Tab. 5.4. For the COMPASS data the central value and the width of the fit on their mass distribution are also shown. In the present analysis of the COMPASS data the number of reconstructed Ξ^- used for the search of the Ξ^{--} pentaquark is more than 10 times the number of reconstructed Ξ^- in NA49.

5.2.6 Ξ^{0*}, $\overline{\Xi^{0*}}$, Ξ^{--} and $\overline{\Xi^{--}}$ selection

One of the more interesting point of this work is the search of the exotic baryon resonance $\Xi^{--} \rightarrow \Xi^-\pi^-$ and of its non−exotic partner in the antidecuplet (Sec. 5.1.1) $\Xi^0_{3/2} \rightarrow \Xi^-\pi^+$, in order to confirm the results of the NA49 experiment [na403]. To perform this analysis, Ξ^- candidates with mass $|m_{\Lambda\pi} - m_{\Xi^-}| \leq 3 \cdot \sigma =$ 10 MeV are selected; σ is calculated from the m_{Ξ^-} distribution (Fig. 5.10). To these

	Ξ^-	$\overline{\Xi^-}$
NA49	1640	551
COMPASS	17930 ± 210	10620 ± 180
mass (MeV)	$1.32154 \pm 4 \times 10^{-2}$	$1.32153 \pm 5 \times 10^{-2}$
width (MeV)	3.37 ± 0.04	3.43 ± 0.06

Table 5.4: Number of Ξ^- and $\overline{\Xi^-}$ in COMPASS and NA49 For the COMPASS data the central value and the width of the fit on their mass distribution are also shown.

candidates the $m_{\Xi^-}^{\mathrm{PDG}}$ [PDG00a] is assigned. An additional particle with the following characteristics is requested:

- the particle has not been used for Λ^0 and Ξ^- reconstruction;
- the track is connected to the primary vertex; since the searched resonances decay immediately after production, their production and decay vertices have to coincide;

The pion mass is then attributed to this particle. Matching the Ξ^- with a positive pion, one reconstructs the spectrum containing Ξ^{0*} candidates, with a negative pion the Ξ^{--} candidates. An opposite matching is done for the antiparticles $\overline{\Xi^{0*}}$ and $\overline{\Xi^{--}}$. Fig. 5.11 shows the invariant mass spectra of these four states. No significant excess of events is detected in the mass region around $m = 1862$ MeV where NA49 has observed a signal, while clear peaks for $\Xi^{0*}(1530)$ and its antiparticle are seen. Zoomed spectra are shown in Fig. 5.2.6, showing the mass region around the $\Xi^{0*}(1530)$.

The black (continuous) curves result from a fit of a Gaussian and a parabolic background. The red (dotted) lines show the background. The total number of reconstructed $\Xi^{0*}(1530)$ and $\overline{\Xi^{0*}}(1530)$, the central value and the width of the fit on their mass distribution are shown in Tab. 5.5. The phase space shown with the the NA49 signal does not include the Ξ^{0*} region (see Fig. 5.2), therefore no comparison between the number of Ξ^{0*} reconstructed events in NA49 and COMPASS is possible.

It is convenient to introduce the dimensionless variable *x-Feynman* x_{F} that quantifies, in the centre of mass frame, the fraction of beam's momentum contained in the longitudinal momentum component of the detected particle. x_{F} is defined as [PDG00a]:

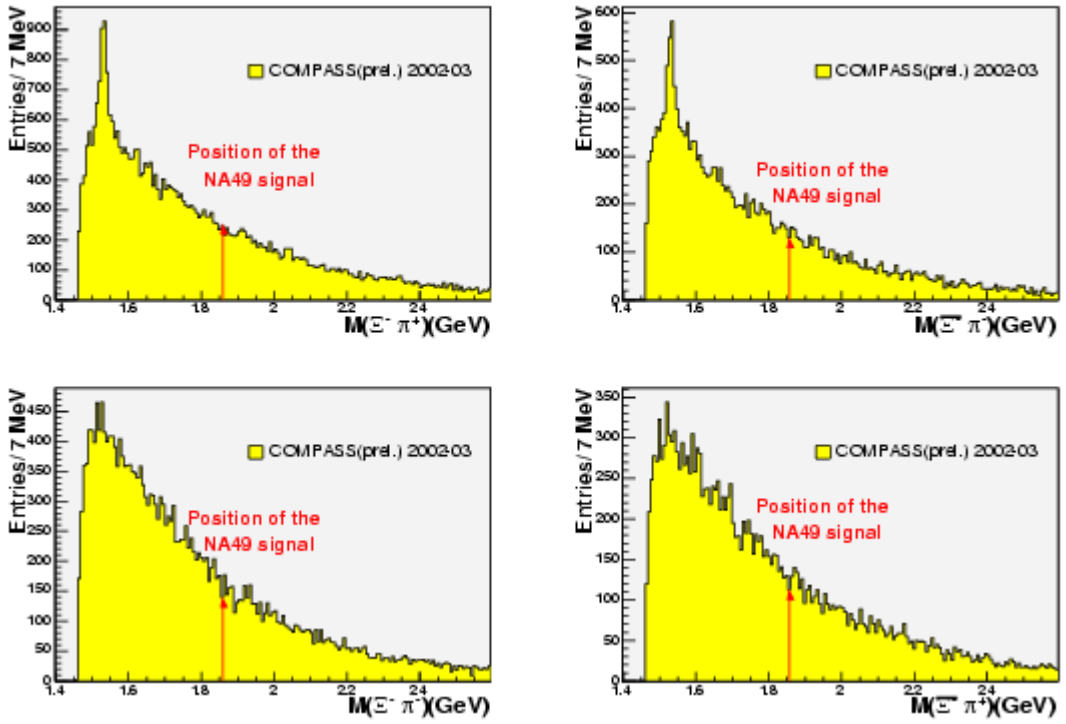

Figure 5.11: $\Xi^-\pi^+$ (top left), $\overline{\Xi^-}\pi^-$ (bottom left), $\Xi^-\pi^-$ (top right), $\overline{\Xi^-}\pi^+$ (bottom right) invariant mass spectra.

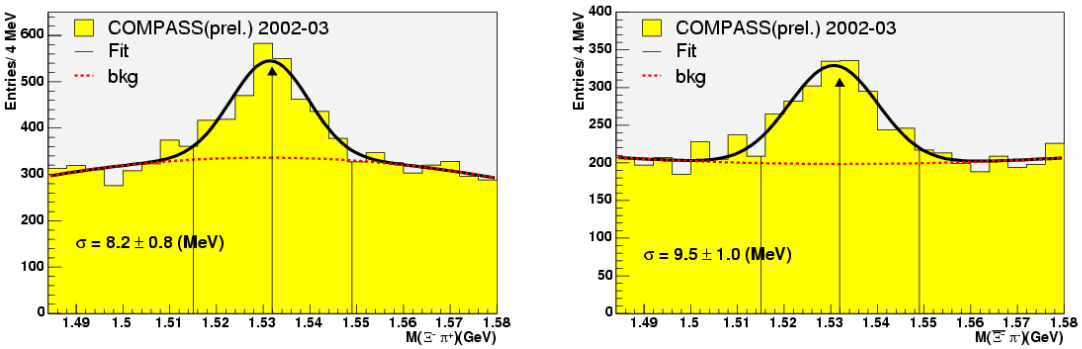

Figure 5.12: The $\Xi^-\pi^+$ (left) and $\overline{\Xi^-}\pi^-$ (right) invariant mass spectra. The vertical lines show the mass cut applied in the further $\Xi^{0*}\pi$ reconstruction (see Sec. 5.2.10).

	Ξ^{0*}	$\overline{\Xi^{0*}}$
Events	1080 ± 90	780 ± 80
mass (MeV)	1531.5 ± 0.6	1530.7 ± 0.8
width (MeV)	8.2 ± 0.8	9.5 ± 1.0

Table 5.5: Number of Ξ^{0*} and $\overline{\Xi^{0*}}$ in COMPASS 2002 and 2003 data, the central value and the width of the fit on their mass distribution

$$x_F \simeq \frac{2p_{z\,cm}}{\sqrt{s}} \tag{5.8}$$

where $p_{z\,cm}$ is the longitudinal momentum of the particle in the **C**entre of **M**ass **S**ystem (*CMS*) of the proton p and the virtual photon γ^*, and $s = (p_p + p_{\gamma^*})^2$ is the square of the total energy available for the process. The x_F is a useful parameter to understand the production mechanism of the particles in a given reaction. In the CMS, x_F can go from -1 to 1. $x_F \simeq 1$ means that the particle produced in the interaction takes most of the momentum of the beam particle; this regime is called *current fragmentation region*. $x_F \simeq -1$ means that the particle is produced in the fragmentation of the target particle and one speaks of a *target fragmentation region*. The x_F distribution for the $\Xi^-\pi$ states in the $p\gamma^*$ CMS is shown in Fig. 5.13.

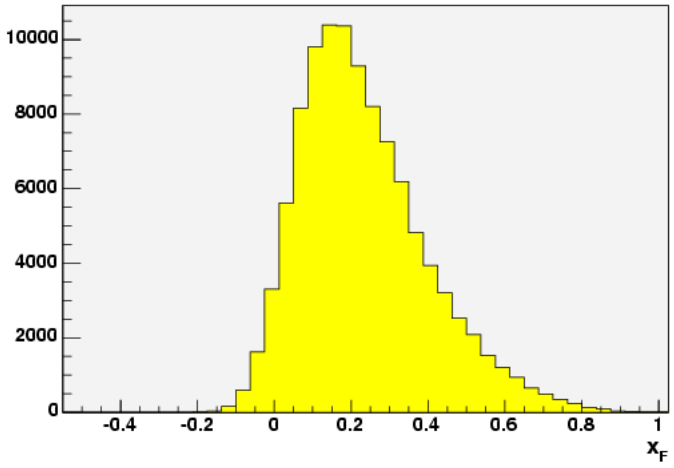

Figure 5.13: The x_F distribution for $\Xi^-\pi$ in the $p\gamma^*$ CMS.

The $\Xi^-\pi^-$ invariant mass distributions are plotted for different intervals of x_F, to check if the Ξ^{--} is seen with a particular kinematics (Fig. 5.14). The same is done

for the $\Xi^-\pi^+$ invariant mass distributions (Fig. 5.15). x_F goes from -0.1 to 0.7 in steps of 0.1. No visible excess of events corresponding to the Ξ^{--} in any of the x_F intervals is observed.

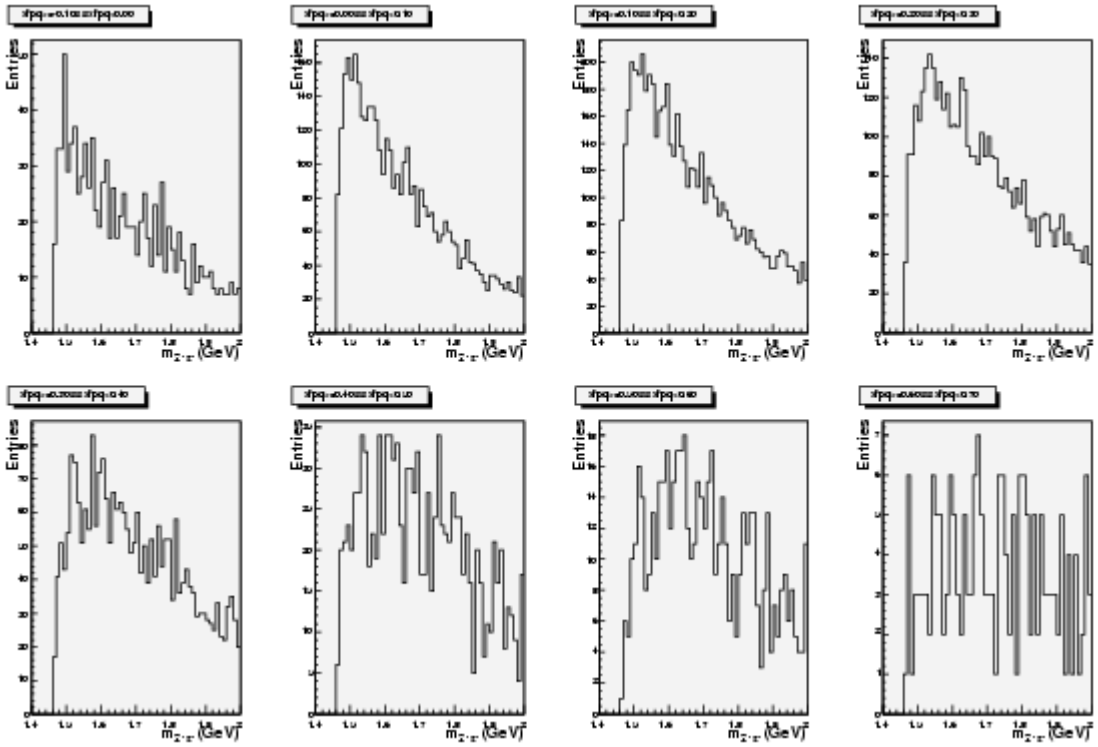

Figure 5.14: $\Xi^-\pi^-$ invariant mass distributions in different intervals of x_F. Starting from the first plot in the upper left corner, x_F goes from -0.1 to 0.7 in steps of 0.1.

In case of the Ξ^{0*}, it is possible to determine the number of particles in each x_F interval and, with the help of the reconstruction efficiency from Monte Carlo, one can calculate the production cross section as function of x_F. Since the Ξ^{0*} lies at $\sim$ 1530 MeV and the mass threshold on the phase space is $\sim$ 1460 MeV, it is difficult to estimate the background correctly. In the $\Xi^-\pi^-$ invariant mass distribution, no further signals are expected, and it can be used to estimate the $\Xi^-\pi^+$ phase space and thus the background under the Ξ^{0*} signal. Since the $\Xi^-\pi^+$ and the $\Xi^-\pi^-$ distributions have a different number of events, the latter has to be scaled to be a good estimation of the phase space. The multiplication factor f has been calculated for each x_F interval by dividing the two histograms bin by bin ($\Xi^-\pi^+/\Xi^-\pi^-$), as shown in Fig. 5.16, and taking the average value f excluding the Ξ^{0*} peak region. The ratio of the distributions is fitted with a constant excluding the region of the Ξ^{0*} peak. The values of f for each x_F interval are shown in Tab. 5.6.

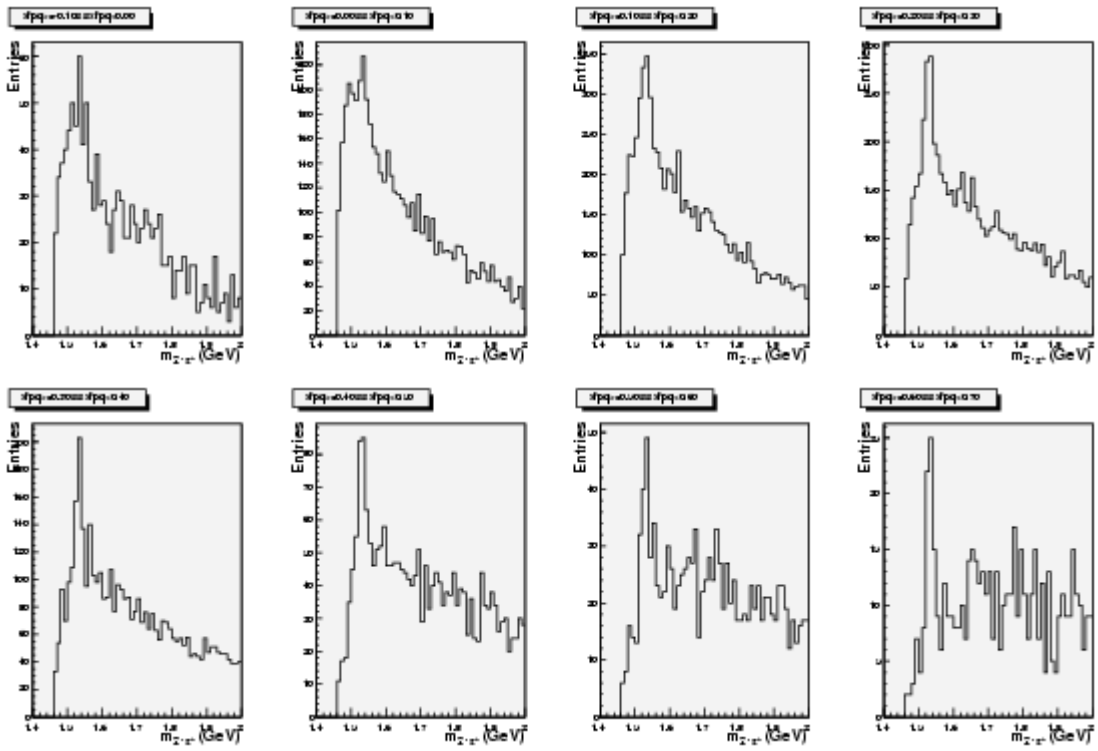

Figure 5.15: $\Xi^-\pi^+$ invariant mass distributions in different intervals of x_F. Starting from the first plot in the upper left corner, x_F goes from -0.1 to 0.7 in steps of 0.1.

x_F	f
-0.1−0.0	0.99
0.0−0.1	1.24
0.1−0.2	1.29
0.2−0.3	1.38
0.3−0.4	1.49
0.4−0.5	1.75
0.5−0.6	1.95
0.6−0.7	2.20

Table 5.6: Multiplication factors f for the $\Xi^-\pi^-$ invariant mass distribution in different intervals of x_F.

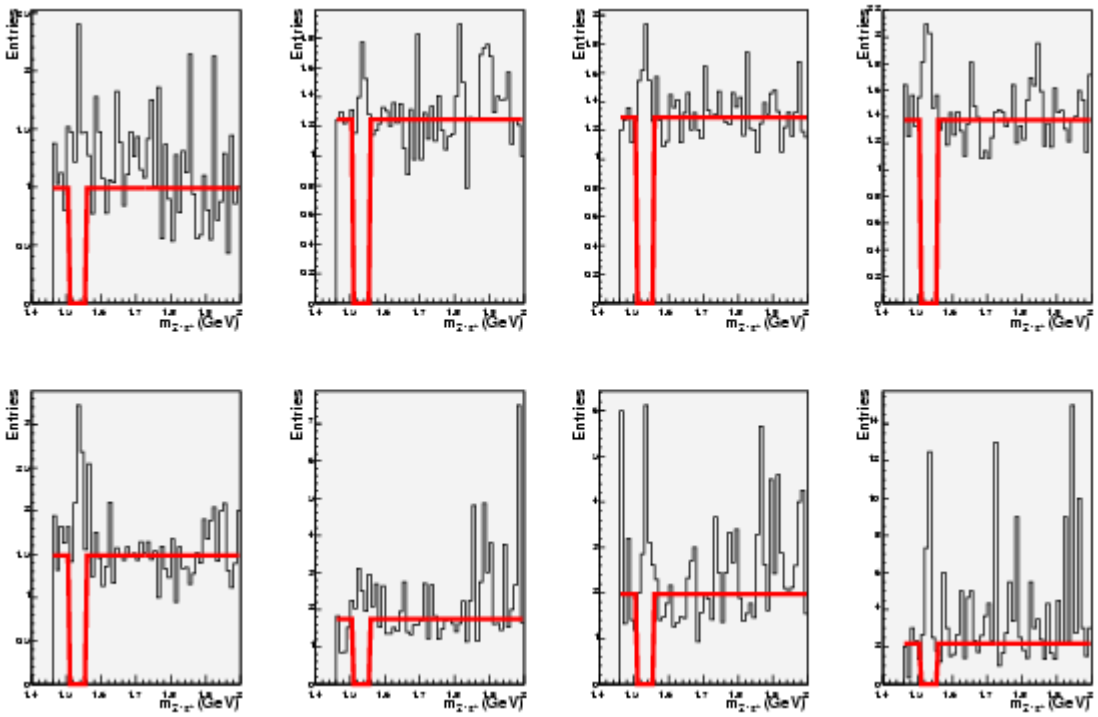

Figure 5.16: $\Xi^-\pi^-/\Xi^-\pi^+$ distribution in different intervals of x_F. The ratio has been fitted with a constant function excluding the Ξ^{0*} peak region. The values of the constant are shown in Tab. 5.6.

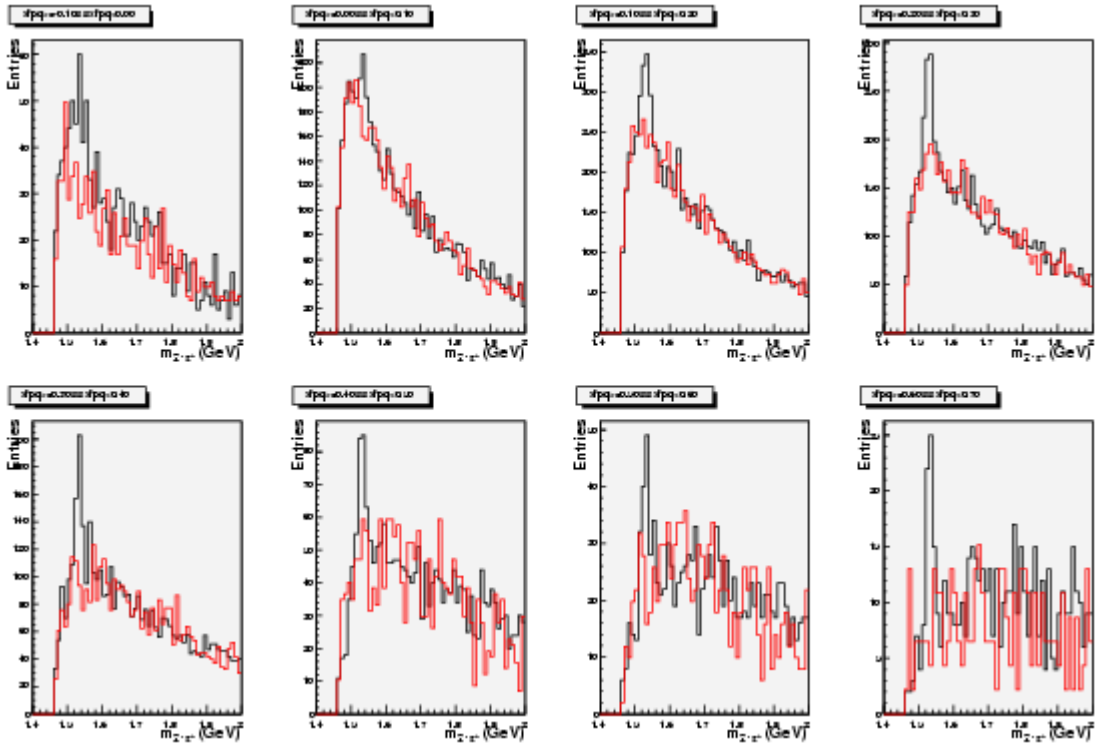

Figure 5.17: $\Xi^-\pi^+$ (black histograms) and $\Xi^-\pi^-$ (red histograms) invariant mass distributions in different intervals of x_F (from -0.1 to 0.7 in steps of 0.1). The red histograms have been scaled according to the factors of Tab. 5.6.

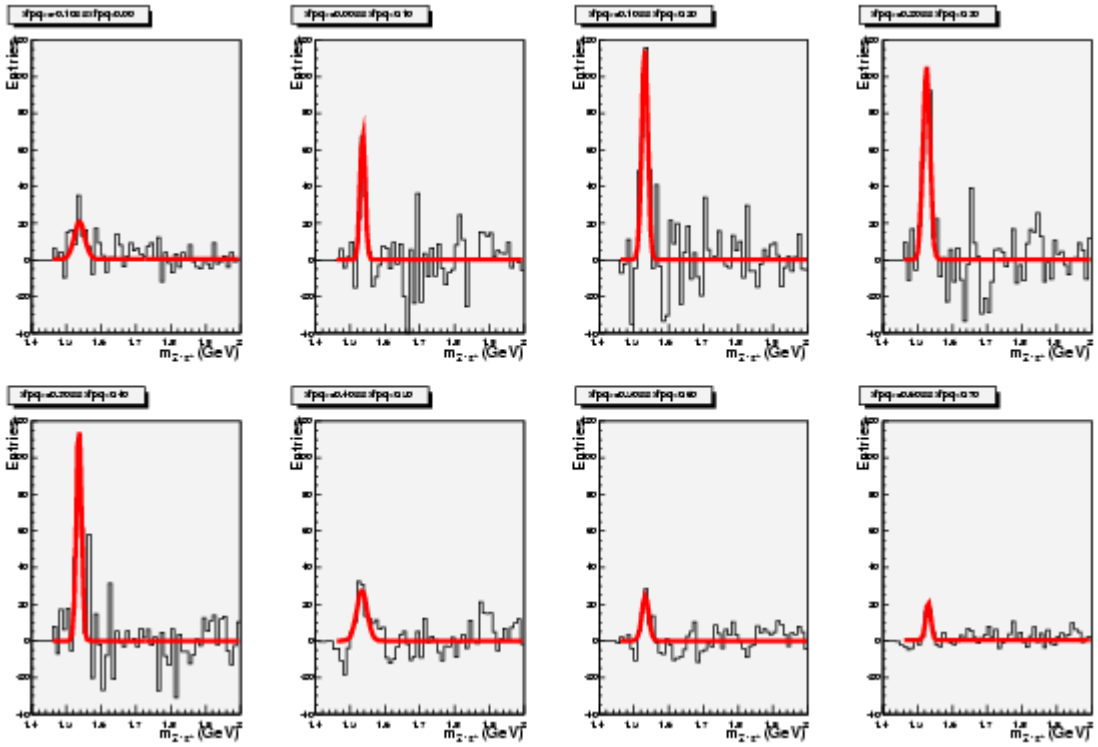

Figure 5.18: Ξ^{0*} invariant mass distributions in different intervals of x_F (from -0.1 to 0.7 in steps of 0.1). The distributions are fitted with a Gaussian plus a constant function.

In Fig. 5.17 the $\Xi^-\pi^+$ (black histograms) and the scaled $\Xi^-\pi^-$ (red histograms) invariant mass distributions in different intervals of x_F are shown. The two distribution are in good agreement, except for the Ξ^{0*} peak. By subtracting the two distributions ("$\Xi^-\pi^+$" $-$ "$\Xi^-\pi^-$") the plots in Fig. 5.18 are obtained. The Ξ^{0*} peak has been fitted with a Gaussian plus a constant function for each interval. The constant function is zero for all the plots, which confirm the validity of the multiplication factor f. The number of Ξ^{0*} (within 3σ) is plotted as function of x_F (Fig. 5.19). The sharp decrease for $x_F \simeq 0$ is due to the overall acceptance (of the spectrometer and the reconstruction) which reduces the efficiency for particles emitted at large angle, thus with small $p_{z\,cm}$ (Eq. 5.8).

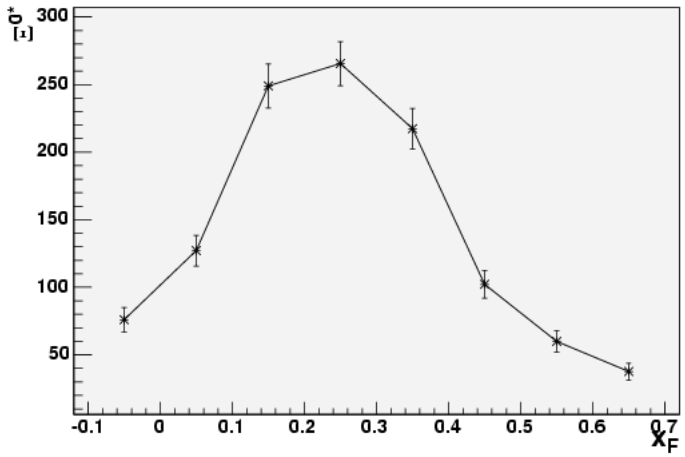

Figure 5.19: Number of reconstructed Ξ^{0*} as function of x_F.

To summarise, the analysis of the $\Xi^-\pi$ channel has not revealed any excess of events at the effective mass $m = 1862$ MeV, corresponding to the signal observed by the NA49. The same holds for different x_F intervals. The well known resonance Ξ^{0*} is clearly seen in the $\Xi^-\pi^+$ channel. The same is valid for the antiparticles.

5.2.7 Monte Carlo simulations

Monte Carlo simulations are a very powerful tool to understand the performance of the detectors. The simulations have to be compared with real data, in order to be sure they correctly describe the detector behaviour. Monte Carlo simulations have been used in this analysis to measure the reconstruction efficiency of Ξ^{0*} (as will be explained in the next section). In this section the Ξ^- and the Ξ^{0*} distributions from real data and Monte Carlo are compared, to verify the validity of the

simulations. The Monte Carlo data simulate the following decay chain:

$$\Xi^{0*} \rightarrow \Xi^{-}\pi^{+} \rightarrow \Lambda^{0}\pi^{-}\pi^{+} \rightarrow p\pi^{+}\pi^{-}\pi^{+}. \tag{5.9}$$

The left plot in Fig. 5.20 shows the $\Lambda^0\pi^-$ invariant mass spectrum from real data and simulations. The Monte Carlo histogram has been scaled to the data in order to have the same area, corresponding to the same number of events, under the two Gaussians from data and simulations. The widths of the Gaussian are very similar, but the background is sensitively different.

A useful quantity to check the validity of the simulations is the momentum distribution of the Ξ^-.

Under the peak, both Ξ^- and background events are present and they cannot be distinguished, but their separate contribution to the momentum distribution can be estimated using the method of *sideband substraction*: the invariant mass distribution is fitted with a Gaussian plus a linear function and the width of the distribution is calculated; the momentum of the particle is plotted for the events with mass at $\pm 3\sigma$ around the mean value of the Gaussian (gray shadowed area in the left plot of Fig. 5.20) and for the events in two regions of the invariant mass distribution aside the peak where only background is expected (yellow shadowed area in the left plot of Fig. 5.20). Subtracting the second histogram from the first one eliminates the contribution of the background events. The momentum distributions from real data and simulations are depicted in the right plot of Fig. 5.20, and they show a sufficient agreement on the qualitative level aimed here.

The same method has been used for the reconstruction of the Ξ^{0*} (Fig. 5.21). In this case, the combinatorial background is relevant also in case of simulated events and the sideband subtraction method has been applied to both momentum spectra. Since the peak of the Ξ^{0*} lies on the top of the phase space, only one background region has been used. Also in this case the two momentum distributions are in sufficient agreement. In Fig. 5.21 the positions of the Ξ^{0*} peak for real data and the Monte Carlo coincide, but the widths are significantly different. This is due to a inadequate estimation of the background function around the peak region. A better way to compare the invariant mass distribution is to use the same method described in Sec. 5.2.6, that is to use the $\Xi^-\pi^-$ spectrum to estimate the background of the $\Xi^-\pi^+$ invariant mass distribution. In this case the two histograms in Fig. 5.22 for real data and Monte Carlo are obtained. The Monte Carlo histogram is scaled to the data in order to have the same number of events under the peak. A full agreement between the two distribution is achieved.

From the width of the Ξ^{0*} distribution $\sigma = 9.4 \pm 1.3$ MeV it is possible to extract the resolution of the COMPASS spectrometer for Ξ^{0*} events. The total measured

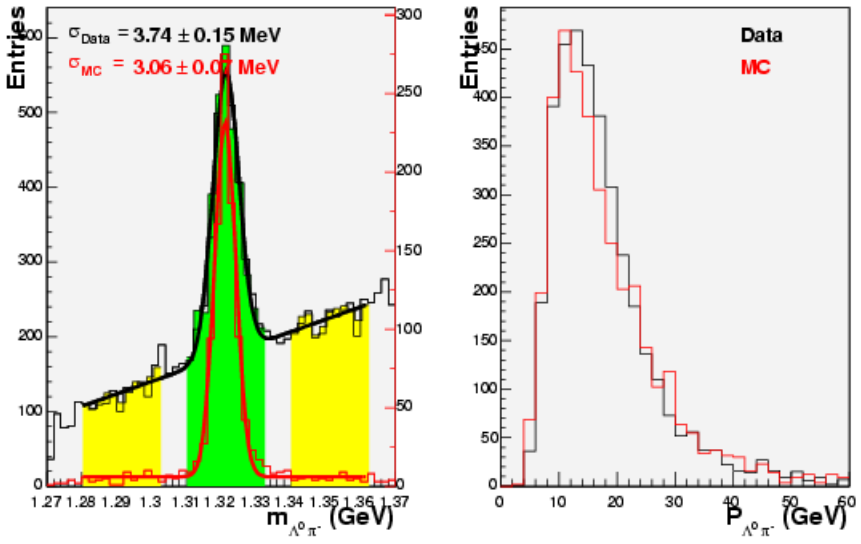

Figure 5.20: Right: $\Lambda^0\pi^-$ invariant mass spectrum from data (black histogram) and Monte Carlo (red histogram). The curves are the fit of a Gaussian plus a linear function. The shadowed areas show the regions used for the sideband subtraction of the momentum distribution (left plot). For explanation see text.

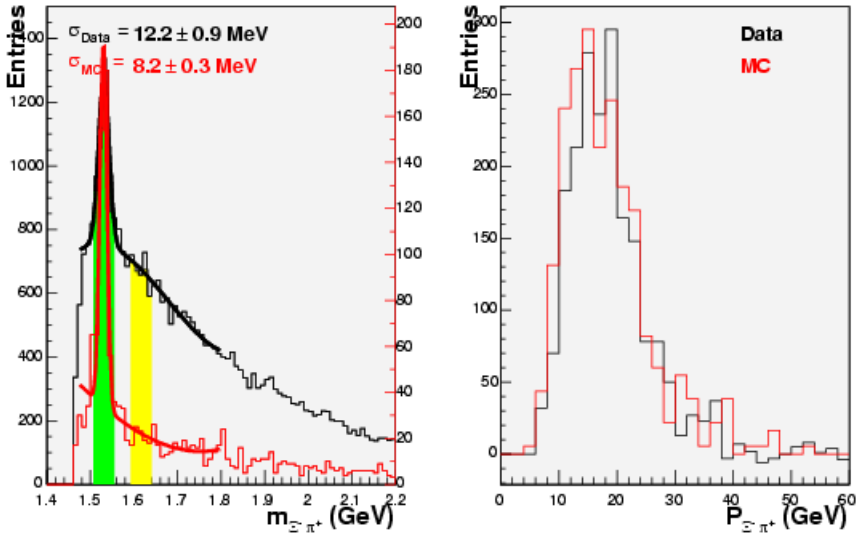

Figure 5.21: Right: same as Fig. 5.20, but here for $\Xi^-\pi^+$

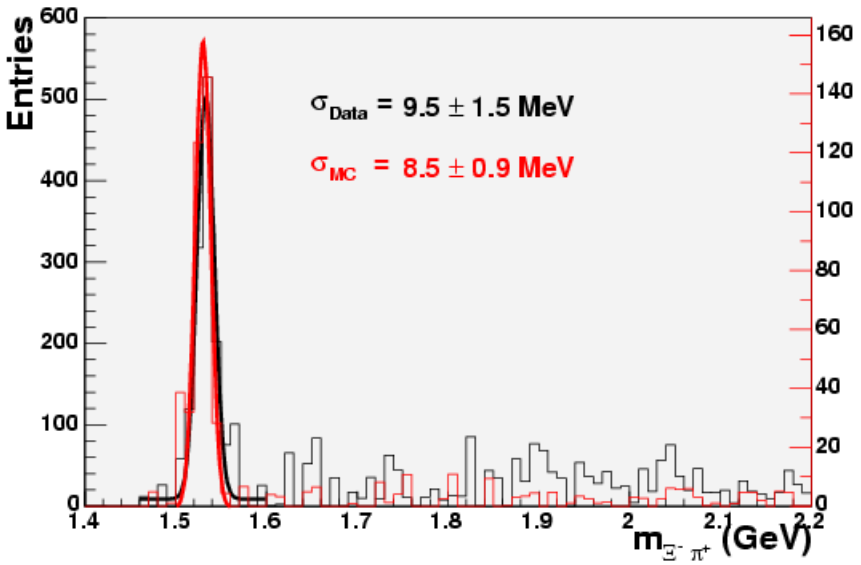

Figure 5.22: $\Xi^-\pi^+$ invariant mass spectrum from data (black histogram) and Monte Carlo (red histogram) with subtracted background. The curves are the fit of a Gaussian plus a constant function.

FWHM $\Gamma_{tot} \simeq 2.3 \cdot \sigma$ is the convolution of the natural line width of the particle Γ_p and of the detector resolution Γ_d.

$$\Gamma_{tot} = \sqrt{\Gamma_p^2 + \Gamma_d^2} \tag{5.10}$$

The width of the Ξ^{0*} is $\Gamma_p = 9.1 \pm 0.5$ MeV [PDG00a] and $\Gamma_{tot} = 22 \pm 3$ MeV. Then

$$\Gamma_d = \sqrt{\Gamma_{tot}^2 - \Gamma_p^2} = 20 \pm 2 \text{ MeV}. \tag{5.11}$$

and for the mass resolution $\sigma = 8.7 \pm 0.9$ MeV.

5.2.8 Ξ^{0*} reconstruction efficiency and production cross section

The reconstruction efficiency of a particle is the ratio between the number of reconstructed particles and the total number of particle and goes from 0 to 1. It is important to determine the production cross section. In this work the reconstruction efficiency for Ξ^{0*} in COMPASS has been estimated, using the Monte Carlo

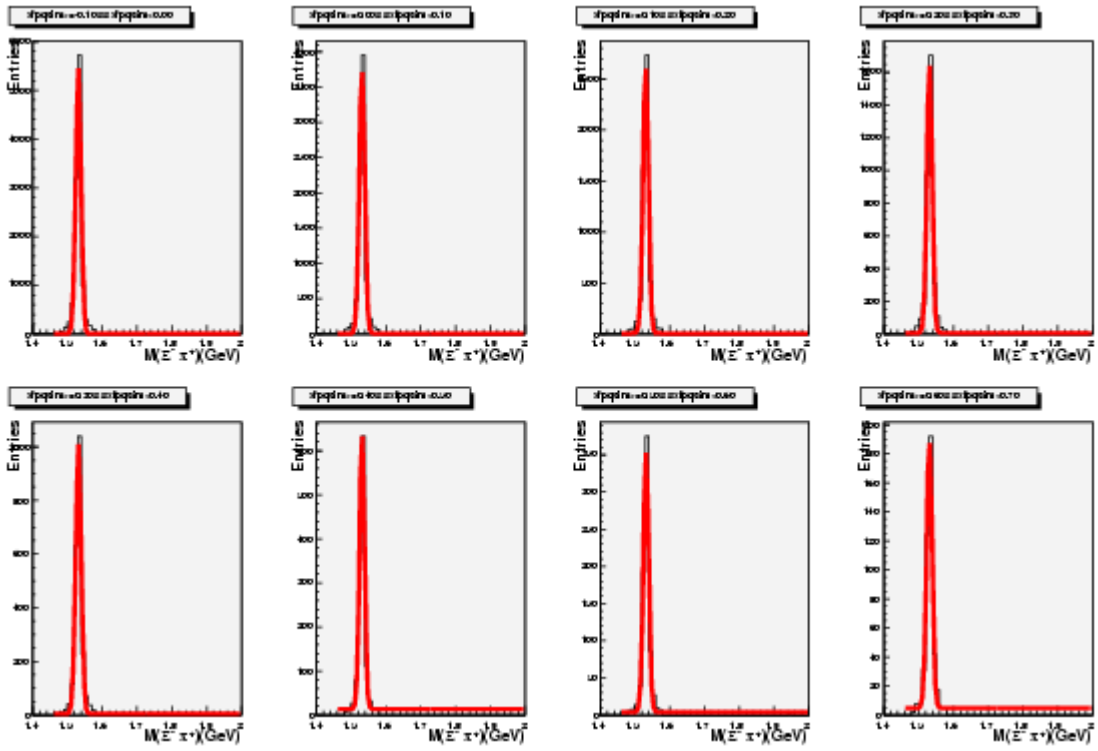

Figure 5.23: The Ξ^{0*} mass spectra in different x_F (from -0.1 to 0.7 in steps of 0.1) intervals of the Monte Carlo generated events.

simulations. The sample has been divided in 8 intervals of x_F (from -0.1 to 0.7 in steps of 0.1) and the efficiency in each interval of x_F has been estimated.

In Monte Carlo simulations each track has an identifier that specifies the type of particle. Therefore Ξ^{0*} can be unambiguously identified. The Ξ^{0*} spectra for different intervals of x_F are shown in Fig. 5.23. The spectra are fit using a Gaussian function and the number of events under the peak within 3σ is counted in each x_F interval . The $\Xi^-\pi^+$ invariant mass spectrum has been reconstructed. The background has been estimated with the help of the $\Xi^-\pi^-$ invariant mass distribution (see Sec. 5.2.6). The invariant mass distributions are shown in Fig. 5.24. The peak corresponding to the Ξ^{0*} is fitted with a Gaussian plus a constant function (red continuous line). The Ξ^{0*} under the peak within 3σ are counted.

The ratio between the number of reconstructed events and generated events has been calculated in each interval of x_F and plotted in Fig. 5.25. The small value of the efficiency for $x_F \sim 0$ is due to the acceptance of the spectrometer, causing a not optimal reconstruction for particles emitted at big angles respect to the beam direction . The points have been fitted with a polynomial function of order 3. This choice of the polinomial for the fit function does not have a theoretical

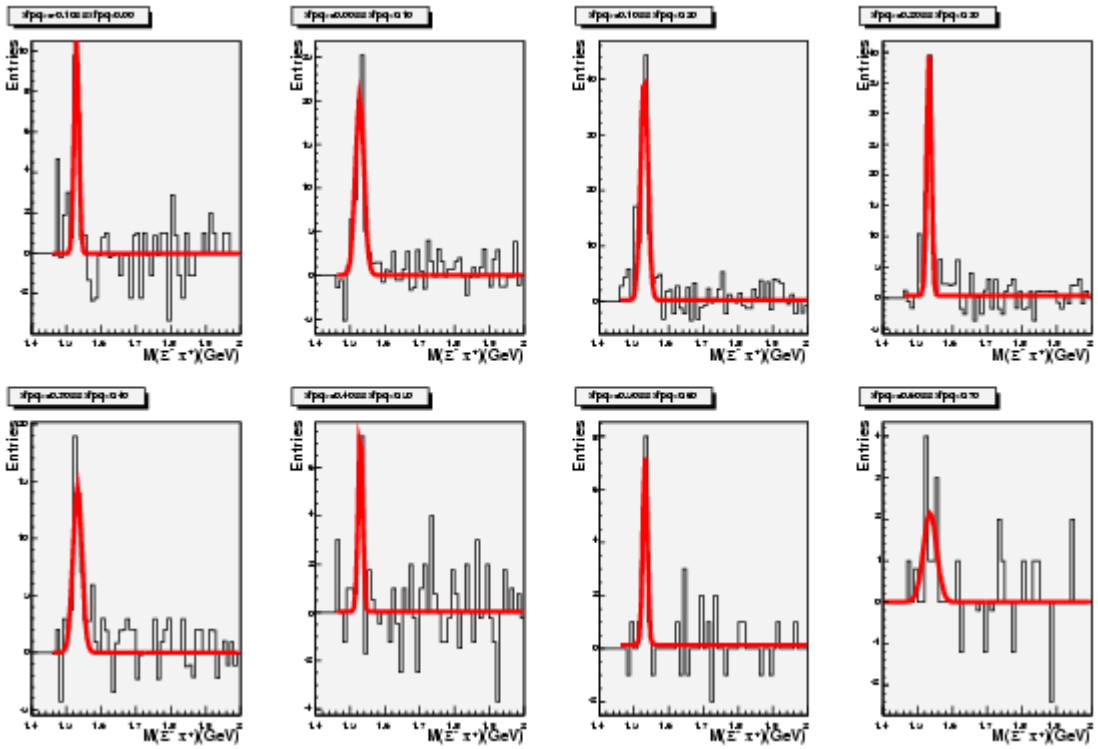

Figure 5.24: The $\Xi^-\pi^+$ invariant mass spectra in different intervals of x_F (from -0.1 to 0.7 in steps of 0.1) for reconstructed Monte Carlo data.

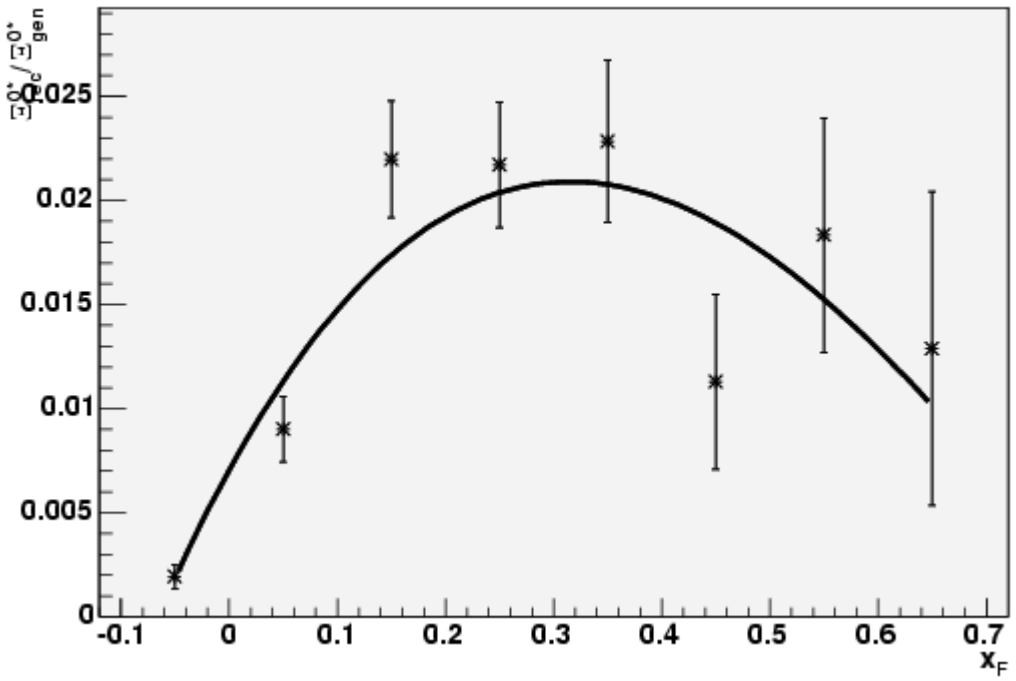

Figure 5.25: The Ξ^{0*} efficiency as function of x_F.

justification, but it is obviously sufficient to describe the x_F dependence within the statistical errors. Consequently, for further analysis the measured efficiency for the different values of x_F was used, instead of the interpolation from the fit function.

By knowing the efficiency of the Ξ^{0*} reconstruction, the production cross section of Ξ^{0*} produced in COMPASS in 2002 and 2003 as function of x_F can be calculated. The number of reconstructed Ξ^{0*} in each x_F interval (n_r, Fig. 5.19) has to be divided for the reconstruction efficiency η and the luminosity L. Since the Ξ^{0*} decays with 100% **B**ranching **R**atio (BR) in the channel $\Xi^-\pi^+$, the Ξ^- with 99.887% BR in the channel $\Lambda^0\pi^-$ and the Λ^0 with 63.9% BR in the channel $p\pi^-$ [PDG00a], these factors have to be included to estimate the production of the Ξ^{0*} without constraints on the decay channel.

Finally

$$\frac{d\sigma}{dx_F} = n_r/(\eta * 1 * 0.99887 * 0.639 * L * \Delta x_F) \tag{5.12}$$

Fig. 5.26 shows the cross section of Ξ^{0*} produced in COMPASS in the 2002 and

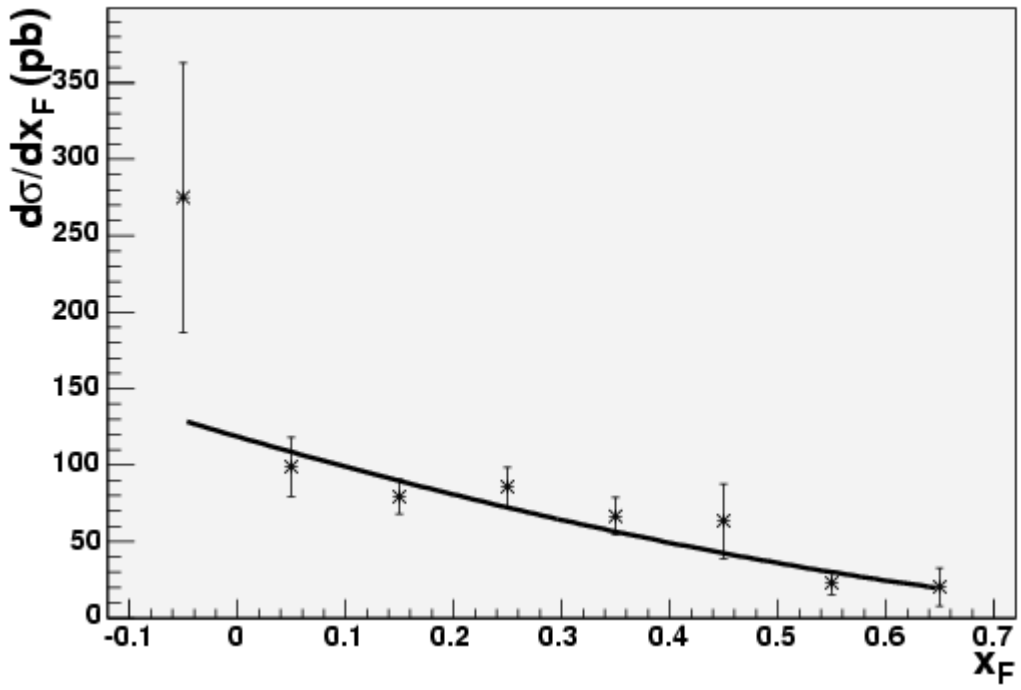

Figure 5.26: The number of Ξ^{0*} produced in COMPASS as function of x_F.

2003 as function of x_F. The points are fitted with the function $C(1-x_F)^{1.725}$ where C is a constant [Ada99].

The integrated cross section for the production of Ξ^{0*}, σ, with x_F from -0.1 to 0.7 is obtained by summing the bins:

$$\sigma = \sum \frac{d\sigma}{dx_F} \Delta x_F = 71 \text{ pb}. \tag{5.13}$$

5.2.9 An upper limit for the Ξ^{--} production cross section

In order to determine the upper limit for the production cross section of the Ξ^{--} in COMPASS, the same method used for the WA89 data has been applied [wa804]. The $\Xi^-\pi^-$ invariant mass distribution has been divided in 8 bins of x_F from -0.1 to 0.7 (Fig. 5.27). Based on the claimed experimental width of the Ξ^{--}, $\Gamma < 17$ MeV FWHM [na403], three regions with width 20 MeV around 1.852, 1.862 and 1.872 GeV have been selected (green shaded area). The number of events in each region is $n_i (i = 1, 2, 3)$. From a fit to the $\Xi^-\pi^-$ invariant mass spectrum in the region $1.55 - 2.6$ GeV, excluding the signal region (continuous

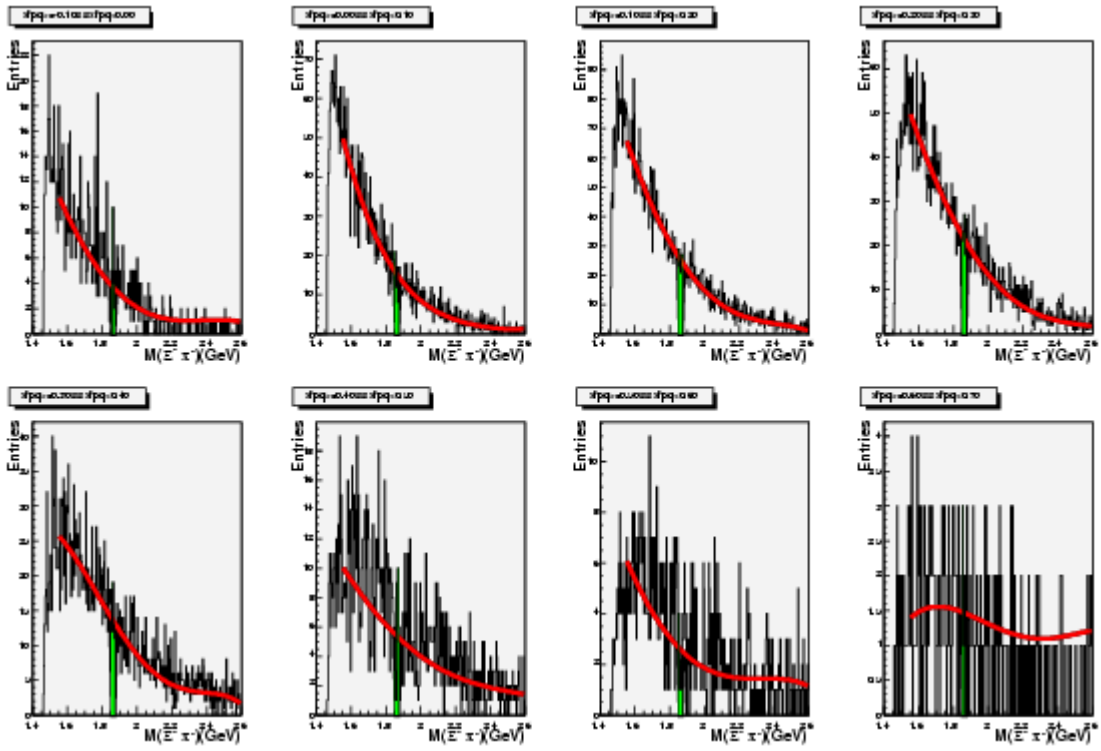

Figure 5.27: The $\Xi^-\pi^-$ Invariant mass spectra in different x_F intervals (from -0.1 to 0.7 in steps of 0.1).

red line), the expected background per each bin $b_i (i = 1, 2, 3)$ has been calculated. The 3σ limit n_{max} for the number of events in an hypotetical peak over the background in each x_F interval is:

$$n_{max} = max_{i=1,2,3}(max(0, n_i - b_i) + 3\sqrt{b_i}) \tag{5.14}$$

and are listed in the second column of Tab. 5.7.

From these numbers the upper limit of the Ξ^{--} differential production cross section $d\sigma/dx_F$ (weighted with the eventual branching ratio $BR(\Xi^{--} \to \Xi^-\pi^-)$)has been calculated. The formula is

$$BR(\Xi^{--} \to \Xi^-\pi^-) \cdot d\sigma/dx_F = \frac{n_{max}}{L\eta BR(\Lambda^0 \to p\pi^-)BR(\Xi^- \to \Lambda^0\pi^-)\,\Delta x_F} \tag{5.15}$$

where $L = 2240\ pb^{-1}$ is the luminosity, η the reconstruction efficiency, $BR(\Lambda^0 \to p\pi^-) = 0.639$ and $BR(\Xi^- \to \Lambda^0\pi^-) = 0.999$ the decay branching ratios. Since

Monte Carlo simulations for a resonance with the characteristics of Ξ^{--} propagated in the COMPASS spectrometer are presently not available, the efficiency measured for the Ξ^{0*} has been used (Sec. 5.2.8). However, no significant difference is expected, since the Ξ^{0*} and the Ξ^{--} have a similar decay channel.

The results are listed in the third column of Tab. 5.7.

x_F	n_{max}	$\Delta x_F \cdot BR \cdot d\sigma/dx_F$[pb]
-0.1−0.0	17	6.08
0.0−0.1	30	2.31
0.1−0.2	34	1.10
0.2−0.3	43	1.40
0.3−0.4	38	1.18
0.4−0.5	20	1.25
0.5−0.6	13	0.50
0.6−0.7	9	0.48

Table 5.7: number of events n_{max} in 3σ and the corresponding limits on the differential cross section for Ξ^{--} production for different x_F intervals.

The limit for the integrated production cross section has been calculated by summing quadratically the contributions $\Delta x_F \cdot BR \cdot d\sigma/dx_F$. The result is $BR\sigma_{max} \leq 7$ pb in the $\Xi^{--}(1860) \rightarrow \Xi^-\pi^-$ decay channel with x_F from -0.1 to 0.7.

5.2.10 $\Xi^{0*}\pi$ selection

This last study followed the preliminary analysis done by NA49 in the channel $\Xi^{0*}\pi$ where a signal at a mass 1855 MeV in the invariant mass spectrum was observed [KA04].

Ξ^{0*} candidates with mass $|m_{\Xi^{0*}} - m^{PDG}_{\Xi^{0*}}| \leq 2 \cdot \sigma = 0.017$ GeV are selected for further analysis; σ is calculated from the $m_{\Xi^{0*}}$ distribution (Fig.5.2.6).

An additional particle fulfilling the following requirements is then requested:

- the particle has not been used for Ξ^{0*}, Λ^0 and Ξ^- reconstruction;
- the track is connected to the primary vertex, since the searched resonances decay immediately after production;

The pion mass is attributed to this particle. The Ξ^{0*} is then matched with a positive or negative pion. The same matching is done for the antiparticles $\overline{\Xi^{0*}}$. In

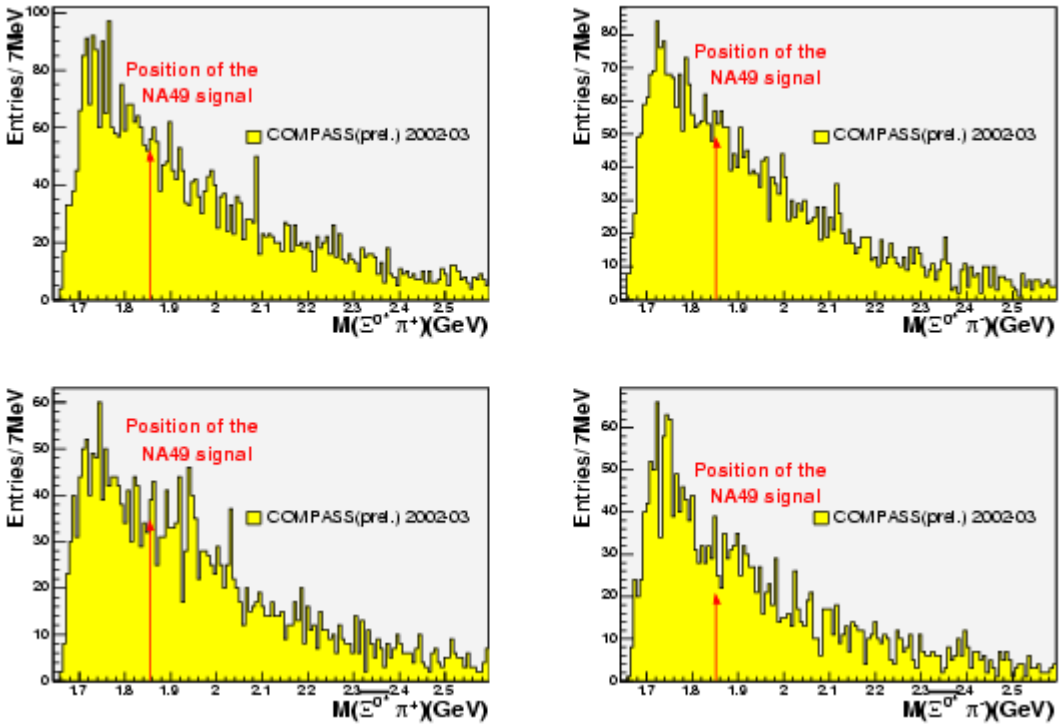

Figure 5.28: $\Xi^{0*}\pi^{+}$ (top left), $\overline{\Xi^{0*}}\pi^{+}$ (bottom left), $\Xi^{0*}\pi^{-}$ (top right), $\overline{\Xi^{0*}}\pi^{-}$ (bottom right) invariant mass spectra.

Fig.5.28 the invariant mass spectra of these four states are presented. No significant signal at $m = 1855$ MeV is observed. Applying the same method discussed in Sec. 5.2.9 the upper limit for the number of events has been calculated. For the $\Xi^{0*}\pi^-$ combination:

$$n_{\max} = max_{\mathrm{i}=1,2,3}(max(0, n_{\mathrm{i}} - b_{\mathrm{i}}) + 3\sqrt{b_{\mathrm{i}}}) = 56 \tag{5.16}$$

Since no Monte Carlo simulations are presenty available for this study, the upper limit for the cross section has not been calculated.

5.2.11 Discussion of the results

Reconstruction of Ξ^{0*}

With the study of Ξ^{0*}, COMPASS can contribute to clarify its production mechanism and properties in $\gamma^* N$ interactions.

About 1000 Ξ^{0*} (Tab. 5.5) have been reconstructed from the 2002 and 2003 COMPASS data. Using Monte Carlo simulated data, the cross section for Ξ^{0*} production as function of x_{F}, $\frac{\mathrm{d}\sigma}{\mathrm{d}x_{\mathrm{F}}}$, in the range [-0.1; 0.7] has been measured (Fig. 5.26) and $\frac{\mathrm{d}\sigma}{\mathrm{d}x_{\mathrm{F}}} \propto (1 - x_{\mathrm{F}})^{1.725}$. The integrated cross section for x_{F} in the range $[-0.1; 0.7]$ has been calculated and it is $\sigma = 71$ pb.

It is interesting to compare these results with other experiments, in order to better understand how Ξ^{0*} are produced.

There are no studies for the production cross section of Ξ^{0*} in photo-production experiments, while it is studied in hadro-production. For comparison, the results of the WA89 experiment are presented here [Ada99].

WA89 measured the $\sigma_{\Xi^{0*}}$ in $\Sigma^- N$ reactions with $0 < x_{\mathrm{F}} < 1$. The $\frac{\mathrm{d}\sigma}{\mathrm{d}x_{\mathrm{F}}}$ behaves like $C(1 - x_{\mathrm{F}})^{1.265}$. The differential cross section in WA89 goes less rapidly to zero for $x_{\mathrm{F}} \to 1$ than in COMPASS. This is due to the fact that WA89 uses Σ^- as beam particle, that contains already a strange quark: if the Ξ^{0*} is formed in the current fragmentation region ($x_{\mathrm{F}} \sim 1$), only one additional strange quark has to be created to form the Ξ^{0*}. This phenomenon is called *leading particle effect*. COMPASS, instead, uses muons as beam particles and the strange quarks in the Ξ^{0*} has to be formed out of the quark sea, making the process in current fragmentation region less probable.

One can also compare the integrated cross section: WA89 measured $\sigma_{\Sigma^- N \to \Xi^{0*} X} = 218\ \mu$b for $0 < x_{\mathrm{F}} < 1$. From the plots in [wa804] it was extracted the value

$\sigma_{\Sigma^- N \to \Xi^{0*} X} \sim 170$ μb in the region $0 < x_F < 0.7$ to be compared with the COMPASS value $\sigma_{\mu N \to \Xi^{0*} X} = 44$ pb for the same x_F region; they differ by about six orders of magnitude. Two points can clarify this difference: the first one is the mentioned leading particle effect, which predicts a higher production rate of strange particles in the current fragmentation region if the beam particle contains already a strange quark. The second and most significant one is the type of interaction. For the cross section $\sigma \propto \alpha^2$ where α is the coupling constant of the interaction. The $\gamma^* N$ interaction is electromagnetic and $\alpha = 1/137$, while the $\Sigma^- N$ interaction is strong and $\alpha = \alpha_s \sim 1$ for the considered energy. This means that the cross section σ_Ξ for a Σ beam is $\sim 10^4$ higher then for a photon beam. The results for WA89 and COMPASS are summarised in Tab. 5.8.

Experiment	Reaction	n	$\sigma_{\Xi^{0*}}$	production
COMPASS	$\gamma^* N$	1.725	44 pb	photo-production
WA89	$\Sigma^- N$	1.265	170 μb	hadro-production

Table 5.8: Comparison between COMPASS and WA89 experiments in the Ξ^{0*} reconstruction. n is the exponent of the $C(1 - x_F)^n$ which was used to fit the $\frac{d\sigma}{dx_F}$ distribution.

To summarise, it is not possible to quantitavely compare the Ξ^{0*} production cross section in COMPASS and WA89 due to their different production mechanisms. However, it has been shown that they are qualitatively consistent.

Reconstruction of Ξ^{--}

The search for a manifestly exotic pentaquark candidate, Ξ^{--}, follows the results of the NA49 experiment which claimed a signal in the decay channel $\Xi^{--} \to \Xi^- \pi^- \to \Lambda^0 \pi^- \pi^- \to p \pi^- \pi^- \pi^-$ at a mass $m = 1862$ MeV in pp interactions [na403]. The invariant mass spectra for $\Xi^- \pi^-$, $\Xi^- \pi^+$ and their charge conjugate are shown in Fig. 5.29.

The analysis of the same decay chain in the 2002 and 2003 COMPASS data does not show any peak structure in the $\Xi^- \pi^-$ channel, and in any of the charge conjugate channels, as it can be observed in Fig. 5.30. The same analysis in different intervals of x_F in the range $-0.1 < x_F < 0.7$ did also show non-confirmative results. Moreover, an upper limit of the production cross section has been calculated, $BR(\Xi^{--} \to \Xi^- \pi^-) \cdot \sigma_{max} \leq 7$ pb.

NA49 observed the Ξ^{--} candidate in hadro-production, however there is no fundamental reason why the Ξ^{--} should not be observed in photo-production. It is

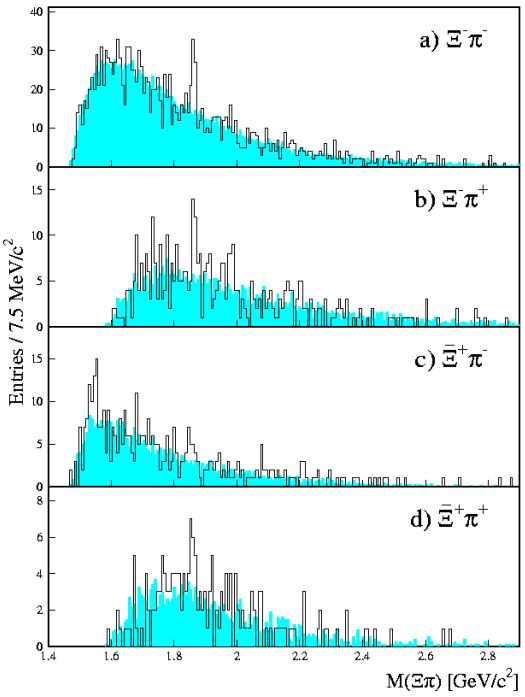

Figure 5.29: Invariant mass spectra for $\Xi^-\pi^-$, $\Xi^-\pi^+$, $\bar{\Xi}^+\pi^-$ and $\bar{\Xi}^+\pi^+$ as observed by the NA49 experiment.

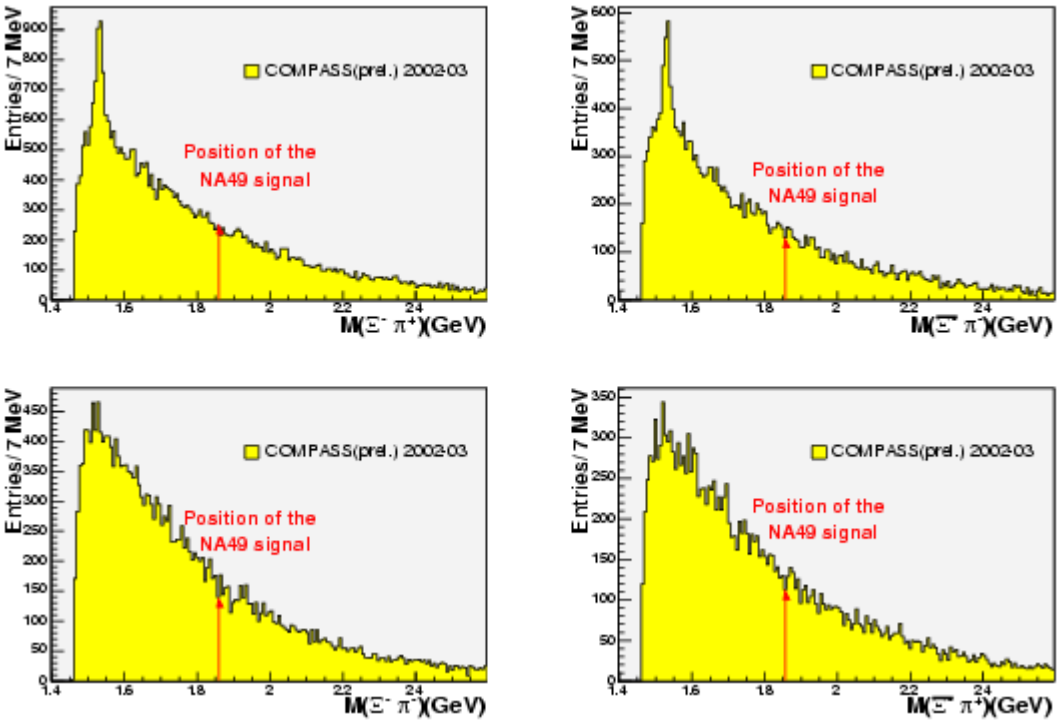

Figure 5.30: $\Xi^-\pi^+$ (top left), $\overline{\Xi^-}\pi^-$ (bottom left), $\Xi^-\pi^-$ (top right), $\overline{\Xi^-}\pi^+$ (bottom right) invariant mass spectra.

worthwhile to remark that also the WA89 [wa804] and HERA-B [HER04] experiments have investigated the $\Xi^{--} \rightarrow \Xi^{-}\pi^{-}$ channel with negative results. The main characteristics of these experiments are listed in Tab. 5.9.

Experiment	Reaction	$\sqrt{s}$ (GeV)	production	Ξ^{--} observation
NA49	pp	17.2	hadro-production	yes
COMPASS	$\gamma^{*}N$	~ 18	photo-production	no
WA89	$\Sigma^{-}N$	~ 26	hadro-production	no
HERA-B	pN	41.6	hadro-production	no

Table 5.9: Comparison between different experiments who searched for the Ξ^{--} pentaquark candidate.

With this in mind, one can make some quantitative comparison between the results of NA49 and COMPASS. NA49 observed ~ 36 events over the background at $m \sim 1862$ GeV [na403] in the $\Xi^{-}\pi^{-}$ channel and 1640 Ξ^{-}, then $\Xi^{--}/\Xi^{-} = 36/1640 = 0.022$. In the present analysis 17930 Ξ^{-} events were reconstructed. Assuming the same relative production rate Ξ^{--}/Ξ^{-}, from the pure comparison of the number of events, COMPASS should then observe $17930 \cdot 0.022 \sim 394$ Ξ^{--} events (see Tab. 5.4). The statistical significance of the COMPASS results is that a peak at 1862 MeV with more than 45 events can be excluded with 2σ C.L.. This means that the non observation of an expected signal of 364 events cannot be due to statistical fluctuations well above 95% C.L.. Other reasons have to found to explain this peculiar behaviour of the claimed Ξ^{--} pentaquark candidate.

To conclude, the status of the Ξ^{--} search is presently puzzling. Several experiments did not confirm the observation of NA49 in photo- and hadro-production. If other high statistics experiments would confirm the NA49 observation, the results achieved in this analysis with COMPASS data may point to an exotic production dynamics of this hypothesised pentaquark.

Conclusions and Outlook

This work was done in the framework of the COMPASS experiment.

In the first part, the design and the realisation of a silicon microstrip detector system operated at cryogenic temperature has been discussed. Silicon detectors are used in COMPASS for the reconstruction of beam particle upstream of the target. To prevent the degradation of the detector's performances due to high radiation doses to which they are exposed, they are operated at cryogenic temperature. This feature is called *Lazarus effect* and consists in the recovery of the **C**harge **C**ollection **E**fficiency (*CCE*) of heavily damaged silicon detectors when operated at cryogenic temperature, with a maximum of the CCE at $T \sim 130$ K. The COMPASS silicon detectors can be used for the entire lifetime of the experiment if operated at cryogenic temperatures. In order to operate a silicon detector at cryogenic temperatures, a cooling system has been designed. It consist of a tiny (1.3 mm inner diameter) tube in thermal contact with the detector, in which liquid nitrogen fluxes. The temperature at the detector can be variated by changing the nitrogen flux in the tube. The termal insulation of the detector from the outer environment is achieved operating it inside an evacuated cryostat. The cryostat has been designed with a small radiation length in the beam direction, to minimise its interference with the beam particles. Cooling the silicon detector implies that its mechanical support, which contains also the first component of the readout chain, is cooled as well. The glues used in this area have proved to mantain their property at low temperatures. The readout chip APV25, which is located close to detector, has not shown any dramatic change of its features, in spite of not being designed for low temperature operation.

During 2003 two silicon detectors operated at 130 K were succesfully installed in the COMPASS experiment. Nevertheless a stable operation could be achieved only for few days, due to discontinuous method of providing the liquid nitrogen with a self-pressurised dewar. A more sophisticated distribution system for liquid nitrogen, which can provide the coolant without any interruption to several detectors, has been designed and tested and will be installed in the near future in COMPASS.

The second part of this work has been devoted to the search of the manifestly exotic pentaquark called Ξ^{--} with mass $m = 1862$ MeV using the 2002 and 2003 COMPASS data. A hint for a Ξ^{--} signal had been given by the NA49 experiment in the decay channel $\Xi^{--} \rightarrow \Xi^{-}\pi^{-} \rightarrow \Lambda^{0}\pi^{-}\pi^{-} \rightarrow p\pi^{-}\pi^{-}\pi^{-}$. NA49 claimed the Ξ^{--} in hadro-production, instead COMPASS provides data in photo-production. The only other pentaquark candidate Θ^{+} has been observed in both hadro- and photo-production experiments, with preference to the latter one, and there is no theoretical reason for a different mechanism production for the Ξ^{--}.

Furthermore the production of the strange particle Ξ^{0*} has been studied. The selected decay channel is $\Xi^{0*} \rightarrow \Xi^{-}\pi^{+} \rightarrow \Lambda^{0}\pi^{-}\pi^{+} \rightarrow p\pi^{-}\pi^{-}\pi^{+}$. Since the decay channels for Ξ^{0*} and Ξ^{--} are similar, their study has be done done in parallel.

At first, a reconstruction method for Λ^{0}, Ξ^{-} and Ξ^{0*} has been developped, leading to a good signal over background for all three particles. Then the production characteristics of the Ξ^{0*} has been studied. For this particle the reconstruction efficiency has been evaluated using Monte Carlo simulation. The production cross section as function of x_{F} ($\mathrm{d}\sigma_{\mu N \rightarrow \Xi^{0*} X}/\mathrm{d}x_{\mathrm{F}}$) has been measured for x_{F} in the range $[-0.1; 0.7]$. A strong enhancement in the number of produced Ξ^{0*} can be observed for negative value of x_{F}, which points to a dominant contribution of Ξ^{0*} from the target fragmentation region. The integrated production cross section σ has been calculated $\sigma = 71$ pb^{-1}.

The same analysis method has been applied to search for the Ξ^{--}. The $\Xi^{-}\pi^{-}$ invariant mass spectrum does not exhibit any visible excess of events at $m \sim 1862$ MeV in any interval of x_{F}. It is worthwhile to mention that other experiments [wa804] [HER04] have analysed the $\Xi^{-}\pi^{-}$ invariant mass spectrum in hadro-production and none of them could confirm the findings of NA49. The Ξ^{0*} efficiency has been taken as estimate to calculate the upper limit of the production cross section for Ξ^{--}. The result is $BR(\Xi^{--} \rightarrow \Xi^{-}\pi^{-})\sigma_{\mathrm{max}} \leq 7$ pb.

In order to confirm or refuse the existence of a Ξ^{--} pentaquark, more measurements are needed. While experiments with high energy hadron beams have obtained results which are difficult to improve, one might envisage the use of low energy beams (γ or kaons) to search for Ξ^{--}. As such experiments are planned for Θ^{+}, their outcome will have strong influence on the future measurement plans. In case of a positive and conclusive observation, it is also envisageable to measure the width, the spin and the parity of such a state, in order to have a better understanding of exotics production and, more in general, of the QCD.

Bibliography

[Abt96] I. Abt et al. Irradiation Tests of Double-Sided Silicon Strip Detectors with a Special Guard Ring Structure. *IEEE Trans. Nucl. Sci* **43**, 1113–1118 (1996).

[Abt98] I. Abt et al. Gluing Silicon with Silicone. *Nucl. Instr. and Meth. in Phys. Res. A* **411**, 191–196 (1998).

[Abt99] I. Abt et al. Double sided microstrip detectors for the high radiation environment in the HERA-B experiment. *MPI-PhE* **99-05** (1999).

[Ada99] M. I. Adamovich et al. Production of Ξ^* resonances in Σ^- induced reactions at 345 GeV/c. *Eur. Phys. J.* **C 11**, 271–278 (1999).

[Ber97] SINTEF Electronics & Cybernetics, R. W. Bernstein, and T. Westgaard. Technical Specifications and Test Specifications for MPI HERA-B Double-sided Silicon (1997).

[Bic72] H. Bichsel. *Passage of charged particles through matter*. Mcgraw-Hill, 3nd edition, 1972.

[Bij] E. van der Bij. http://hsi.web.cern.ch/HSI/s-link/.

[Bro] Bronkhorst: High-Tech B.V. Thermal Mass Flow Meters and Controllers for Gases: Instruction Manual.

[CAS] http://castor.web.cern.ch/castor/Welcome.html .

[Cas01] L. Casagrande et al. Review on the development of cryogenic silicon detectors. *Nucl. Instrum. Meth.* **A461**, 150–154 (2001).

[CLA03] S. Stepanyan et al. hep-ph/0307018 (2003).

[CM84] P. D. B. Collins and A. D. Martin. *Hadron Interactions*. Hilger, 2nd edition, 1984.

[COM] http://wwwcompass.cern.ch/

[COM96] The COMPASS collaboration. A proposal for a Common Muon and Proton Apparatus for Structure and Spectroscopy. *CERN* **SPSLC 96-14** (1996).

[DIA03] V. V. Barmin et al. hep-ph/0304040 (2003).

[DVC] N. d'Hose. Feasibility Study of Deeply Virtual Compton Scattering using COMPASS at CERN. In preparation.

[Ehl02] J. Ehlers. *Performance of the Triple GEM Detectors in the COMPASS Experiment*. Diploma thesis, Universität Heidelberg, September 2002.

[ELMa] http://atlas.web.cern.ch/Atlas/GROUPS/DAQTRIG/DCS/LMB/SB/index.html

[ELMb] http://pccosrv1.cern.ch/compass/detector/dcs/elmb.html

[EMC88] The European Muon Collaboration. A measurement of the spin asymmetry and determination of the structure function g(1) in deep inelastic muon - proton scattering. *Nucl. Phys.* **B 206 364** (1988).

[Erl95] J. Erler and P. Langacker. Implications of high precision experiments and the CDF top quark candidates. *Phys. Rev.* **D52**, 441–450 (1995).

[Fau04] P. Fauland. *The COMPASS Experiment and the RICH-1 Detector*. Phd thesis, Universität Bielefeld, March 2004.

[Fuc04] A. Fuchs. *Setup for a low temperature silicon detector for the COMPASS Experiment*. Diploma thesis, TU München, January 2004.

[GLA64] C.J. Glassbrenner and G.A. Slack. Thermal Conductivity of Silicon and Germanium from 3K to the Melting Point. *Phys. Rev.* **4A134**, 1058–1069 (1964).

[GPD02] Michel Garcon. An introduction to the generalized parton distributions. hep-ph/0210068 (2002).

[gra01] V.Granata et al. Cryogenic Technology for Tracking detectors. *NIM A, 461 197-199* (2001).

[Gru01] B. Grube. *The trigger control system and the common GEM and Silicon read out for the COMPASS experiment*. Diploma thesis, TU München, December 2001.

[h1] P. Pagano et al. Preliminary Measurements of Transversity in COMPASS. In preparation.

[H104] A. Aktas et al. Evidence for a narrow anti-charmed baryon state. hep-ph/0403017 (2004).

[HER98] A. Airapetian et al. Measurement of the proton spin structure function g1(p) with a pure hydrogen target. *Phys. Lett.* **B442**, 484–492 (1998).

[HER03] A. Airapetian et al. hep-ph/0312044 (2003).

[HER04] K. T. Knoepfle et al. Search for Θ^+ $\Xi^{--}_{3/2}$ pentaquarks in HERA-B. hep-ph/0403020 (2004).

[Ilg03] Ch. Ilgner. *Fertigung und Inbetriebnahme einer Strohdriftkammerstation fr das COMPASS-Experiment*. Phd thesis, Ludwig-Maximilians-Universitt Mnchen, March 2003.

[jaf04] R. L. Jaffe. Exotica. hep-ph/0409065 (2004).

[KA04] M. Karliner. http://gate.hep.anl.gov/berger/Aspen04/Prog04/Karliner.pdf

[Kuh01] R. Kuhn. *Simulations for the Measurement of the Polarizabilities of the Pion at COMPASS*. Diploma thesis, TU München, November 2001.

[Kuh02] P. Pagano. *Preliminary measurement of Transversity at COMPASS experiment*. Phd thesis, Trieste, November 2002.

[Lam04] A. Ferrero et al. Λ^0 and $\overline{\Lambda^0}$ polarization at COMPASS. *XLII International Winter Meeting on Nuclear Physics* February 2004.

[Laz] V.Eremin et al. In preparation.

[Laz98] V.Palmieri et al. Evidence for charge collection efficiency recovery in heavily irradiated silicon detectors operated at cryogenic temperatures. *Nucl. Instr. and Meth. in Phys. Res. A* **413**, 475–478 (1998).

[Leb02] M. Leberig. *Das COMPASS-Triggersystem zur Messung des Gluonbeitrags zum Protonspin*. Phd thesis, Johannes Gutenberg-Universität Mainz, 2002.

[Leo94] W. R. Leo. *Techniques for Nuclear and Particle Physics Experiments*. Springer, 2nd edition, 1994.

[LEP03] T. Nakano et al. *Phys. Rev. Lett.* **91**, 012002 (2003).

[Les75] A. Lesnick et al. Observation of a difference between polarization and analyzing power in Λ^0 production with 6 GeV/c polarized protons. *Phys. Rev. Lett.* **35**, 770 (1975).

[M2] http://sl.web.cern.ch/SL/eagroup/NewM2/main.html

[Mal96] G. Mallot. *The Spin Structure of the Nucleon from the SMC Experiments*. Habilitationsschrift, Johannes Gutenberg-Universitt, August 1996.

[MM] G. Puill et al. Development of MICROMEGAS, a novel position sensitive gas detector with micromesh (In French). DAPNIA-SED-00-01-T.

[Moi02] M. A. Moinester et al. First observation of doubly charmed baryons. hep-ex/0212029 (2002).

[Mol99] M. Moll. *Radiation Damage in Silicon Particle Detectors - microscopic defects and macroscopic properties*. PhD thesis, Universität Hamburg, 1999.

[na403] C. Alt et al. Observattion of an Exotic S=-2, Q=-2 Baryon Resonance in Proton-Proton Collisions at CERN SPS. *Phys. Rev. Lett.* **92-042003**, 441–450 (2003).

[NA5] NA50 collaboration. http://na50.web.cern.ch/NA50/

[Nag05] T. Nagel. Diploma thesis, TU München, 2005. In preparation.

[NBW] http://www-physics.lbl.gov/s̃pieler/Heidelberg_Notes/pdf/III_Electronic_Noise.pdf

[OC04] C. Bernet et al. The Gluon Polarization $\frac{\Delta G}{G}$ at COMPASS. *XXXIXth Rencontres de Moriond: QCD and High Energy Hadronic Interactions* March 2004.

[PDG00a] D. E. Groom et al. Review of particle physics. *Eur. Phys. J.* **C 15** (2000).

[PDG00b] G. P. Yost et al. Review of particle physics. *Phys. Lett.* **B 204**, 1 (2000).

[Pei92] A. Peisert. Silicon Microstrip Detectors. *DELPHI* **92-143 MVX 2** (1992).

[PER75] M.L. Perl et al. *Phys. Rev. Lett.* **35**, 1489 (1975).

[Per82] D. H. Perkins. *Introduction to High Energy Physics*. Addison-Wesley, 2nd edition, 1982.

[PHA] http://ges.home.cern.ch/ges/phast/

[Pol97] V. Petrov D. Diakonov and M. V. Polyakov. Exotic anti-decuplet of baryons: Prediction from chiral solitons. *Z. Phys.* **A359**, 305–314 (1997).

[pol02] M. Moinester et al. Pion polarizabilities at CERN COMPASS. hep-ex/0206038 (2002).

[Ray01] M.Raymond et al. The APV25 0.25μm CMOS Read Out Chip for the CMS Tracker. (2001).

[RD39] RD39 collaboration. Radiation Hard Position Sensitive Cryogenic Silicon Detectors: The Lazarus effect. . PhysicaB.

[RD39w] RD39 collaboration. http://www.cern.rd39/

[ROSE] RD48 collaboration (*ROSE*). http://rd48.web.cern.ch/

[Rug99] G. Ruggiero. *Resistenza alla radiazione di rivelatori al silicio operanti a temperature criogeniche*. Diploma thesis, Universita' degli studi di Napoli, 1999.

[SAP03] J. Barth et al. hep-ph/0307083 (2003).

[Sau97] F. Sauli. GEM: A new concept for electron amplification in gas detectors. *Nucl. Inst. Methods* **A386**, 531–534 (1997).

[Sch03] L.Schmitt et al. The DAQ of the COMPASS experiment. *13th IEEE Reak Time Conference, Montreal* (2003).

[See04] D. Seeharsch. *A Microcontroller based Steering Mechanism for the COMPASS Silicon Detector Cooling System*. Diploma thesis, TU München, 2004.

[SHP] R. Kuhn. private comunication.

[SMC99] G. Abril et al. Spin dependent structure function g1: Recent experimental results. *Nucl. Phys. Proc. Suppl.* **71**, 100–108 (1999).

[Tak03] N. Takabayashi. *Polarized target for the measurement of the gluon contribution to the nucleon spin in the COMPASS experiment*. Phd thesis, Nagoya, March 2003.

[TOTEM] TOTEM collaboration. http://totem.web.cern.ch/Totem/

[wa804] M. I. Adamovich et al. Search for the exotic Ξ^{--} Resonance in 340 GeV/c Σ^--Nucleus Interaction. hep-ph/0405042 (2004).

[wes] http://www.wessingtoncryogenics.co.uk

[Wie03] M. Wiesmann. *A Silicon Microstrip Detector for COMPASS and a First Measurement of the Transverse Polarization of Λ^0-Hyperons from quasi-real Photo-production*. Phd thesis, TU München, 2003.

Acknowledgements

During my Ph.D. many persons supported me and collaborated, in many different ways, to the realisation of this work and I want to thank all of them.

I first wish to thank my supervisor Prof. Stephan Paul for his guidance. His trust and encouragement, the autonomy he left me and the discussions we had have provided me with motivation to pursue my goals.

I want to thank Antonello Esposito and Jan Friedrich. Under their scientific guidance I was introduced to the marvellous world of cryogenics and silicon detectors and of the physics analysis, respectively. From the critical and constructive comments of Jan and his precious suggestions much of this work is in debt. Antonello has also the responsibility of bringing me here and I can finally thank him for that.

Thanks a lot to all past and present members of the silicon group: Michael Wiesmann, Robert Wagner, Annemarie Fuchs, Matthias Becker and all the working student with whom I worked, shouted, but especially have great time in Munich and at CERN.

Thank to Igor Konorov, for all what I learned from him in these years, electronically but not only. A special thank for the Arbat.

Many many thanks to the rest of the Munich COMPASS group for the help with "alles mögliches". A special mention is for Boris Grube, Roland Kuhn, (without them I would be still screaming at my computer), Lars Schmitt (for answering to all possible questions), Heinz Angerer and Bernhard Ketzer.

Thanks to Igor Altarev, Uwe Trinks and the Tritron Hütte for their great ideas and the patience they had with mines.

Thanks a lot to my officemate Daniele Tortorella, who stood me during the most stressing time of this work.

Thanks to Frau Frank for the help with all the German papers who passed in my hands in this four years.

I want to thank also all the E18 for the nice atmosphere in our group, for having fun together and for laughing at all my jokes.

During my theses CERN became a well familiar place; I met there several exceptional persons from whom I have learned much: I want to thank the whole COMPASS collaboration, Jan McGill and Tapio Niinikoski.

A big support came in these years from my friends: as newcomer in a foreign land I have benefit from the help and the warmth of the "historic" friends I left in Napoli and the fantastic ones I met here. Thanks to Rosanna and Peppe for always been there when I needed to be cherished. Thanks to Laura, for her decisive role in technical, job and emotional business. Thanks to Aprajita for teaching me english (and how to write a PhD thesis) and warming me in the cold German years.

Dedico questa tesi alla mia famiglia: mamma, papa', Marco, Tata e zio Adriano, per tutto l'affetto che mi hanno dato, per aver creduto in me e per aver sempre appoggiato le mie scelte, non ultima questa avventura tedesca.

Und, herzlich, Christoph der, trotz eines ganzen Ozeans (und mehr), mir Heiterkeit gegeben hat um diese Arbeit fertigzumachen.

Own Contributions

I have spent the biggest part of time during my thesis in the design, development and installation of the cryogenic silicon system. Due to the small size of the COMPASS silicon group, I have been involved in all phases of the development and construction.

One of my main tasks has been the design, production and testing of the cryogenic infrastructure. This included contact to different workshops and private companies. Since the CERN security policy requires every cryogenic and under pressure installation to respect certain security requirements, a part of my work concerned the preparation of the required documentation to obtain the TÜV approval for the cryogenic infrastructure. Part of this work has been completed by Matthias Becker.

I have also contributed to the assembly and testing of the first detector prototypes. This included to learn bonding technologies, to debug the part of the readout electronics connected to the detector or the APV25 and to participate to several test beams at CERN.

Together with Michael Wiesmann I have developped the procedure for the assembly of silicon detectors and have contacted and instructed a private company for starting a mass production of the detectors.

Since the silicon detectors had to be installed and deinstalled every year from their location in the COMPASS experiment, I participate several times in this procedure.

I was involved also in the planning and scheduling of the silicon project. In 2003 I organised in the installation of the detectors and cryogenic infrastructure in the COMPASS experiment. I participate to the COMPASS shifts, partly as shift leader. I supervised several work students who collaborated in the silicon project.

Starting from the end of 2003 I started the analysis of the COMPASS data. In the framework of the PHAST analysis package I implemented C++ based routines for the dedicated physics analysis. Under the supervision of Prof. Stephan Paul and Dr. Jan Friedrich I measured the cross section for the production of Ξ^{0*} in

muon-production and calculated an upper limit for the cross section of the pentaquark candidate Ξ^{--}. I have presented the results of my work to the COMPASS collaboration and in some international conferences.